PONTIFICIA UNIVERSIDAD CATOLICA DE CHILE
SCHOOL OF ENGINEERING

MATHEMATICAL MODELING OF SPACE-TIME VARIATION IN ACOUSTIC TRANSMISSION AND SCATTERING FROM SCHOOLS OF SWIM BLADDER FISH

MARÍA PAZ RAVEAU MORALES

Thesis submitted to the Office of Graduate Studies
in partial fulfillment of the requirements for the degree of
Doctor in Engineering Sciences

Advisors:
CRISTIÁN ESCAURIAZA MESA,
CHRISTOPHER FEUILLADE

Santiago de Chile, October 2015

PONTIFICIA UNIVERSIDAD CATOLICA DE CHILE
SCHOOL OF ENGINEERING

MATHEMATICAL MODELING OF SPACE-TIME VARIATION IN ACOUSTIC TRANSMISSION AND SCATTERING FROM SCHOOLS OF SWIM BLADDER FISH

MARÍA PAZ RAVEAU MORALES

Members of the Committee:
CRISTIÁN ESCAURIAZA MESA,
CHRISTOPHER FEUILLADE
RODRIGO CIENFUEGOS CARRASCO
JAIME DELANNOY ARRIAGADA
ROGER C. GAUSS
JORGE ARENAS
CRISTIÁN VIAL EDWARDS

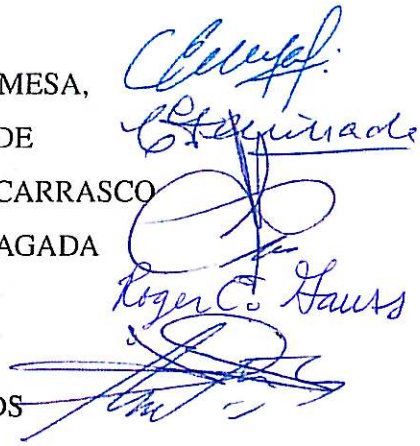

Thesis submitted to the Office of Graduate Studies
in partial fulfillment of the requirements for the degree of
Doctor in Engineering Sciences

Santiago de Chile, October 2015

Gratefully to my family

ACKNOWLEDGEMENTS

At first, thanks go to my family for almost unbelievable support. They are the most important people in my world and I dedicate this thesis to them.

Special mention goes to my professor, Christopher Feuillade. He offered me so much advice, patiently supervising me, and always guiding me in the right direction. I have learned a lot from him, without his help I could not have finished my dissertation successfully. Thank you, Profe!

I would like to give my sincere thanks to my supervisor, Cristián Escauriaza, for accepting me into his group, encouraging my research, engaging me in new ideas, and for all of the meetings and chats over the years. I would also like to thank my committee members, professors Rodrigo Cienfuegos, Jaime Delannoy, Jorge Arenas and Roger Gauss for their interest in my work. Additionally, I am very grateful for the support of all of the members of the Hydraulic and Environmental Engineering Department.

Special thanks are also given to Preston Wilson, who accepted me as a visiting scholar at the University of Texas at Austin, and to all those persons who have helped me when I collected necessary data for my investigation, including Gabriel Venegas, Craig Dolder, Greg Enenstein, Orest Diachok, Jim Lynch, Arthur Newhall and Ying-Tsong Lin.

Finally, but by no means least, I am grateful for the funding sources that allowed me to pursue my graduate school studies. This work was supported by the Comisión Nacional de Investigación Científica y Tecnológica (CONICYT) and by the Office of Naval Research under Grant N00014-11-1-0161.

TABLE OF CONTENTS

LIST OF FIGURES

LIST OF TABLES

PONTIFICIA UNIVERSIDAD CATOLICA DE CHILE
ESCUELA DE INGENIERIA

MATHEMATICAL MODELING OF SPACE-TIME VARIATION IN ACOUSTIC TRANSMISSION AND SCATTERING FROM SCHOOLS OF SWIM BLADDER FISH

Thesis submitted to the Office of Research and Graduate Studies in partial fulfillment of the requirements for the Degree of Doctor in Engineering Sciences by

MARIA P. RAVEAU

ABSTRACT

A coupled differential equation formalism is used to investigate both spatial and temporal variations of acoustic propagation and scattering due to schools of swim bladder fish. The method uses a verified swim bladder scattering kernel for the individual fish, and incorporates all orders of multiple scattering between the fish, and coherent interactions between their scattered fields. The work presented here consists of three main sections: (1) The mathematical formalism is used to investigate the forward scattering properties of fish schools. Results are presented of an analysis of acoustic transmission data obtained in 1995 during an experiment performed in the Gulf of Lion in the Mediterranean Sea. The analysis shows that using forward scattering leads to significantly larger estimates of fish abundance than previous analysis based upon back scattering approaches. (2) The results of applying the formalism are compared with those of another widely used scattering approach: the effective medium method. A theoretical comparison of the models shows good agreement over the entire resonance region in the forward scattering direction, where interference effects have a minimal effect. Good agreement is also seen in back scattering at low frequencies, where the wavelength $\lambda \geq 4s$, and s is the average nearest neighbor fish separation. A comparison with low frequency forward scattering data shows very good agreement for both models. For back scattering data, the effective medium method diverges strongly when $\lambda < 4s$ (3) Time domain solutions of the coupled equations are used

to calculate the impulse response of a bubble cloud in a compressible medium. This method is based on perturbation theory, and provides for an approximate solution formulated by adding a perturbation to the mathematical description of an exactly solvable problem. The model is successfully applied to describe experimental data derived from measurements of a model bubble cloud response in a shallow fresh water environment.

Members of the Doctoral Thesis Committee:

Cristián Escauriaza Mesa
Christopher Feuillade
Rodrigo Cienfuegos Carrasco
Jaime Delannoy Arriagada
Jorge Arenas Bermúdez
Roger C. Gauss
Cristián Vial Edwards

Santiago, October, 2015

PONTIFICIA UNIVERSIDAD CATOLICA DE CHILE
ESCUELA DE INGENIERIA

MODELAMIENTO MATEMÁTICO DE VARIACIONES ESPACIO-TEMPORALES EN LA TRANSMISIÓN ACÚSTICA DE CARDÚMENES

Tesis enviada a la Dirección de Investigación y Postgrado en cumplimiento parcial de los requisitos para el grado de Doctor en Ciencias de la Ingeniería.

MARÍA PAZ RAVEAU MORALES

RESUMEN

Se utiliza un enfoque de ecuaciones diferenciales acopladas para investigar las variaciones espaciales y temporales de la propagación acústica de cardúmenes y burbujas. Este método incorpora coherentemente las interacciones acústicas entre individuos. El presente trabajo consiste en tres secciones principales:(1) El modelo descrito es usado para investigar las propiedades acústicas de cardúmenes en la dirección de la onda incidente (dirección posterior). Se presentan los resultados de un análisis de datos de transmisión, obtenidos en 1995 durante un experimento realizado en el Golfo de Lion en el mar Mediterráneo. El presente análisis conduce a estimaciones significativamente mayores de abundancia de peces que el análisis anterior. (2)Este modelo también se compara con el enfoque del medio efectivo, ampliamente usado en problemas de dispersión acústica. La comparación teórica de los modelos muestra una buena concordancia cerca de la región de resonancia en la dirección posterior, donde los efectos de interferencia tienen un efecto mínimo. También se observa una buena concordancia en la dispersión de retorno para frecuencias bajas, donde la longitud de onda $\lambda \geq 4s$, y s es la separación media entre vecinos más cercanos. La comparación con datos de baja frecuencia resulta igualmente buena para la dispersión posterior, mientras que en la dirección de retorno el método del medio efectivo diverge fuertemente para $\lambda < 4s$. (3) Se propone una solución en el dominio del tiempo para calcular la respuesta al impulso de una nube de burbujas en un medio compresible,

incorporando los efectos de dispersión múltiple entre burbujas. Este método se basa en la teoría de perturbación y proporciona una solución aproximada, formulada mediante la adición de una perturbación a la descripción matemática de un problema exactamente soluble. El modelo se aplicó con éxito a las mediciones experimentales de una nube artificial de burbujas en un entorno de agua dulce de poca profundidad

Miembros de la Comisión de Tesis Doctoral

Cristián Escauriaza Mesa
Christopher Feuillade
Rodrigo Cienfuegos Carrasco
Jaime Delannoy Arriagada
Jorge Arenas Bermúdez
Roger C. Gauss
Cristián Vial Edwards

Santiago, Octubre, 2015

1. INTRODUCTION

1.1. Problem Description: Acoustic scattering from school of fish

Sound propagation in the ocean has been a topic of great importance since the middle of the last century. While light is typically absorbed within a few meters in the water column, sound can propagate long distances with relatively little attenuation. Therefore, acoustic methods have been widely used as a tool to investigate the ocean. Originally developed for military purposes, ocean acoustics has expanded its scope and has been used for the exploration and mapping of the seabed, the remote sensing of fish schools, and the study of marine mammal communication, among others. A distinguishing feature of the oceanic medium is its heterogeneity. Plankton patches, schools of fish, marine mammals and bubble clouds are only a few of the elements that can be found in the sea, which affect or may be affected by acoustic signals.

Bubbles in the water column are generated by several processes, such as breaking waves, cavitation from ship propellers, or even the biological action of microorganisms. Another cause of "bubbles" is the presence of swim bladder-bearing fish. A swim bladder is an internal gas-filled organ within a fish, which allows it to control its buoyancy and to stay at its current water depth without using energy in swimming. At low acoustic frequencies, scattering from a swim bladder fish is dominated by the volume pulsation, or "monopole" resonance, of the swim bladder, which can significantly enhance the received signals compared to specular scatter. A swim bladder behaves very similarly to an air bubble in water, and this led Marshall (1951) to consider scattering from fish with air-filled swim bladders as the cause of high levels of acoustic volume reverberation in deep scattering layers. It is now known that resonant back scattering by swim bladder-bearing fish is the major cause of volume reverberation in the ocean at frequencies up to at least 10 kHz. (Farquhar,1976;Andreeva,1964;Nero et al.,1997)

While scattering from individual dispersed fish continues to be important, attention has recently been focused on the related problem of resonance scattering from schools,

and other ensembles, of swim bladder fish. (McCartney,1967;Holliday,1972;Scrimger et al.,1972;Gong et al.,2010;Andrews et al.,2011;Weber et al.,2013) Schools of fish typically consist of closely spaced individuals of similar size, (Pitcher et al.,1985;Pitcher & Parrish,1993;Breder,1965;Gordoa & Duarte,1991) and at resonance frequencies multiple scattering processes among the fish become significant and complex. The acoustic wavelength at the monopole resonance frequency of a swim bladder is generally many times the length of the fish. Since fish in a closely spaced school typically arrange themselves to be about a fish length apart, (Misund,1991) the scattered waves from neighboring fish interact coherently. This feature is a function of the spatial organization of the fish in the school, and must be correctly incorporated, together with multiple scattering, to accurately predict levels of back scattering from schools of bladder fish. The recent work reported by Weber et al. (2013), on near resonance scattering from schools of juvenile Atlantic bluefin tuna, emphasizes the importance of considering both multiple scattering and spatial organization within the school when estimating the target strength of the school.

Over the past decades, theories of multiple scattering from bubbles in water have predominantly used time-independent descriptions. A classic approach is to consider the bubble cloud as a single scattering object, whose internal acoustic properties are described using a modified propagation wavenumber. The acoustic field due to a wave propagating through this medium can be determined by solving the corresponding Helmholtz equation. This is known as the "effective medium" model, and is based on the theory of multiple scattering of waves developed by Foldy and Carstensen.(Foldy,1945;Carstensen & Foldy,1947) Later on, an important study by Commander and Prosperetti (1989) showed that the effective medium model underestimates the scattering amplitude in the vicinity of the resonance frequency of the bubbles, especially in dense clusters of bubbles. This can be explained by the fact that the model does not correctly represent the phenomena of acoustic interaction among bubbles, and several corrections have been subsequently proposed in order to include this effect(Feuillade,1996;Ye & Ding,1995;Kargl,2002;Henyey,1999). In a recent article, Hahn (2007) used effective medium theory to study scattering effects such as low frequency collective resonances in idealized, spherically shaped, schools of bladder fish.

According to Hahn, the effective medium method is ideal for this purpose, since it facilitates investigations by providing explicit expressions for the scattering amplitude and cross section. Another approach to multiple scattering from bubbles is to solve a coupled differential equation system. At sufficiently small amplitudes the behavior of an air-bubble in a liquid can be approximated as a simple harmonic oscillator, represented by a mass-spring differential equation. This method incorporates both multiple scattering effects between bubbles, and coherent interactions of their individual scattered fields.(Feuillade et al.,1996)

While most previous theoretical and experimental research at low frequencies has concentrated on back scattering from fish schools, some work has also been done on the propagation and absorption of sound as it passes through the fish, which is directly related to the "forward scattering" problem. The primary purpose of this latter work has been to investigate the use of acoustic techniques to identify the species of schooling fish, to determine their abundance, and to study their behavior. Weston and Ching (Weston,1977;Weston & Ching,1970;Ching & Weston,1971) made measurements of sound extinction between 300 Hz and 4400 Hz in the Bristol Channel. Diachok (1999,2000) pioneered the development of fish absorption spectroscopy, and has analyzed data obtained during the 1995 Gulf of Lion experiment in the Mediterranean Sea to both identify species and behavior, and to directly infer fish abundance (specifically, the number of sardines in a typical school) via the inversion of acoustic transmission data. More recently, Gong et al. (2010) used several different sonar systems in the 300-1200 Hz range, looking at both scattering and attenuation, to monitor large shoals of Atlantic herring during the 2006 Gulf of Maine experiment, and to make estimates of target strength, and to determine spatial distributions, abundance, and behavior, over time. Subsequently, Andrews et al. (2011) used a numerical Monte-Carlo technique to model scattering, propagation, and attenuation for the same experiment, and to study the population density of Atlantic herring.

In time domain modeling, the acoustic interaction between bubbles has classically been considered as an instantaneous problem.(Leighton,1994;Doinikov & Zavtrak,1995;Mettin et al.,1997) For a compressible liquid, with a finite speed of sound propagation, the acoustic response of any bubble to the incident field, and to the field scattered by all the other

bubbles, is a time-retarded response. Time delays directly affect the constructive or destructive interference of all the scattered fields, and therefore can be a factor of critical importance in the acoustic behavior of bubble clouds. During recent years, substantial progress has been achieved in the development of time-delay acoustic coupling in multi-bubble systems. The radiation forces between gas bubbles, which are also known as secondary Bjerknes forces, were investigated for two coupled oscillating bubbles (Doinikov & Zavtrak,1997;Doinikov,2001;Mettin et al.,2000) in a compressible medium, as well as the forced oscillations caused by an external acoustic field. (Feuillade,2001;Hsiao et al.,2001) More recent works analyzed the time delay effects on the free oscillation of a linear bubble chain system. (Doinikov et al.,2005;Ooi et al.,2008)

The main purpose of the present work (Chapter 4) is to present a new method to calculate the impulse response of a near surface bubble cloud in a compressible medium, based on perturbation theory. Chapters 2 and 3 intend to provide a full understanding of the current current steady-state model, including an investigation of the forward scattered field of a fish school, as opposed to the back scattered field, and a comparison with the Effective Medium approach.

1.2. Research question and objectives

Previous CW solutions enabled an investigation of the scattered intensity as a function of frequency, and as a function of azimuthal angle to the fish school. These static solutions, however, are not suitable for developing an understanding of the spatial and temporal variations in the acoustic field scattered from, and transmitted trough a large fish school, where the shape of the school, and the numerical distribution of the fish may vary significantly over an extended volume, causing large fluctuations in the received time signal.

The purpose of the proposed research is to develop true accurate time domain solutions to a set of coupled differential equations, describing the coupled acoustic behavior of a school of swim bladder fish in response to a time varying input signal. This will enable time signal returns to be analyzed in terms of arrivals from different spatial sections of a fish

school. By identifying individual portions of the received time signals in this way, it should be possible to study the relationship between the fluctuating shapes and fish distributions of a school, and the resulting stochastic variations in the received signals.

Another important goal will be validation of the method. This may be achieved by comparison with previously gathered fishery survey data, where available, or, if possible, using data from future at-sea experiments. An interim stage may be to compare the model against data obtained from computer simulations of fish school behavior using currently available biomathematical models of their ensemble behavior.

1.3. Existing approaches in Frequency-Domain models

1.3.1. Scattering due to a single fish

The resonance characteristics of fish swim bladders and air bubbles in water are physically similar, and spherical "bubble-like" models have been a popular method for describing resonance scattering from swim bladder bearing fish. (Feuillade & Nero,1998) The monopole action dominates the low-frequency scattering response, and the scattered field distribution has a strong spherical symmetry, even for highly elongated swimbladders. (Feuillade,2012)

The acoustic behavior of a spherical bubble in water was described by Minnaert (1933), and developed by Devin (1959), using a method which identifies the monopole response as the solution of a "mass-spring" second-order differential equation, i.e.,

$$m\ddot{\nu} + b\dot{\nu} + \kappa\nu = -P_0\, e^{i\omega t.} \ . \tag{1.1}$$

In this equation, the variable ν (called the differential volume) is the difference between the instantaneous volume, and the equilibrium volume (i.e, $4\pi a^3/3$), of a bubble of radius a. The coefficient $m(= \rho/4\pi a)$ is termed the radiation mass, (Leighton,1994) where ρ is the density of water. The quantity $\kappa(= 3\gamma P_A/4\pi a^3)$ is the adiabatic stiffness, where γ is the gas constant, and P_A is the ambient water pressure. The coefficient b describes the damping of the bubble motion, while P and ω represent the amplitude and frequency, respectively,

of the external pressure field applied to the bubble (P is preceded by a minus sign, since a decrease in pressure results in an increase in the bubble volume).

If a harmonic steady state solution of Eq. (1.1) of the form $\nu = \overline{\nu}e^{i\omega t}$ is assumed, substitution yields the individual bubble resonance response function

$$\overline{\nu} = \frac{-P_0}{\kappa - \omega^2 m + i\omega b} = \frac{-(P_0/\omega^2 m)}{\left(\frac{\omega_0^2}{\omega^2} - 1\right) + i\frac{b}{m\omega}}\ , \tag{1.2}$$

where $\omega_0 = 2\pi f_0 = \sqrt{\kappa/m} = (1/a)\sqrt{3\gamma P_A/\rho}$, and f_0 is the Minnaert resonance frequency. If $k_0 (= \omega_0/c)$ denotes the propagation wave number at resonance, then, for an air bubble at atmospheric pressure in fresh water, assuming the speed of acoustic wave propagation c = 1500 m/s, the value of $k_0 a \approx 0.0136$, making the wavelength at resonance $\approx 460\times$ the bubble radius. The imaginary component $b/m\omega$ in the denominator of Eq. (1.2), is identified with a bubble damping parameter, comprising radiative, viscous, and thermal terms, i.e.

$$\delta_B = \frac{b}{m\omega} = \delta_r + \delta_v + \delta_t = \frac{\omega_0}{\omega Q}, \tag{1.3}$$

where the "quality factor" Q has also been introduced, which is defined at the resonance frequency as $Q = m\omega_0/b = 1/\delta_B(\omega_0)$, i.e., at the resonance frequency, Q is the reciprocal of δ_B.

In the spherical swim bladder model introduced by Love (1978), a parameter H is introduced, which also consists of three terms representing radiation, viscous, and thermal damping, as follows:

$$\frac{1}{H} = \frac{1}{H_r} + \frac{1}{H_v} + \frac{1}{H_t}. \tag{1.4}$$

Love indicates that, at the low frequencies where his model is typically applicable, damping losses due to thermal effects are minimal and may be neglected. The expressions for H_r and H_v are:(Love,1978)

$$H_r = \frac{\omega_0 c}{\omega^2 a} \qquad ; \qquad H_v = \frac{\omega_0 \rho a^2}{2\xi}\ , \tag{1.5}$$

where ξ is the viscosity of fish flesh surrounding the swim bladder. Note that, in Eq. (1.5), both damping factors contain the parameter a, which now refers to the "radius" of the swim bladder. Throughout the present work, whenever the term "swim bladder radius" is used, it always refers to the radius of the sphere of volume equivalent to that of the (typically nonspherical) swim bladder.

Recently, Baik (2013) questioned the accuracy of Love's model, and particularly the viscous damping term, and proposed corrections. Subsequently, Love (2013) has indicated that the concerns raised by Baik are moot for experiments conducted on fish in the ocean, and that his original swim bladder model maintains its practical validity. Therefore, in this work, Love's swim bladder model is applied using the viscous damping term as originally defined.(Love,1978,1977)

The acoustic field reradiated into the surrounding water by a bubble (or swim bladder) when an external field is incident upon it, as described by Eq. (1.1), is predominantly monopolar and isotropic. The scattered pressure field amplitude, at range r and time t, is given by: (Lamb,1945)

$$p_s(r,t) = \frac{\rho e^{-ikr}}{4\pi r}\,\ddot{\nu} = \frac{-\rho\omega^2}{4\pi r}\,\overline{\nu}\,e^{i(\omega t-kr)} = \mathrm{f}_b\,P_0\,\frac{e^{i(\omega t-kr)}}{r}\,, \tag{1.6}$$

where $k(=\omega/c)$ is the propagation wave number for water applicable to the incident field, and $\mathrm{f}_b = a/[(\omega_0^2/\omega^2)-1+i\delta_B]$ is the "scattering amplitude" of the bubble, or swim bladder.

While the distribution of the scattered pressure field in the resonance region has strong spherical symmetry, even for highly elongated bladders, the elongation causes the resonance frequency to increase above that for a spherical swim bladder of the same gas volume.(Feuillade,2012) The shape of swim bladders typically approximates that of a prolate spheroid, which is a three dimensional object generated by rotating an ellipse 180 deg around its major axis. Assuming it is a prolate spheroid, Weston (Weston,1977) proposed a correction factor for the resonance frequency due to nonsphericity. If f_ϵ is the resonance frequency of the prolate spheroid, and f_1 is the resonance frequency of a spherical bladder

of the same volume, Weston's expression is:

$$\frac{f_\epsilon}{f_1} = \sqrt{2}\ \epsilon^{-1/3}\ (1-\epsilon^2)^{1/4}\ \left[\ln\left\{\frac{1+(1-\epsilon^2)^{1/2}}{1-(1-\epsilon^2)^{1/2}}\right\}\right]^{-1/2}\ , \tag{1.7}$$

where $\epsilon \equiv \alpha^{-1}$, and α is the aspect ratio of the prolate spheroid, i.e., the ratio of the lengths of the major and minor axes of the generating ellipse.

When using Love's swim bladder model to analyze experimental data, the nominal resonance frequency is typically increased using Weston's correction factor, based on available evidence for the degree of elongation of the swim bladder, obtained from sampled fish, or from previously published data.

An alternative method of studying the acoustic resonances of a bubble is to examine sound scattering from its surface. This can be performed by using Anderson's fluid sphere theory, (Anderson,1950) in which a bubble is characterized as a spherical void filled with air placed within the larger mass of water. This method predicts a monopole resonance frequency essentially identical to that obtained by Minnaert. (Feuillade & Clay,1999)

1.3.2. School scattering theory 1: the effective medium method

Hahn (Hahn,2007) reviews the effective medium method, based on the theory of multiple scattering of waves between bubbles developed by Foldy and Carstensen, (Carstensen & Foldy,1947;Foldy,1945)and applies it to water containing swim bladder fish, stating that the spatial distribution of the acoustic field due to a wave propagating through a fish school may be determined by solving the Helmholtz equation:

$$(\nabla^2 + k_e^2)p = 0\ , \tag{1.8}$$

where k_e is the effective propagation wave number for the fish school medium which, at low frequencies, is dominated by the swim bladder resonance response. If the swim bladders are all identical , k_e is given by

$$k_e^2 = k^2 + 4\pi n \mathrm{f}_b\ , \tag{1.9}$$

where n is the density of fish (and, therefore, of swim bladders) per unit volume, which can be a function of position, k is again the propagation wave number for water (without fish), and f_b is the scattering amplitude of a single swim bladder, as defined via Eqs. (1.2) and (1.6).

The effective medium approach to calculating scattering from a fish school ensemble represents the school as a single scattering object, whose acoustic wave propagation properties are determined by k_e, as defined in Eq. (1.9). Rather than calculating, and then aggregating, the scattering from all the swim bladders individually, the procedure circumscribes the entire volume containing the school by a closed three-dimensional surface that geometrically matches its external boundary. Outside the surface is water. Inside the surface there is considered to be a second ("effective") fluid, for which the macroscopic properties are described by Eq. (1.9). Scattering from the ensemble is then determined by the overall shape of the volume, and by imposing appropriate boundary conditions at the surface separating the two fluids.

While, in Hahn's paper (Hahn,2007), Eq. (1.9) was originally determined by using multiple scattering considerations, (Foldy,1945) it may also be derived using a completely distinct physical argument. (Clay & Medwin,1977) The sound speed of water is given by $K_w = 1/\rho c^2$ where K_w is the compressibility of water. In water containing swim bladder fish, the effective compressibility K_e of the combined medium is the sum of two components, i.e., $K_e = K_w + K_b = 1/\rho_e c_e^2$, where K_b is the compressibility due to the swim bladders; and ρ_e and c_e are the effective density and effective sound speed of the combined medium, respectively. Since compressibility is defined as the fractional change in volume divided by the change in pressure, we find from Eq. (1.2), assuming there are n swim bladders per unit volume, all with the same radius a, that

$$K_b = -\frac{\overline{\nu}}{P} \times n = \frac{(n/\omega^2 m)}{\left(\frac{\omega_0^2}{\omega^2} - 1\right) + i\delta_B} = \frac{(4\pi a n/\rho\omega^2)}{\left(\frac{\omega_0^2}{\omega^2} - 1\right) + i\delta_B} \,. \tag{1.10}$$

Love (Love,1978) indicates that the density of sea-water (where this method is primarily applied) differs very little ($< 2.5\%$) from that of fish flesh. Furthermore, the density of air

is much less than that of water, and since the air volume fraction for schools of fish is also very small, then it is a good approximation to assume $\rho_e \approx \rho$, so that

$$K_e = K_w + K_b \Rightarrow \frac{1}{\rho_e c_e^2} = \frac{1}{\rho c^2} + \frac{4\pi a n}{\rho\omega^2\left[\left(\frac{\omega_0^2}{\omega^2} - 1\right) + i\delta_B\right]} \,. \tag{1.11}$$

Multiplying both sides of the resulting equation of Eq. (1.11) by $\rho\,\omega^2$ immediately recovers Eq. (1.9).

Note that the derivation of Eq. (1.11) incorporates no information about scattering interactions between the swim bladders. It simply considers the compressibility of one swim bladder, which is assumed to be isolated from the others around it. This compressibility is simply multiplied by the number of swim bladders per unit volume to obtain their collective compressibility. As a result, the use of Eq. (1.9) to calculate fish school scattering incorporates an implicit assumption that multiple scattering interactions between the swim bladders do not enhance or modify the levels of scattering, and may be neglected. Hahn (Hahn,2007) notes that Eq. (1.9) represents the "lowest order" expression for the wave number of the effective medium derivable from the Foldy theory, and that Eq. (1.9) is a good approximation for the wave number if $|4\pi n \mathrm{f}_b^2/k| \ll 1$, as indicated by Frisch. (Frisch,1970) Depending also upon both the scattering amplitude f_b and the ensonification frequency ω (via $k = \omega/c$), this condition should effectively limit the number density of fish n of a school for which the acoustical propagation properties can be accurately represented by Eq. (1.9).

There also exists a high frequency limit for the applicability of the effective medium approach to fish school scattering. In order to represent the school as a single acoustical object, rather than an ensemble of individual fish, the ensonification frequency must be sufficiently low (and the corresponding wavelength sufficiently long) to justify the assumption that the incident field does not resolve the fish as discretely identifiable scatterers. In optical and acoustic holography, the resolution is defined by the minimum separation distance between two distinguishable point objects. (Maynard et al.,1985;Kim & Nelson,2003) Applying the principles of source reconstruction techniques, the minimum resolvable distance

$s \sim \pi/k = \lambda/2$, which implies $\lambda/s \sim 2$, where λ is the wavelength. In the case of acoustical scattering from fish, let us suppose two fish separated by a distance s, both lying along the axis between the source and receiver. (Raveau & Feuillade,2015) If the source and receiver are co-located (the back scattering case), the distance traveled by the incident field directly from the source to one fish and then back to the receiver, is not the same as for the other fish. There is a path difference of $2s$ and, at the receiver, a phase $2s \times k$ differentiates the arrivals from the two fish. According to the resolution principle, the wavelength required to resolve the fish will then be given by $2s \sim \lambda/2$, i.e., $\lambda/s \sim 4$.

On the other hand, if the receiver is located on the opposite side of the fish from the source (the forward scattering case), the two fish are ensonified in such a way that the total distance traveled by the waves, from the source to the receiver, is the same for both of them. (Raveau & Feuillade,2015) Therefore, in forward scattering, no phase difference is introduced due to the two distinct propagation paths and, as a result, the arrivals from the two scatterers are not differentiated by the receiver. The practical consequence of this, as demonstrated in Chapter 3, is that, while the upper frequency limit on the applicability of the effective medium approach to fish school scattering clearly applies in back scattering cases, it is largely inapplicable in forward scattering cases, or in cases where the total scattering cross section, which is typically dominated by the forward scattering component, is at issue.

For a school of fish, the separate paths between the scatterers and the receiver are not as simple to analyse as for two fish. Within a school, some fish will be located near the source-receiver axis, while other fish will lie off-axis, and incur additional phase shifts as a result. This means that phase difference effects are not completely absent in forward scattering, although they are typically negligible. In contrast, back scattering practically always leads to large phase differences at the receiver.

In back scattering, the upper frequency limit is expected to occur roughly when the acoustic wavelength in the external water medium $\lambda \sim 4s$, where s is now the average nearest neighbor spacing between fish. This can be used to specify an approximate upper

frequency limit $f_u \lesssim c/4s$ for the application of the effective medium approach to fish school scattering. At this limit, while the incident wave may not resolve two adjacent fish, it could still resolve fish separated further apart in the school. Nevertheless, since the strongest acoustical interactions occur between adjacent fish, this definition of f_u is still a reasonable assumption.

Henceforward, for simplicity, the " effective medium method," or "effective medium," is referred to using the abbreviation EM.

1.3.3. School scattering theory 2: the coupled differential equation approach

Another approach to modeling school scattering uses a mathematical formalism based upon the harmonic solution of sets of coupled differential equations. (Feuillade et al.,1996) It allows a verified swim bladder scattering kernel for the individual fish to be incorporated (in this work, the Love model (Love,1978) is used), includes all multiple scattering interactions between the fish, and calculates the aggregate scattering field by coherent summation. Only a brief summary is given here. The cited article (Feuillade et al.,1996) gives full details.

When an external pressure field is incident on an ensemble of N fish, the scattering of each fish is the response not only to external field, but also to the aggregate scattered field from all the other fish. In 1996, Feuillade et al. (1996) developed a model which considers both the scattered field from each individual fish, and the interactions between them, using a system of coupled equations, as follows:

$$\begin{aligned}
&m_1\ddot{\nu}_1 + b_1\dot{\nu}_1 + \kappa_1\nu_1 = -P_1 e^{i(\omega t+\phi_1)} - \textstyle\sum_{j\neq 1}^{N} \frac{\rho e^{-iks_{j1}}}{4\pi s_{j1}}\ddot{\nu}_j \\
&\vdots \\
&m_n\ddot{\nu}_n + b_n\dot{\nu}_n + \kappa_n\nu_n = -P_n e^{i(\omega t+\phi_n)} - \textstyle\sum_{j\neq n}^{N} \frac{\rho e^{-iks_{jn}}}{4\pi s_{jn}}\ddot{\nu}_j \qquad , \qquad (1.12) \\
&\vdots \\
&m_N\ddot{\nu}_N + b_N\dot{\nu}_N + \kappa_N\nu_N = -P_N e^{i(\omega t+\phi_N)} - \textstyle\sum_{j=1}^{N-1} \frac{\rho e^{-iks_{jN}}}{4\pi s_{jN}}\ddot{\nu}_j
\end{aligned}$$

Here, P_n and ϕ_n are the amplitude and phase of the external field incident on the n-th fish swim bladder, and s_{jn} is the separation distance between the centers of the j-th and n-th

bladders, etc. The variable quantities m_n , b_n , κ_n , etc., appearing in these equations, allow for different values for the swim bladder radii, damping, etc., to be incorporated into the model, to represent a diverse range of individual fish properties within the school. Note, on the RHS of every equation in (1.12), that each bladder is driven by both the external field and the scattered fields from the other bladders as given by Eq. (1.6).

Looking for harmonic steady state solutions, by substituting $\nu_1 = \overline{\nu}_1 e^{i\omega t}, \nu_2 = \overline{\nu}_2 e^{i\omega t}, \ldots$ etc., in (1.12), a matrix equation $\mathbf{M}\mathbf{v} = \mathbf{p}$ is obtained, where $\mathbf{v} = \{\overline{\nu}_1, \ldots, \overline{\nu}_n, \ldots, \overline{\nu}_N\}$ and $\mathbf{p} = \{-P_1 e^{i\phi_1}, \ldots, -P_n e^{i\phi_n}, \ldots, -P_N e^{i\phi_N}\}$ are column vectors containing the steady-state volume oscillation amplitudes and external fields, respectively, for the individual bladders, and $\mathbf{M}$ is an $N \times N$ matrix with elements:

$$\begin{aligned} M_{nn} &= \kappa_n - \omega^2 m_n + i\omega b_n \ , \\ M_{nj} &= \tfrac{-\omega^2 \rho e^{-iks_{jn}}}{4\pi s_{jn}} \quad (n \neq j) \quad . \end{aligned} \tag{1.13}$$

Each diagonal term [i.e., M_{jj} $(j = 1, \ldots, N)$] describes the resonance behavior of an individual bladder, incorporating variations in size, damping, depth etc. Every off-diagonal element [i.e., M_{nj} $(j, n = 1, \ldots, N)$, $n \neq j$)] describes the radiative coupling between two of the bladders. The solution $\mathbf{v} = \mathbf{M}^{-1}\mathbf{p}$ enables the description of steady-state scattering from the whole ensemble as a function of the external field amplitude and frequency. Once the $\overline{\nu}_n$ are found, the total scattered pressure field for the whole school, for any azimuthal angle, is given by the coherent summation

$$p_s = -\frac{\rho\omega^2}{4\pi} \sum_{n=1}^{N} \frac{\overline{\nu}_n e^{-ikr_n}}{r_n} \ , \tag{1.14}$$

where r_n is the distance between the n-th swim bladder and a point receiver, located in the far field.

The ensemble scattered field in any direction is affected by coherent interactions between the scattered fields from the individual fish. For this reason, the phase factor e^{-ikr_n} for each swim bladder must be included inside the summation of Eq. (1.14). Similarly, it is

necessary to define a scattering amplitude f_s for the whole school ensemble [cf. Eq. (1.6)] by:

$$p_s = \frac{P_0}{r}\mathrm{f}_s \ . \tag{1.15}$$

Equation (1.15) assumes that the field is detected in the far-field, so we can substitute $r_1,\, r_2, \ldots, r_N \approx r$ in the denominator of Eq. (1.14), and treat the fish school as a point scatterer. From equations (1.14) and (1.15), the scattering amplitude of the school may be expressed as

$$\mathrm{f}_s(k,\theta,\phi) = \frac{-\rho\omega^2[\ \sum_{n=1}^{N} \overline{\nu}_n e^{-ikr_n}\ ]}{4\pi P_0} \ , \tag{1.16}$$

where the angles θ and ϕ are included as arguments to indicate that the school scattering amplitude is generally anisotropic. The scattered pressure field can be obtained for a receiver placed at any arbitrary orientation with respect to the fish school, and for any bistatic angle with respect to the acoustic source, including both back and forward scattering geometries.

Note there is a difference between the definition of the scattering amplitude for a single swim bladder, as given by Eq. (1.6), and that for a school, as defined by Eqs. (1.14), (1.15), and (1.16). For a single swim bladder, the phase factor e^{-ikr} appears explicitly in Eq. (1.6) as a separate factor from the scattering amplitude f_b for a single bladder. For the school, the corresponding phase factors, i.e., e^{-ikr_n} etc., for the different fish, are incorporated inside the definition of f_s, and are found within the complex summation that appears in Eq. (1.16). Note also that Eq. (1.15) implies that the amplitude of the external field applied to the swim bladders in Equations (1.12) is the same for all of them, i.e., $P_1 = P_2 = \cdots = P_N = P_0$.

The steady-state volume oscillation amplitudes $\overline{\nu}_n$ are initially defined, in the original coupled differential equations, (Feuillade et al.,1996) to include all radiative interaction (i.e., multiple scattering) processes between the swim bladders. Therefore, the use of the $\overline{\nu}_n$ to calculate the total scattered pressure of the school, using Eq. (1.14), implicitly incorporates modifications of the scattered pressure due to multiple scattering. As a result, this method of calculating scattering from a school of swim bladder fish is not constrained by

limitations due to the individual scattering amplitude and number density of fish (specified by $|4\pi n f_b^2/k| \ll 1$) that apply to the effective medium approach.

Henceforward, for simplicity, "the coupled differential equation approach" is referred to using the abbreviation CDE.

1.4. Existing approaches in Time-Domain models

1.4.1. Single bubble

At sufficiently small amplitudes the oscillating behavior of an air-bubble in a liquid can be approximated as a simple harmonic oscillator, represented by a mass-spring differential equation.(Minnaert,1933;Devin,1959) In his 1994 book *The Acoustical Bubble*, Leighton describes the different reference frames for the equation of motion. (Leighton,1994) In general, the displacement can be defined in terms of the bubble volume v or the radius displacement r, while the driving term is expressed by either a force F or an acoustic pressure P. This leads to four different combinations:

The Radius-Pressure frame

$$m_{RP}\ddot{r}_i(t) + b_{RP}\dot{r}_i(t) + \kappa_{RP} r_i(t) = P(t), \tag{1.17}$$

the Volume-Pressure frame

$$m_{VP}\ddot{\nu}_i(t) + b_{VP}\dot{\nu}_i(t) + \kappa_{VP} \nu_i(t) = P(t), \tag{1.18}$$

the Radius-Force frame

$$m_{RF}\ddot{r}_i(t) + b_{RF}\dot{r}_i(t) + \kappa_{RF} r_i(t) = F(t), \tag{1.19}$$

and the Volume-Force frame

$$m_{VF}\ddot{\nu}_i(t) + b_{VF}\dot{\nu}_i(t) + \kappa_{VF} \nu_i(t) = F(t), \tag{1.20}$$

where the subscripts R, V, P, F refer to "Radius", "Volume", "Pressure" and "Force", respectively. Despite the different subscripts, m, b and κ represent the same physical concepts of mass, damping and stiffness in different frames, the exact values of these parameters will depend on the way the system is defined. Even so, it is possible to establish some relations between frames. If the wavelength is much greater than the bubble radius ($\lambda \gg R_0$), the acoustic pressure at equilibrium is the ratio of the acoustic force over the bubble surface to the surface area:

$$F_A = P_A 4\pi R_0^2. \tag{1.21}$$

Therefore, by comparing (1.18),(1.20) and (1.21):

$$\frac{m_{VF}}{m_{VP}} = \frac{b_{VF}}{b_{VP}} = \frac{\kappa_{VF}}{\kappa_{VP}} = 4\pi R_0^2, \tag{1.22}$$

$$\frac{m_{RF}}{m_{RP}} = \frac{b_{RF}}{b_{RP}} = \frac{\kappa_{RF}}{\kappa_{RP}} = 4\pi R_0^2. \tag{1.23}$$

It should be remembered that the terms ν and r refer to changes in radius and volume from equilibrium. Since the equilibrium volume is equal to $4\pi R_0^3/3$:

$$\nu = d\nu = 4\pi R_0^2 dR = 4\pi R_0^2 r. \tag{1.24}$$

Comparison between (1.19), (1.20) and (1.24), leads to

$$\frac{m_{RF}}{m_{VF}} = \frac{b_{RF}}{b_{VF}} = \frac{\kappa_{RF}}{\kappa_{VF}} = 4\pi R_0^2, \tag{1.25}$$

$$\frac{m_{RP}}{m_{VP}} = \frac{b_{RP}}{b_{VP}} = \frac{\kappa_{RP}}{\kappa_{VP}} = 4\pi R_0^2, \tag{1.26}$$

From (1.22) and (1.26), the values of the parameters in the radius-pressure frame equal the values of the corresponding parameters in the volume-force frame: $m_{RP} = m_{VF}$, $b_{RP} = b_{VF}$ and $\kappa_{RP} = \kappa_{VF}$.

1.4.2. Two bubbles

1.4.2.1. Mettin

Mettin $et\ al$ investigated the effect of the secondary Bjerknes force in small cavitation bubbles,(Mettin et al.,1997) starting from linear analysis of the equations of motion. A modified Keller-Miksis model was used to describe the radial motion $R_i(t)$ of two spherical bubbles coupled by a time delayed term. (Mettin et al.,2000) The delay τ is assumed to be equal for both mutual interactions and independent of time, which implies that the bubble radii are much smaller than the bubble separation distance L, and that the bubbles do not move significantly during the oscillation. Linearizing around equilibrium radii $R_i(t) = R_{i0} + r_i(t)$, the radial motion equation defined in a Radius-Pressure frame, is given by:

$$\ddot{r_i}(t) + \omega_{i0}^2 r_i(t) + f_i \dot{r_i}(t) + \frac{R_{j0}^2}{L R_{i0}} \ddot{r_j}(t-\tau) = -\frac{p_a(t)}{\rho R_{i0}}, \tag{1.27}$$

where ρ is the water density, f_i and ω_{i0} represent the damping and resonance frequency of the i-th bubble, and p_a is the driving pressure for both bubbles. Eq. (1.27) assumes small amplitudes of the external sound field, i.e. $p_a << p_{\mathrm{amb}}$, where p_{amb} is the ambient pressure. Using the harmonic approach $r_i(t) = A_i e^{i\omega t}$ and $p_a = P_a e^{i\omega t}$, leads to the solution of a linear system. It should be noted that even when Eq. (1.27) is originally defined in the time domain, the proposed solution is time independent.

According to Leighton, in a Radius-Pressure frame the mass m_{RP} is defined as $m_{RP} = \rho R_{i0}$. Multiplying Eq. (1.27) by m_{RP}:

$$m_{RP}\ddot{r_i}(t) + \kappa_{RP} r_i(t) + b_{RP}\dot{r_i}(t) + m_{RP}\frac{R_{j0}^2}{L R_{i0}} \ddot{r_j}(t-\tau) = -p_a(t). \tag{1.28}$$

Combination of eqs. (1.24) and (1.26) leads to:

$$\begin{aligned} m_{RP} r_i &= m_{VP} v_i, \\ b_{RP} r_i &= b_{VP} v_i, \\ \kappa_{RP} r_i &= \kappa_{VP} v_i, \end{aligned} \tag{1.29}$$

Substitution of Eq. (1.29) into Eq. (1.28) gives the following equation:

$$m_{VP}\ddot{\nu}_i(t) + b_{VP}\dot{\nu}_i(t) + \kappa_{VP}\nu_i(t) = -p_a(t) - m_{VP}\frac{R_{j0}^2}{LR_{i0}}\ddot{\nu}_j(t-\tau). \tag{1.30}$$

In the Volume-Pressure frame, $m_{VP} = \frac{\rho}{4\pi R_{i0}}$. Assuming identical bubbles $R_{j0} \approx R_{i0}$, Eq. (1.30) can be re-expressed as:

$$m_{VP}\ddot{\nu}_i(t) + b_{VP}\dot{\nu}_i(t) + \kappa_{VP}\nu_i(t) = -p_a(t) - \frac{\rho}{4\pi L}\ddot{\nu}_j(t-\tau). \tag{1.31}$$

1.4.2.2. Feuillade

A different approach was presented by Feuillade, where the coupling effect between the bubbles is included in the mass and damping terms.(Feuillade,2001) Considering two identical bubbles pulsating in phase, the equations are:

$$\begin{aligned} m\ddot{\nu}_1 + b\dot{\nu}_1 + \kappa\nu_1 &= -\delta(t) - \frac{\rho e^{-ikd}}{4\pi d}\ddot{\nu}_2, \\ m\ddot{\nu}_2 + b\dot{\nu}_2 + \kappa\nu_2 &= -\delta(t) - \frac{\rho e^{-ikd}}{4\pi d}\ddot{\nu}_1, \end{aligned} \tag{1.32}$$

where $\delta(t)$ represents the Dirac delta function, k is the wavenumber, and d is the distance between the bubbles. This work was addressed in a Volume-Pressure frame, hence it is expected that Eqs. (1.32) differs from Eqs. (1.27). Hovewer, Eqs. (1.28) to (1.31) show that

Eqs. (1.31) [and therefore, Eqs. (1.32)] is the equivalent form of Eqs. (1.27), in a Volume-Pressure frame. Let us asume that the damping b and the coupling term $\frac{\rho e^{-ikd}}{4\pi d}$ are frequency independent, so we can perform a Fourier transform on both sides of Eqs. (1.32):

$$\begin{aligned}\left(-\omega^2 m + ib\omega + \kappa\right)\nu_1(\omega) &= -1 + \omega^2 \frac{\rho e^{-ikd}}{4\pi d}\nu_2(\omega),\\ \left(-\omega^2 m + ib\omega + \kappa\right)\nu_2(\omega) &= -1 + \omega^2 \frac{\rho e^{-ikd}}{4\pi d}\nu_1(\omega),\end{aligned} \tag{1.33}$$

where ω is the angular frequency. Solution of equations (1.33) yields $\nu_1(\omega) = \nu_2(\omega) = \nu(\omega)$, then:

$$\nu(\omega) = \frac{-1}{\left(-\omega^2 m + ib\omega + \kappa - \omega^2 \frac{\rho e^{-ikd}}{4\pi d}\right)}. \tag{1.34}$$

Using Euler's identity in the coupling factor (i.e.,$\frac{\rho e^{-ikd}}{4\pi d}$), the damping and mass terms can be re-expressed as : $m_+ = m + \frac{\rho \cos kd}{4\pi d}$, $b_+ = b + \frac{\omega\rho \sin kd}{4\pi d}$. According to Feuillade (2001) both the coupling factor and the damping deviate little over the central peak of the bubble resonance spectrum, and may be assumed practically frequency independent. Therefore, replacing $\omega = \omega_0$ in b_+, m_+ and k, expression (1.34) yields:

$$\nu_+(\omega) = \frac{-1}{(-\omega^2 m_+ + i\omega b_+ + \kappa)}. \tag{1.35}$$

Performing the inverse Fourier transform of (1.35):

$$\nu_+(t) = -\frac{e^{-\alpha_+ t}}{m_+ \Omega_+} \sin \Omega_+ t. \tag{1.36}$$

Therefore, $\nu_+(t)$ represents the impulse response of the coupled system, where $\alpha_+ = \frac{b_+}{2m_+}$, $\Omega_+ = \sqrt{\omega_{0+}^2 - \alpha_+^2}$ and $\omega_{0+} = \frac{\omega_0}{\sqrt{1+\frac{a}{d}\cos\frac{\omega_{0+} d}{c}}}$.

1.4.3. Bubble cloud

1.4.3.1. Doinikov

Classically, the small-amplitude free radial oscillation of N coupled bubbles in a compressible medium is described by the following equations: (Leighton,1994)

$$\ddot{r}_i(t) + \omega_0 \delta \dot{r}_i(t) + \omega_0^2 r_i(t) = - \sum_{m=1, m \neq n}^{N} \frac{R_{j0}}{d_{nm}} \ddot{r}_j(t - d_{nm}/c), \tag{1.37}$$

where c is the sound speed in the water, d_{nm} indicates the distance between the n-th and m-th bubbles, and $\omega_0 \delta$ now represents the damping term. It should be noted that Eq. (1.37) is essentially the same as Eq. (1.27) under the assumption $R_{j0} \approx R_{i0}$, for an N-bubble system. In 2005, Doinikov et al. proposed the following approximation for the time delay:

$$\ddot{r}_j(t - \tau) = \ddot{r}_j(t) - \tau \dddot{r}_j(t). \tag{1.38}$$

Introducing this approximation would increase the order of Eq. (1.37). However, it is desirable to maintain the order of the original equation, reducing the order of Eq. (1.38). Let us note that the amplitude of the coupling term is negligible in comparison to the natural radiation. It is possible therefore to approximate Eq. (1.37) as:

$$\ddot{r}_i(t) \approx -\omega_0 \delta \dot{r}_i(t) - \omega_0^2 r_i(t). \tag{1.39}$$

Differentiating Eq. (1.39) and substituting into Eq. (1.38):

$$\ddot{r}_j(t - \tau) = (1 - \tau \omega_0 \delta)\, \ddot{r}_j(t) - \tau \omega_0^2 \dot{r}_i(t). \tag{1.40}$$

Substituting Eq. (1.40) into Eq. (1.37) leads to a non-delayed system. However, the approximation described in Eq. (1.38) may not be accurate enough for larger values of τ. According to Doinikov et al. (2005), it would be valid if $\tau \ll T_0$, where $T_0 = 2\pi/\omega_0$.

1.4.3.2. Ooi and Manasseh

Later, Ooi et al. (2008) published an extension of Doinikov's work, in which they analyzed the time delay effects on a linear bubble chain system, based on a method of finding the eigenvalues for time delay systems developed by Hu. (Hu et al.,1998) At first, let us analyze a 3 bubble case in an incompressible medium. Substituting a harmonic solution $ae^{\lambda t}$ into (1.37) gives:

$$
\begin{aligned}
&a_1\left[\lambda^2+\omega_0\delta\lambda+\omega_0^2\right]+\frac{R_0}{d_{12}}a_2\lambda^2+\frac{R_0}{d_{13}}a_3\lambda^2=0,\\
&\frac{R_0}{d_{12}}a_1\lambda^2+a_2\left[\lambda^2+\omega_0\delta\lambda+\omega_0^2\right]+\frac{R_0}{d_{23}}a_3\lambda^2=0,\\
&\frac{R_0}{d_{13}}a_1\lambda^2+\frac{R_0}{d_{23}}a_2\lambda^2+a_2\left[\lambda^2+\omega_0\delta\lambda+\omega_0^2\right]=0,
\end{aligned}
$$

which can be expressed in the form:

$$
\left[\lambda^2(\mathbf{I}+\mathbf{R})+\lambda\mathbf{C}+\mathbf{K}\right]\mathbf{A}=\mathbf{0}, \tag{1.41}
$$

where $\mathbf{C}=\omega_0\delta\mathbf{I}$, $\mathbf{K}=\omega_0^2\mathbf{I}$, $\mathbf{A}=\begin{bmatrix} a_1\\ a_2\\ a_3\end{bmatrix}$, $\mathbf{R}=\begin{bmatrix} 0 & \frac{R_0}{d_{12}} & \frac{R_0}{d_{13}}\\ \frac{R_0}{d_{12}} & 0 & \frac{R_0}{d_{23}}\\ \frac{R_0}{d_{13}} & \frac{R_0}{d_{23}} & 0\end{bmatrix}$, and $\mathbf{I}$ is the identity matrix.

Since $\mathbf{R}$ is a constant matrix, equation (1.41) will result in a conventional quadratic eigenvalue problem. In a compressible medium, $\tau_{mn}=d_{mn}/c$ denotes the time delay, where d_{mn} is the distance between the centers of the n-th and m-th bubbles. Harmonic solution yields to:

$$
\begin{aligned}
&a_1\left[\lambda^2+\omega_0\delta\lambda+\omega_0^2\right]+\frac{R_0}{d_{12}}a_2\lambda^2e^{\tau_{12}\lambda}+\frac{R_0}{d_{13}}a_3\lambda^2e^{\tau_{13}\lambda}=0,\\
&\frac{R_0}{d_{12}}a_1\lambda^2e^{\tau_{12}\lambda}+a_2\left[\lambda^2+\omega_0\delta\lambda+\omega_0^2\right]+\frac{R_0}{d_{23}}a_3\lambda^2e^{\tau_{23}\lambda}=0,\\
&\frac{R_0}{d_{13}}a_1\lambda^2e^{\tau_{13}\lambda}+\frac{R_0}{d_{23}}a_2\lambda^2e^{\tau_{23}\lambda}+a_2\left[\lambda^2+\omega_0\delta\lambda+\omega_0^2\right]=0.
\end{aligned}
\tag{1.42}
$$

In this case, the characteristic equation has the same form as in (1.41):

$$
\left[\lambda^2(\mathbf{I}+\mathbf{R}(\lambda))+\lambda\mathbf{C}+\mathbf{K}\right]\mathbf{A}=\mathbf{0},
\tag{1.43}
$$

where:

$$
\mathbf{R}(\lambda)=\begin{bmatrix}
0 & \frac{R_0}{d_{12}}e^{\tau_{12}\lambda} & \frac{R_0}{d_{13}}e^{\tau_{13}\lambda}\\
\frac{R_0}{d_{12}}e^{\tau_{12}\lambda} & 0 & \frac{R_0}{d_{23}}e^{\tau_{23}\lambda}\\
\frac{R_0}{d_{13}}e^{\tau_{13}\lambda} & \frac{R_0}{d_{23}}e^{\tau_{23}\lambda} & 0
\end{bmatrix}.
\tag{1.44}
$$

Since now $\mathbf{R}=\mathbf{R}(\lambda)$, equation (1.43) represents a nonlinear eigenvalue problem. Generalizing, in a N-bubble system, the conventional form to write these equation will be:

$$
\left[\lambda^2(\mathbf{I}+\mathbf{R}(\lambda))+\lambda\mathbf{C}+\mathbf{K}\right]\mathbf{A}_t=\mathbf{0}\rightarrow\mathbf{D}(\lambda_t,\tau_{nm})\mathbf{A}_t=0,
\tag{1.45}
$$

where λ_t and $\mathbf{A}_t$ are the eigenvalues and eigenvectors of the time delay system. If the times are neglected, $\tau_{nm}=0$ and:

$$
\left[\lambda^2(\mathbf{I}+\mathbf{R})+\lambda\mathbf{C}+\mathbf{K}\right]\mathbf{A}_r=\mathbf{0}\rightarrow\mathbf{D}(\lambda_r,0)\mathbf{A}_r=0.
\tag{1.46}
$$

The eigenvalues λ_r and eigenvectors $\mathbf{A}_r$ are the solution of a quadratic eigenvalue problem, and can be found by conventional methods. Hence, the following approximation is proposed for λ_t and $\mathbf{A}_t$:

$$\begin{aligned} \lambda_t &= \lambda_r + \Delta\lambda_r, \\ \mathbf{A}_t &= \mathbf{A}_r + \Delta\mathbf{A}_r. \end{aligned} \tag{1.47}$$

Once the eigenvalues λ_t and eigenvectors A_t of the time delay system are obtained, the time domain solution can be constructed by a linear combination:

$$r(t) = \sum_{n=1}^{N} \beta_n A_{n,t} e^{\lambda_{n,t} t}, \tag{1.48}$$

where β_n are constants to be determined from the initial conditions.

1.5. Primary Contributions

There is a critical difference between the characteristics of back scattering and forward scattering from schools of fish. This is due primarily to the occurrence, in the back scattering case, of constructive and destructive coherent interactions between the scattered fields of individual fish. These interactions lead to strong frequency dependent interference effects, which can significantly affect the amplitude of the back scattered field at low frequencies and, more specifically, at, and near to, the monopole resonance frequency. These coherent interactions are almost completely absent in the forward scattering case, where frequency dependent variations due to interference effects are not observed. (***Chapter 2***) The analysis described here assumes the acoustic data obtained by Diachok (1999) from the processing of his experimental measurements, and proposes a new interpretation of these data, using the analysis of acoustic forward scattering from schools of fish described in the present work. By analyzing the same data, and adopting basically the same biological assumptions and analytical approach as Diachok, but matching the data against a forward scattering model, rather than a back scattering model, it is shown that markedly different predictions are obtained for the number of individual fish in (the nucleus of) a school of sardines. The number of fish predicted is found to increase by as much as 60-200% (and possibly even more) for the cases examined here. (***Chapter 2***)

The effective medium method was used to investigate resonance scattering from schools of swim bladder fish, and compared with a coupled differential equation model which incorporates multiple scattering between fish and coherent interactions of their scattered fields. A theoretical comparison for idealized spherical schools showed good agreement in forward scattering, where interference effects have a minimal effect. Good agreement was also seen in back scattering at low frequencies, when the wavelength is significantly larger than the fish separation, specifically, $\lambda \geq 4s$. If $\lambda < 4s$, the models diverge in back scattering, and the effective medium method fails. Multiple scattering interactions are significant when $|4\pi n f_b^2/k| > 0.01$. A comparison with low frequency forward scattering data shows very good agreement for both models, and indicates a method for estimating fish abundance. For back scattering data, the effective medium method diverges strongly when $\lambda < 4s$. (***Chapter 3***)

The present work introduces a new method to find the impulse response of a bubble cloud in a compressible medium, based on perturbation theory.(McComb,2004) This method provides for an approximate solution to the problem, by starting from the exact solution of a related problem. The solution is formulated by adding a "small" term (or perturbation) to the mathematical description of the exactly solvable problem. (***Chapter 4***) The perturbation-based model was tested against experimental measurements of an artificial bubble cloud located near the surface of a shallow fresh water lake environment. The model shows good agreement with the experimental transfer function data, both in amplitude and frequency. First and second order boundary reflections were successfully incorporated to represent the variation in the peak amplitude registered by the different hydrophones. A numerical benchmark was also implemented, using a fourth order Runge-Kutta algorithm. The input consist of the impulse signal coming from the source and the multiple scattering among the bubbles. Two issues arise with the benchmark solution. The first one is the impulse implementation, which depends upon the impulsive function chosen. In the perturbation-based solution, the impulsive input is applied just to the soluble case, which can be solved analytically. Therefore, in this case there is no need to create an impulse function to solve the equation. The second issue is related to stability. For the

tested case, the numerical benchmark was less stable than the perturbation-based solution. (***Chapter 4***)

1.6. Thematic outline of dissertation

Chapter 2 provides a detailed analysis of the physical properties and the frequency variation of the forward scattered field and the extinction coefficient for ensembles of swim bladder fish, using the CDE approach. Chapter 2 also gives an overview of the assumptions and parameters used in the data analysis (Diachok,1999), describes how the new analysis was performed, and compares the results of the new interpretation of the data with those previously described by Diachok. Chapter 3 provides a theoretical comparison between the CDE and EM models, including the idealized spherical fish school example presented by Hahn (2007). It also compares both models with experimental data, and discusses the applicability and limitations of the effective medium approach. Chapter 4 presents a new method to calculate the impulse response of a near surface bubble cloud in a compressible medium and in the presence of a reflective bottom, based on perturbation theory. It also describes the experiment that was conducted to test the model, and how the data was analyzed. Once the model is implemented, a comparison with the experimental data, and a second comparison with a numerical benchmark calculation, are also offered. This is followed by a summary of conclusions from the work (Chapter 5).

2. SOUND EXTINCTION BY FISH SCHOOLS: FORWARD SCATTERING THEORY AND DATA ANALYSIS

2.1. Analysis of the forward scattered pressure for ensembles of swim bladder fish

2.1.1. Two fish ensonified with the same phase

Two factors which strongly affect radiative coupling between fish in a school, and scattering from the school as a whole, are the depth of the fish in the water column, and the nearest-neighbor spacing of the fish. To study these effects independently of other important factors, such as the variable external field phase applied to each individual fish, and the total number of fish in the school, the case of two identical and interacting swim bladder fish, both ensonified by a common external harmonic field with the same phase, is first considered. Since there is no phase difference in the ensonification of the two fish, the individual scattered field amplitudes from the two fish are equal. Solution of Eqs. (1.12) yields:

$$p_{s1} = p_{s2} = \frac{P_0}{r} \frac{a}{\left(\frac{\omega_0^2}{\omega^2} - 1 + i\delta\right) - \frac{a}{s} e^{-iks}}, \tag{2.1}$$

where s is the separation distance between the two fish (i.e., between the swim bladders). From this equation a modified resonance frequency, common to both fish, may be obtained, as shown by Feuillade (2001) i.e.,

$$\omega_{0+} = \frac{\omega_0}{\left[1 + \left(\frac{a}{s}\right) \cos \frac{\omega_{0+} s}{c}\right]^{1/2}} \, . \tag{2.2}$$

In this equation, the numerator corresponds to the resonance frequency of an individual uncoupled fish, while the denominator describes the effects of the interaction between the fish. The cosine term in the denominator introduces an oscillatory factor which depends on s. In general, where two fish are ensonified with arbitrarily different phases, the resultant motion may be expressed as a superposition of two modes: the symmetric mode ("+"), where the swim bladders oscillate in phase with each other; and the antisymmetric mode ("−"), where they oscillate in antiphase.(Feuillade,1995) In the present case only the symmetric mode is excited, and it is typically found that ω_{0+} is less than ω_0 for fish ensembles near the

surface, since $\frac{\omega_{0+}s}{c} < \pi/2$ for the small separations s between neighboring fish in a closely packed school.(Feuillade,1995) However, at greater depth, ω_0 may increase substantially, particularly in the case of physostomes, where the swim bladder volume typically varies inversely with the depth . As the swim bladder volume (and radius a) decreases, its resonance frequency, as described by $\omega_0 = (1/a)\sqrt{3\gamma P_A/\rho}$, increases, and ω_0 also increases due to the increase in P_A with depth. It is therefore possible that, depending on the depth of the fish, $\omega_{0+} > \omega_0$.

Later in the present work, a reanalysis of experimental data by Diachok for sardines, which are physostomes, of effective modal length 16.5 cm, and with swimbladder aspect ratio ≈ 12, is performed. (Diachok,1999) In Figure 2.1, and henceforward, these properties are implicitly assumed for the modeling cases discussed. In particular, the swimbladder aspect ratio of 12 gives rise to a 28% increase in the observed resonance frequency, as predicted by Weston's equation, i.e., Eq. (1.7).

Figure 2.1 shows the frequency variation of the absolute scattering amplitude $|\mathrm{f}_s|$ for two identical fish, where the separation $s = L = 16.5$ cm, where L is the length of the fish. The fish are ensonified in phase, and were both positioned at: (a) 25 m depth; and (b), 60 m depth. Whereas the swim bladder radius of these fish at the surface is $a_0 = 7.9$ mm; at 25m depth, and 60m depth, the swim bladder radius is reduced by compression to 5.2 mm, and 4.1 mm, respectively. In the first case, at 25 m depth, the theoretical resonance frequency of a single fish (see the dashed line) is 1478 Hz, while the reduced resonance frequency of the coupled pair is 1465 Hz, i.e., $\omega_{0+} \approx 0.99\omega_0$. At 60 m depth, the resonance frequency of the coupled pair increases slightly from 2633 Hz (for a single fish) to 2642 Hz, so that $\omega_{0+} \approx 1.003\omega_0$. While the difference between ω_{0+} and ω_0 is small in both cases, this effect increases with the number of fish in the ensemble, and becomes significant for the numbers of fish typically observed in fish schools in the sea.

As indicated by Eq. (2.2), another factor which affects the resonance frequency of the coupled fish is the separation s. In Figure 2.1, s = L (i.e., $s/L = 1$); and in Figure 2.2, the variation of the resonance frequency for two identical coupled fish for variable s/L, as

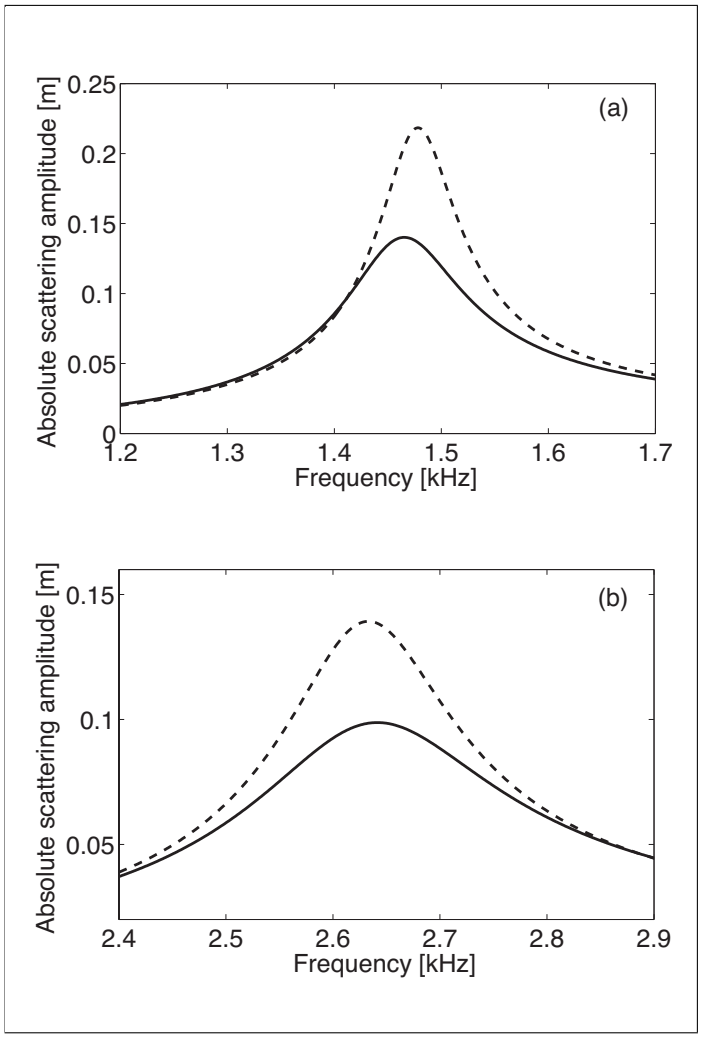

FIGURE 2.1. Absolute scattering amplitude $|f_s|$ due to two identical fish oscillating: (a) in phase, at 25 m depth; (b)in phase, at 60 m depth. In both cases, the solid line indicates the response of a pair of coupled fish, and the dashed line indicates the response of a single uncoupled fish multiplied by two.

described by Eq. (2.2), is shown. The frequency changing effect decreases as s increases, as indicated by Eq. (2.2), and the coupled resonance frequency may be either greater, or lower, than the resonance frequency of a single fish, depending on the depth and the separation.

2.1.2. Two fish ensonified with arbitrary phase

In the case of real fish schools, containing many individuals, the scattering is influenced by both the number of fish, and the variation of phase of the applied field across the

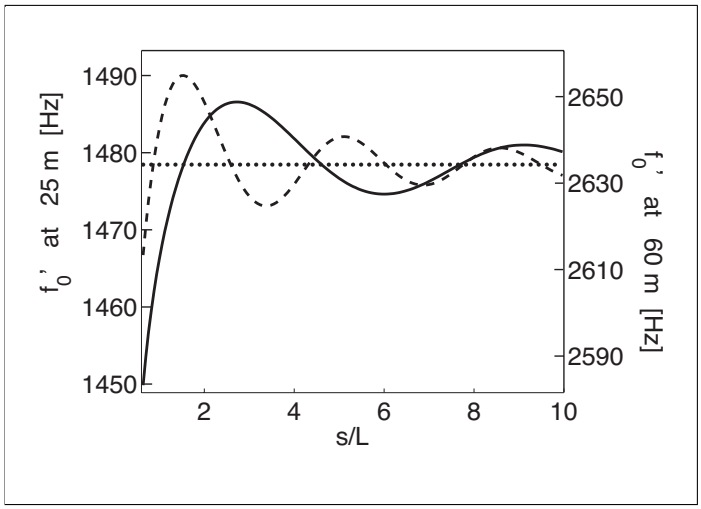

FIGURE 2.2. Resonance frequency, in [Hz], of two coupled identical fish oscillating in phase with each other, as a function of the separation s between them, calculated using Eq. (2.2). Solid line: the fish are located at 25 m depth. The left vertical axis indicates the corresponding frequency scale. Dash line: the fish are located at 60 m depth. The right vertical axis indicates the corresponding frequency scale. The horizontal line indicates the resonance frequency of a single fish, i.e., 1478 Hz at 25 m depth, and 2634 Hz at 60 m depth

school. In this section the effect of variable phase differences on the resonances of spatially distributed ensembles of fish is analyzed. It is helpful to do this first for two fish, and then extend the analysis to larger ensembles.

In the case of two fish, it is assumed that the source, the fish, and the receiver, are all located along a common axis. This ensures that the distances between the source and each fish are distinct, which necessarily introduces a phase difference in phase between the external fields applied to them. Figure 2.3 depicts, in schematic form, the ensonification of the two fish in this configuration. It will be seen, after solving Eqs. (1.12), that the received scattered pressure depends on the receiver position relative to the source.

If the source and receiver are co-located (the backscattering case), the pressure field radiated by each fish is given by:

$$p_{bs1} = P_0 e^{-2ikR_{S1}} \frac{a}{R_{R1}} \frac{\left(\frac{\omega_0^2}{\omega^2} - 1 + i\delta\right) + \frac{a}{s}e^{-2iks}}{\left(\frac{\omega_0^2}{\omega^2} - 1 + i\delta\right)^2 - \left(\frac{a}{s}e^{-iks}\right)^2} \quad ; \tag{2.3}$$

$$p_{bs2} = P_0 e^{-2ikR_{S2}} \frac{a}{R_{R2}} \frac{\left(\frac{\omega_0^2}{\omega^2} - 1 + i\delta\right) + \frac{a}{s}}{\left(\frac{\omega_0^2}{\omega^2} - 1 + i\delta\right)^2 - \left(\frac{a}{s}e^{-iks}\right)^2} \quad , \tag{2.4}$$

where p_{bs1} represents the pressure scattered by fish 1 (nearer to the source) and p_{bs2} represents the pressure scattered by the fish 2 (further from the source), R_{S1} and R_{S2} are the distances from the source to the two fish, s is again the fish separation, and R_{R1} and R_{R2} are the distances from the two fish to the receiver.

Equations (2.3) and (2.4) show that the back scattered pressure fields p_{bs1} and p_{bs2} contain several frequency varying phase terms. First, there is a phase due to the radiative interaction between the fish, i.e., e^{-2iks}, which appears in the denominator of both equations, and also in the numerator of Eq. (2.3). Second, there are two other phase terms, different for each fish, which depend on the distance between the fish and the source, i.e., $e^{-2ikR_{S1}}$, and $e^{-2ikR_{S2}}$. When the two back scattered pressure fields are detected at the receiver, these add coherently and, as a result of the path difference between R_{S1} and R_{S2}, they interfere either constructively or destructively depending on the frequency, leading to a "comb filter" effect, with periodicity equal to $\frac{c}{2s}$ rad/s.

If the receiver is located on the opposite side of the two fish than the source (the forward scattering case), the scattered pressures for the two fish are:

$$p_{fs1} = P_0 e^{-ikR_{SR}} \frac{a}{R_{R1}} \frac{\left(\frac{\omega_0^2}{\omega^2} - 1 + i\delta\right) + \frac{a}{s}e^{-2iks}}{\left(\frac{\omega_0^2}{\omega^2} - 1 + i\delta\right)^2 - \left(\frac{a}{s}e^{-iks}\right)^2} \quad ; \tag{2.5}$$

$$p_{fs2} = P_0 e^{-ikR_{SR}} \frac{a}{R_{R2}} \frac{\left(\frac{\omega_0^2}{\omega^2} - 1 + i\delta\right) + \frac{a}{s}}{\left(\frac{\omega_0^2}{\omega^2} - 1 + i\delta\right)^2 - \left(\frac{a}{s}e^{-iks}\right)^2} \quad , \tag{2.6}$$

where R_{SR} is the source-receiver distance.

Here it is seen that, while Eqs. (2.5) and (2.6) still contain terms with the e^{-2iks} factor due to the radiative interaction, exactly as in Eqs. (2.3) and (2.4), they both now contain the same phase term $e^{-ikR_{SR}}$. Therefore, when they add coherently at the receiver in the

forward direction, there are no interference variations due to the different distances between the source and the two fish.

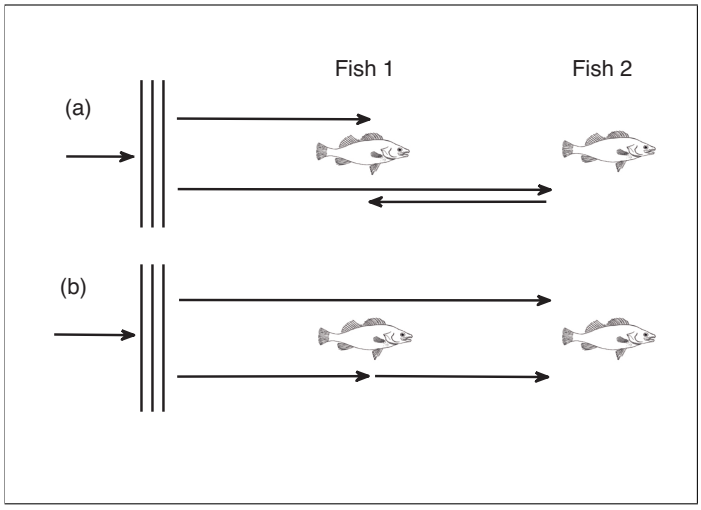

FIGURE 2.3. Ensonification of two identical fish lying along an axis between the source and receiver:(a) field contributions on the fish nearest from the source;(b) field contributions on the fish furthest to the source.

There is, however, an important difference between Eqs. (2.5) and (2.6). Fish 2 is ensonified by the external pressure field, and also by the field reradiated by fish 1, in such a way that the distance travelled by the waves is the same in both cases [see Fig. 2.3(b)]. Therefore, no phase is introduced between these two components due to differences in the propagation paths. In contrast, the distance traveled by the incident field directly from the source to fish 1 is not the same as the distance traveled to fish 2 plus the distance traveled by the reradiated field back to fish 1. In this case, there is a path difference of $2s$ [see Fig. 2.3(a)]. The effect of the extra propagation distance for the reradiated field is seen in the incorporation of a factor e^{-2iks} in the second term of the numerator in Eq. (2.5), which does not appear in Eq. (2.6). Typically, $R_{R1}, R_{R2} \gg s$, so the approximation $R_{R1} = R_{R2} = R$ can be applied, and if the common phase $e^{-ikR_{SR}}$ is neglected, Equ ations (2.5) and (2.6) may be rewritten as $p_{fs1} = p_{s0} + p_{s21}$ and $p_{fs2} = p_{s0} + p_{s12}$, where:

$$p_{s0} = \frac{aP_0}{R} \frac{\left(\frac{\omega_0^2}{\omega^2} - 1 + i\delta\right)}{\left(\frac{\omega_0^2}{\omega^2} - 1 + i\delta\right)^2 - \left(\frac{a}{s}e^{-iks}\right)^2} \quad ; \tag{2.7}$$

$$p_{s21} = \frac{aP_0}{R} \frac{\frac{a}{s}e^{-2iks}}{\left(\frac{\omega_0^2}{\omega^2} - 1 + i\delta\right)^2 - \left(\frac{a}{s}e^{-iks}\right)^2} \quad ; \tag{2.8}$$

$$p_{s12} = \frac{aP_0}{R} \frac{\frac{a}{s}}{\left(\frac{\omega_0^2}{\omega^2} - 1 + i\delta\right)^2 - \left(\frac{a}{s}e^{-iks}\right)^2} \quad , \tag{2.9}$$

and p_{s0} corresponds to the scattering due to each fish itself, p_{s21} describes the reradiated pressure from fish 2 to fish 1, and p_{s12} is the reradiated pressure from fish 1 to fish 2. These three expressions describe the resultant values of these quantities after radiative coupling effects are included.

Figure 2.4 shows a phase analysis for equations (2.7) to (2.9). Two identical fish lying along an axis between the source and receiver, with $s = L$, were considered. Both fish were located at 60 m depth. The upper figure describes the phase behavior for fish 1, where the solid line indicates the phase response of the component p_{s0}, and the dashed line indicates the phase of p_{s21} [i.e., the two components of Eq. (2.5)]. The lower figure describes the behavior for fish 2, where the solid line again indicates the phase of p_{s0}, while the dashed line now indicates the phase of p_{s12} [the two components of Eq. (2.6)]. Figure 2.4(b) shows that the two components of p_{fs2} [see Eq. (2.6)] are practically in anti-phase (i.e., there is a phase difference of π between them) above the resonance frequency. This leads to destructive interference between the two components for fish 2 (p_{s0} and p_{s12}) in the region above resonance. In Figure 2.4(a), which shows the behavior of the two components of Eq. (2.5), the same effect is not seen, due to the additional phase factor e^{-2iks} in Equation (2.8). These phase effects have two important consequences. First, the resonance peak for fish 2 is apparently shifted down to a frequency below the original resonance frequency for a single fish. Second, the scattering behavior of fish 2 is inhibited, and the energy scattered from it is reduced. It is shown below that, as the number of fish in the school increases, this latter effect leads to the appearance of a "hole" in the overall resonance response of the school in the region of the original resonance frequency.

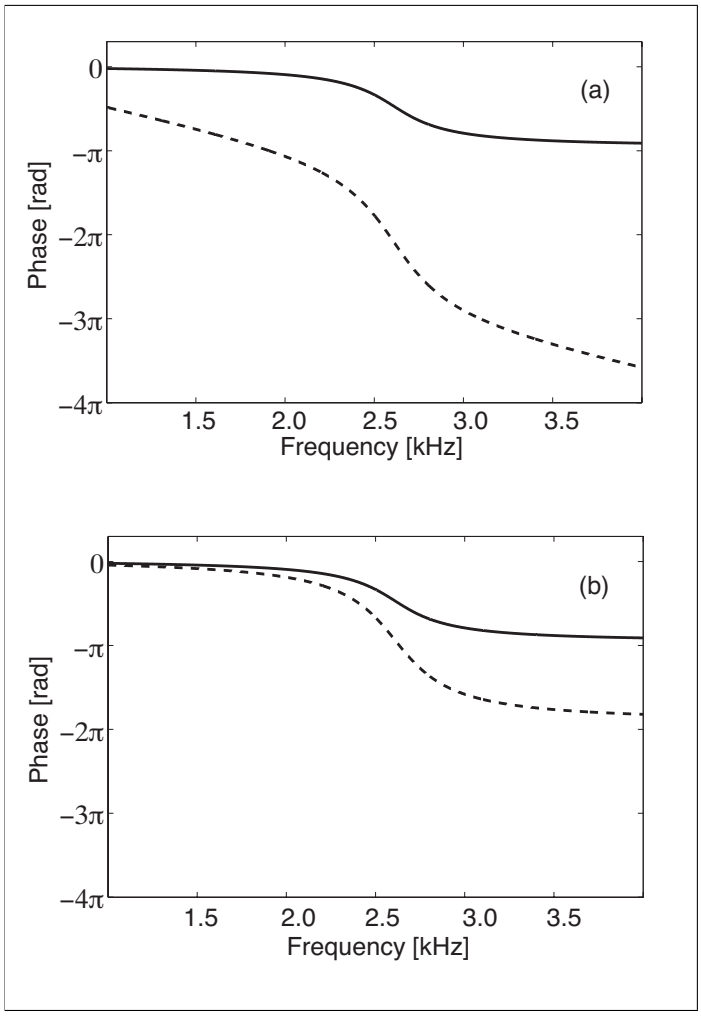

FIGURE 2.4. Phase response of p_{s0} , p_{s12} , p_{s21} [see eqs. (2.7),(2.8),(2.9)]. In both figures, the solid line indicates the phase response of p_{s0}. (a) Fish nearest to the source, at 60 m depth. The dashed line indicates the phase of the interaction p_{s21} (b) Fish furthest from the source, at 60 m depth. The dashed line indicates the phase of the interaction p_{s12}.

2.1.3. Larger schools

Figure 2.5(b) indicates the projections on the xz plane of the randomized individual fish locations within a spherical ensemble of 500 fish. The ensemble is positioned in the far field of the source, and the ensonifying field is understood to be incident from the LHS. As a result of the geometry, each fish is ensonified with a different phase. Figure 2.5(a) shows the frequency variation of the absolute scattering amplitude $|\mathrm{f}_s|$, evaluated in the forward

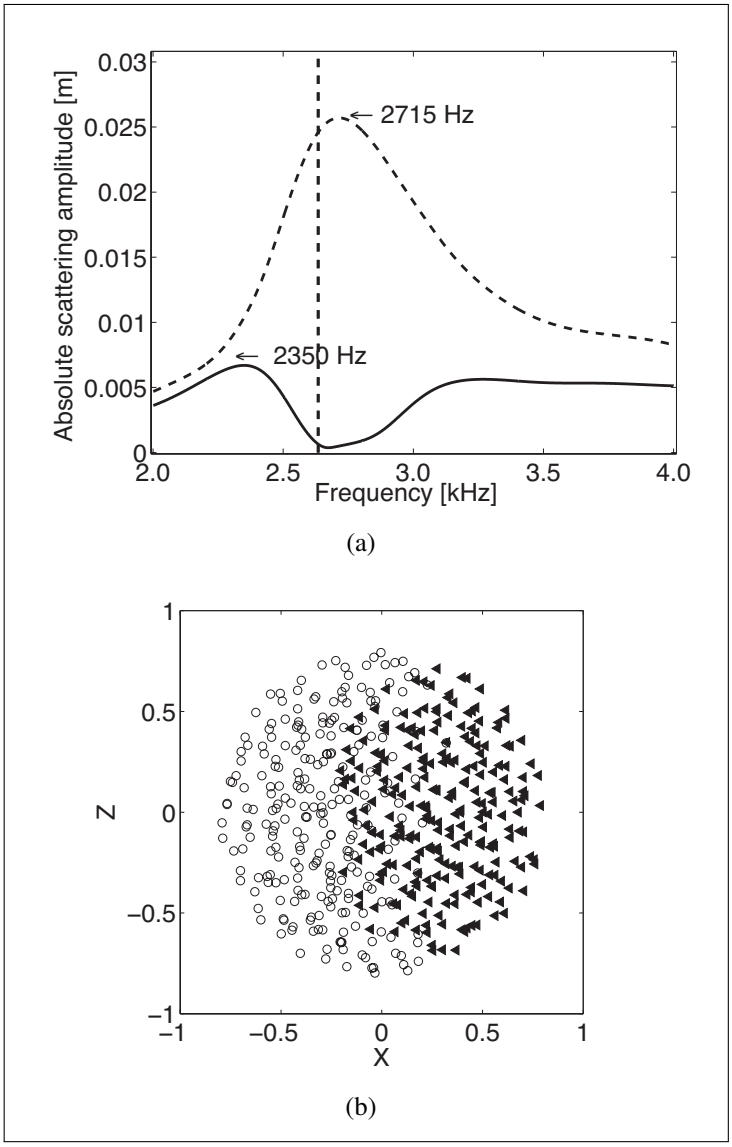

FIGURE 2.5. (a) Frequency variation of the absolute scattering amplitude $|\mathrm{f}_s|$ evaluated in the forward direction of two fish from a spherical school of 500 fish, with their corresponding peak resonance frequencies indicated. Dashed line: the fish with the highest scattered energy. Solid line: the fish with the lowest scattered energy. (b) Spatial configuration of the fish school. This figure shows the projections on the xz plane of the individual fish locations. The source and receiver lie on the x axis. The source is located on the LHS of the fish (with negative x) and the receiver lies on the RHS (with positive x). The triangles indicate the 250 lowest-energy radiating fish.

direction, for two of the 500 fish: that with the *highest* scattered energy (dashed line); and that with the *lowest* scattered energy (solid line), where radiative interactions between the

fish have been incorporated using the school scattering model. It is seen that the resonance response of the low energy fish shifts down in frequency, and that the absolute scattering amplitude is suppressed. Note also the appearance of a "hole" in the scattering response for this fish near the original resonance frequency. In contrast, the response of the high energy fish does not show these effects, and its resonance frequency is almost identical to the original resonance frequency of an individual fish. The 250 fish with the lowest scattered energies in the ensemble are indicated by triangles in Figure 2.5(b). These fish are seen to lie predominantly on the side of school nearer to the receiver (i.e., on the RHS of the figure, since the external field is incident from the LHS). The resonances of these fish are suppressed due to interference effects, in essentially the same way that the resonance of fish 2 was suppressed in the two fish case discussed above.

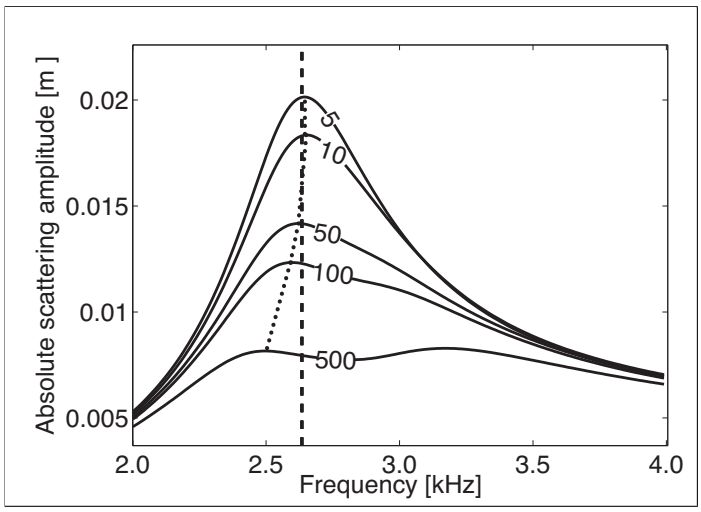

FIGURE 2.6. Effect of school size on absolute scattering amplitude $|\mathrm{f}_s|$. Normalized scattering amplitude for spherical schools containing 5, 10, 50, 100 and 500 fish. In each case the normalized absolute scattering amplitude is obtained by dividing the absolute scattering amplitude calculated for the whole school by the number of fish in the school. The vertical line indicates the theoretical resonance frequency for an individual fish. The dotted line indicates the downward shift of the peak frequency as the number of fish is increased.

Figure 2.6 shows the frequency variation of the normalized absolute scattering amplitude evaluated in the forward direction (obtained by dividing the absolute scattering amplitude $|\mathrm{f}_s|$ for the whole school by the number of fish) for spherical schools with 5, 10,

50, 100 and 500 fish. The figure shows that, as the number of fish is increased, the peak frequency of the overall school resonance response decreases, and a hole in the region of the original resonance frequency (indicated by the dashed line) progressively emerges. As this hole develops, this leads to the appearance, on the high frequency edge of the hole, of a feature that imitates a second higher frequency peak. These phenomena are due to interference effects, which change the resonance behavior of fish nearer to the receiver, as previously discussed.

2.1.4. Comparison of the back scattered and forward scattered field

The acoustic behavior of the back scattered field from schools of fish was discussed at length by Feuillade et al. (1996). Application of the school model led to three general conclusions: (a) there is typically a reduction in the target strength at frequencies close to the resonance frequency of the individual fish; (b) there is a reduction in the observed resonance peak frequency compared to that seen with incoherent scattering; (c) there are variations in the target strength as a function of frequency, that become greater as the number of fish increases, due to interference between the radiated fields of the individual fish.

Figure 2.7 shows the frequency variation of the absolute scattering amplitude $|\mathrm{f}_s|$ averaged over 10 different random spherical schools of 500 fish ($L = 0.165$ m, $a_0 = 7.9$ mm), at 60 m depth. The parameter s is now used to denote the average nearest-neighbor spacing between fish in the school. In Figure 2.7 a mean value of $s = L$ is used. In this case, and henceforward, s is allowed to vary randomly according to a Gaussian distribution with a standard deviation of 10% of the nominal average spacing s. In Figure 2.7, radiative interactions between the fish have been incorporated using the school scattering model. Figure 2.7(a) shows the back scattering case, and Figure 2.7(b) shows the forward scattering case. The dashed vertical line, in both figures, indicates the resonance frequency of an individual fish at 60 m depth. It is seen that, in back scattering, interference effects degrade and modify the resonance response in a way that may frequently make identification of the actual school resonance peak problematic. However, in the forward direction, the scattered field is free of interference effects. The resonance peak of the school is clearly identified as

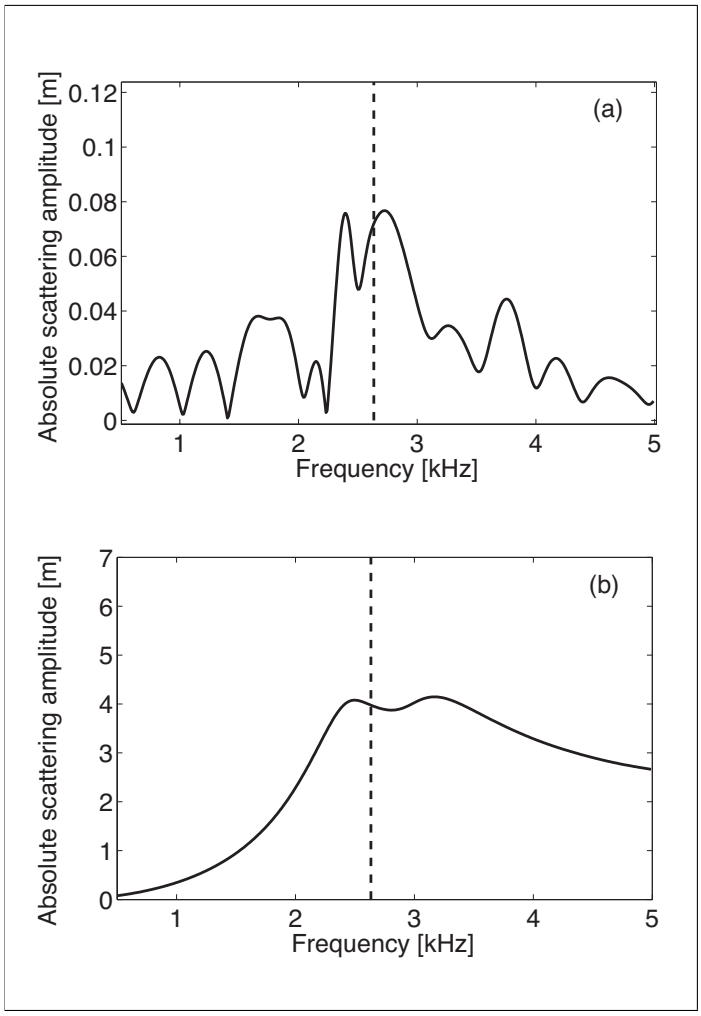

FIGURE 2.7. Absolute scattering amplitude $|f_s|$ of a spherical school of 500 fish, at 60 m depth (a) Back scattering (b) Forward scattering. Note the different scales for absolute scattering amplitude on the vertical axes.

the lower frequency component of the two peak features indicated in the figure. It can also be seen, by noting the different scales for the absolute scattering amplitude on the vertical axes of Figure 2.7(a) and Figure 2.7(b), that acoustical scattering in the forward direction is generally much stronger than back scattering, indicating there is also significant angular variation in scattering from the school.

2.1.5. Influence of the shape of the school on the forward scattering amplitude

While the low-frequency scattered field of a single fish is predominantly spherically symmetric, Figures 2.7(a) and 2.7(b) indicate that the acoustical scattering behavior of an ensemble of fish will typically show a strongly directional variability, even for spherical schools. This is also implied by Figure 2.5(b), which indicates that the scattering amplitude of an individual fish depends on its relative position, both within the school, and along the source-receiver axis.

The acoustic forward scattering behavior of schools of three different configurations is now compared. First, a spherical school is considered, which is positioned in the far field of the source. Its absolute forward scattering amplitude is calculated, as in cases discussed previously. Second, an oblate spheroidal school is considered, which is ensonified along a direction perpendicular to the axis of rotational symmetry. Third, an oblate spheroidal school is again considered, but is ensonified along a direction parallel to the axis of rotational symmetry. The three cases are depicted in Figure 2.8.

The oblate spheroids were generated by rotating an ellipse of aspect ratio $\alpha = 3$ by 180 degrees around the minor axis, which is orientated to lie in the z direction. The dimensions of the schools were varied by adjusting the parameters r_x, r_y, r_z, which, if the spheroid is centered at the origin, are given by the points of interception of the surface of the spheroid with the positive x, y, and z, axes, respectively. All of the schools were generated to contain 500 fish, with nearest neighbor spacing $s = L$.

Figure 2.9 shows the average frequency variation of the forward scattered pressure field (i.e., the absolute scattering amplitude $|\mathrm{f}_s|$ computed in the forward direction) of 10 different randomizations for each type of school. Curve 1 represents the forward scattering distribution for a spherical school of 500 fish. It shows the characteristic two peaked distribution, and overall reduced scattering level, previously shown in Figure 2.6. Curve 2 is the corresponding distribution for an oblate spheroidal school, again of 500 fish, ensonified perpendicularly to its axis of rotation [see Figure 2.8(b)]. It is seen that the effect of changing from the spherical to the oblate spheroidal form in this orientation is to further suppress

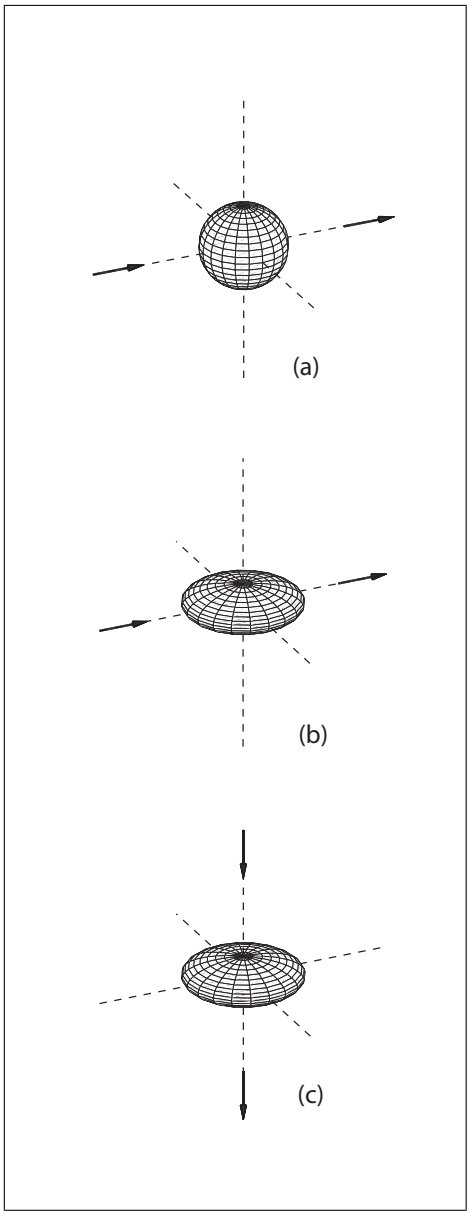

FIGURE 2.8. Spatial configuration of school containing 500 fish at $s = L$. (a) Spherical school, radius $r = 0.8124$ m. (b) Oblate spheroidal school, radius $r_x = r_y = 1.1717$ m, $r_z = 0.3906$ m, ensonified along a direction which is perpendicular to its axis of rotational symmetry (c) Oblate spheroidal school, radius $r_x = r_y = 1.1717$ m, $r_z = 0.3906$ m, ensonified along a direction parallel to its axis of rotational symmetry.

the overall level of the scattering distribution, but also to increase the relative height of the

low frequency peak with respect to this level. In the previously discussed case of a spherical school containing 500 fish [cf. Figure 2.5(a)], it was shown that the low frequency peak, and the suppression of scattering, is typically generated by those fish in the school which are nearer to the receiver. With the oblate spheroidal school in the present orientation, more of the fish are distributed close to the xy plane, because the minor axis is orientated in the z direction. Also, the propagational distance over which the fish interact with the incident field as it passes through the school is increased. These two factors combine to enhance the phase effects previously observed for the spherical schools, and to further accentuate the low frequency peak, and the overall scattering suppression, seen in those cases.

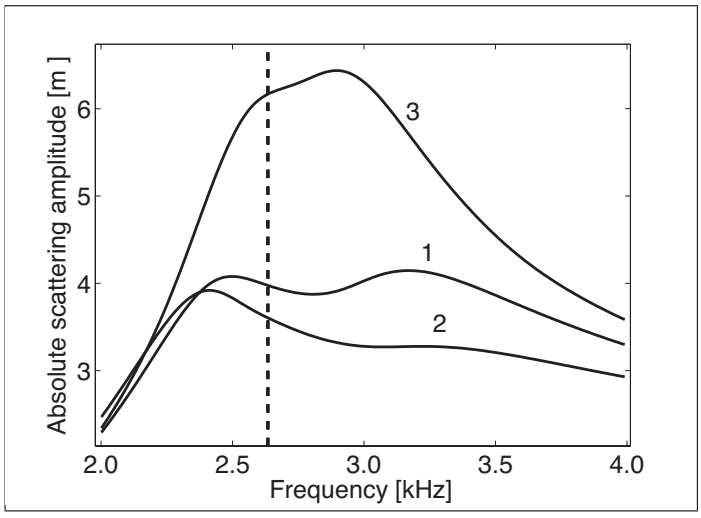

FIGURE 2.9. Absolute forward scattering amplitude for a school of 500 fish, at 60 m depth. (1) Spherical school, corresponding to Fig 2.8(a). (2) Oblate spheroidal school [Fig 2.8(b)]. (3) Oblate spheroidal school [Fig 2.8(c)].

In contrast, curve 3 shows the frequency distribution obtained when the school is ensonified along its axis of rotation, i.e., along its minor axis [see Figure 2.8(c)]. In this case, the effect of the oblate school is to de-emphasize the low frequency peak, and to increase the overall scattering level from that of the spherical school (curve 1). The explanation is the opposite of that for curve 2. When the oblate spheroidal school is ensonified in this second orientation, the propagation distance over which the incident field interacts with the fish is shortened, and the phase cancellation effects on the fish nearer to the receiver are correspondingly reduced.

2.1.6. Extinction cross section

The extinction cross section (σ_e), represent the total power loss from the incident wave due to scattering and absorption by the fish in the school. According to the "extinction" theorem, also called the "forward scattering" theorem or the "optical" theorem,(Ishimaru,1997) this loss is directly related to the behavior of the scattered wave in the forward direction:

$$\sigma_e = \frac{4\pi}{k}\mathrm{Im}\{\mathrm{f}_s(0,0)\}; \tag{2.10}$$

where "Im" denotes the "imaginary part of" and $\mathrm{f}_s(0,0)$ is the school scattering amplitude evaluated in the forward scattering direction, i.e. in the direction of the incident field. The SI unit for the extinction cross section is meters squared. Figure 2.10 shows the simulation of the average absolute scattering amplitude and extinction cross section, calculated using Eqs. (1.16) and (2.10), for a set of 10 randomized spherical schools of 500 fish, with $s = L$. Curves 1 and 2 represent the absolute scattering amplitude $|\mathrm{f}_s|$ in the forward direction, and the extinction cross section, respectively. It was seen, in Figure 2.7, that the absolute scattering amplitude is considerably greater for the forward scattered field than for the back scattered field. This behavior is consistent with the amplitudes of curves 1 and 2 in Figure 2.10.

2.2. Data analysis

In the 1999 article by Diachok, a careful and comprehensive analysis of acoustic transmission data obtained during the Modal Lion experiment, performed in the Gulf of Lion in the Mediterranean Sea in September 1995, is presented. The purpose of this analysis was to study absorption due to fish in shallow water ($\sim$80 m depth) over a range of about 12 km, by isolating their sound attenuation effect from the overall propagation losses measured in the experiment.

It is clear from the design of Diachok's experiment that the acoustic source was placed on one side of the ensembles of fish in the water column, and that the sound then passed through these fish before being received at a hydrophone array placed on the opposite side.

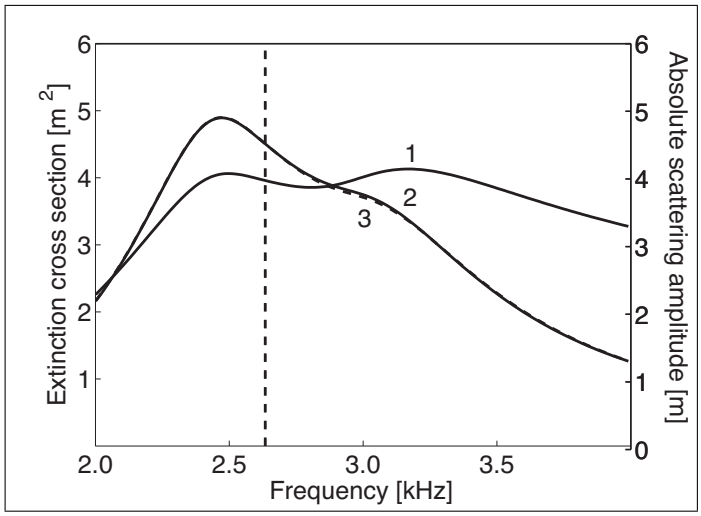

FIGURE 2.10. Curve 1: Absolute scattering amplitude $|\mathrm{f}_s|$ for a spherical school of 500 fish, evaluated in forward direction, at 60 m depth. Curve 2: Extinction cross section for a school of 500 fish, at 60 m depth, random packing arrangement. Curve 3 (the dashed curve almost completely hidden by curve 2): Extinction cross section for a school of 500 fish, at 60 m depth, body-centered cubic arrangement.

The transmitted acoustic signals were modified by their interactions with the ensembles of fish as they passed through them, and these modified signals were subsequently received at the array. The signals, when analyzed, thereby provide a measurement of the extinction of sound by the fish, and therefore should lead to estimates of the extinction coefficient for individual fish, and for fish ensembles, including fish schools. From the extinction theorem,(Ishimaru,1997) it is clear, therefore, that the properties of the attenuated sound received at the array are characterized by the *forward scattering* behavior of the ensembles of fish.

In the analysis described by Diachok (1999) curves are presented which indicate the absorption coefficient α_b at different depths in the water column where fish are located, obtained by matching the measurements with a computational model of transmission loss for the environment where the experiment was performed. These curves are functions of frequency, where the maxima are associated with the resonance frequencies of the various ensembles of fish in the water column. However, an analysis of this data is then performed

that produces estimates of the number of fish in a school based upon modeling of the back scattering properties of fish schools, i.e., *not* the forward scattering properties.

The method used by Diachok to estimate the abundance of sardines in a school, depends on identifying the peak frequency of the collective resonance of the school, which typically shifts down to a lower frequency than that of an individual fish, due to radiative coupling between the fish swim bladders. The magnitude of this shift effect increases as the number of fish in the school is increased, and it also increases as the nearest-neighbor spacing between fish in the school is reduced. Once the peak frequency of the collective school (i.e., nucleus) resonance is identified, Diachok then infers the number of fish in the school by matching the shifted collective resonance frequency against that predicted by a semi-empirical equation, modified from an equation given by d'Agostino and Brennan (1988) for the frequencies of the normal modes of a bubble cloud. To determine the parameters of the semi-empirical equation, and obtain estimates of the number of sardines in a school, Diachok used the resonance frequencies for fish schools derived from the published back scattering work of Feuillade et al. (1996), and also some unpublished back scattering computations of Nero, which he cites as a personal communication.

In his paper, Diachok cites the work of Misund (1991), who mapped the internal structure of schools of herring using a high resolution sonar. Misund's results show that schools typically consist of an inner core region (the "nucleus" of the school), in which the average nearest-neighbor separation between fish is usually approximately equal to the fish length, and an outer peripheral region where the average separation is significantly larger than the fish length. The "nucleus" constitutes about half the volume of schools. Diachok notes, in his work on sardines, that his measurements manifest pairs of absorption lines per layer of fish. One line is attributed to the resonance frequencies of individual sardines, and the second line is attributed to the resonance frequencies of an ensemble of "nuclei" of schools, which is consistent with Misund's work. It is important to bear in mind, however, that when Diachok subsequently analyzes his data to estimate the number of sardines in a "school," he is actually referring to an analysis of the specific data which lead to estimates of the number of sardines in the "nucleus" of the school, not of the entire school.

In the area where the Modal Lion experiment was performed, ensembles of both sardines and anchovies were identified. According to Diachok, the acoustic effects of sardines dominate the echosounder data, presumably because there were about twice as many sardines as anchovies present, and because their target strength is about twice that of anchovies. He indicates that, in general, it is improbable that the absorption lines he found are due to the presence of dispersed or schooling anchovies, although they could contribute to other absorption lines. For this reason, following Diachok, the analysis in the present work is focused on schools of sardines.

The analysis described here assumes the acoustic data obtained by Diachok from the processing of his experimental measurements, and proposes a new interpretation of these data, using the analysis of acoustic forward scattering from schools of fish described in the present work. In the conclusions section of his paper, Diachok (1999) acknowledged a number of topics used in his theory and analysis which require further work to improve its prescriptive capability. The work described here is intended to partially supply this need, by developing a model of the extinction cross section of fish schools, and refining the analytical model of the resonance frequency of the school.

2.2.1. Brief review of parameter inputs for the Modal Lion analysis

To analyze measurements from the Modal Lion experiment, it is first necessary to determine a number of input parameters, to provide a starting point to run the school scattering model. The model requires information about the length of the individual fish, the size of the swim bladder, and the viscosity of fish flesh surrounding the swim bladder. To model the fish schools themselves, it is necessary to know the shape and dimensions of the schools, the nearest-neighbor separation between the fish s, and the depth of the school in the water column.

It is important to distinguish between those parameters which may be determined directly from sampling measurements, and from other experimental data (some of which were obtained as part of the Modal Lion experiment itself), and those parameters which must be inferred by indirect means, e.g., from the literature. In his paper, Diachok gives an

extensive discussion and evaluation of the available literature. The articles he cites in this review, and the topics of the information which he incorporates in his analysis, are summarized in Table 2.1. In the reanalysis of Diachok's absorption data reported in the present work (to be detailed below), both his approach and reasoning have been generally followed when deriving input parameters for the school scattering model.

TABLE 2.1. Articles referred to by Diachok

Year	Author	Topic
1971	Culley (1971)	Depth of dispersed sardines
1996	Barange et al. (1996)	Depth of dispersed sardines
1993	Pitcher and Parrish (1993)	Structure of school
1985	Pitcher et al. (1985)	Structure of school
1985	Azzali et al. (1985)	Structure of school
1991	Misund (1991)	Structure of school
1996	Freon et al. (1996)	Diel variability
1963	Cullen et al. (1965)	Average separation between fish
1977	Graves (1968)	Average separation between fish
1996	Scalabrin et al. (1996)	Dimension of sardines schools
1997	Scalabrin (1997)	Dimension of sardines schools
1995	Misund et al. (1995)	Shape of a school

The third column in this Table indicates only the topics specifically referred to by Diachok in his analysis, and the entries do not necessarily represent the entire subject matter of the corresponding article cited in the second column.

Prior to the start of the Modal Lion experiment, fish sampling was performed in the study area, to estimate the size distribution of the fish. The effective modal value was adjusted according to the growth rate of the fish, resulting in a final estimate of 16.5 cm for sardines. Also, the effective radius at the surface (i.e., the radius of a sphere having the same volume as the swim bladder) was determined, being $a_0 = 0.79$ cm for sardines.

The depth at which fish ensembles are located, whether dispersed or grouped more closely together in schools, is a basic input parameter of the school scattering model. Before, during, and after the Modal Lion experiment, echo sounding measurements were performed to determine the depth distribution of fish in the study area. It was found that the modal depth of schools, representing only large schools, was 65 m during the day or night. With subsequent adjustments to his transmission loss model, Diachok (1999) determined that the average depth is 65 m during the day, and 60 m at night. Furthermore, an

average depth for dispersed fish of 25 m was measured, consistent with previous reports by Culley (1971) and Barange et al. (1996) indicating that dispersed sardines are usually located between 15 m and 35 m depth (see Table 1).

Regarding the number of fish, and the shape and internal structure of the school, there is little that could be inferred directly from the echo sounder measurements or sampling. In response to predators, the fish group themselves together in schools. These schools consist of fish of the same species, of similar size, closely spaced, and similarly oriented. Shoals are defined as structures where fish are more widely spaced, and loosely organized and orientated, coexisting at the same depth with schools.(Pitcher et al.,1985;Pitcher & Parrish,1993) During the day, between 60% and 70% of the fish form schools near the bottom in layers. In the evening fish migrate upwards nearer to the surface and form shoals. At night only 5% of the fish form schools. The remainder are either well dispersed (20%) or in "accumulations" (75%), which contain dispersed fish, as well as schools.(Azzali et al.,1985) It has been observed that the volume of sardine schools at night is 0.6 times the volume during the day,(Freon et al.,1996) which implies that a smaller number of individuals form schools at night.

With respect to the average distance between nearest neighbors, a controlled experiment in a large pool during daytime showed that the average distance between neighboring fish in a school of sardines is $s = 0.6L$, where L is the average length of the fish in the school.(Cullen et al.,1965) However, at-sea measurements by Misund (1991), using high-resolution sonar, and by Graves (1968), using photography, have reported values of s equal to approximately L and $0.8L$, respectively.

Dimensions of adult sardine schools were measured by Scalabrin et al. (1996) and Scalabrin (1997), finding a modal value of 6 m by 2 m, although, on average, they are larger. With respect to the shape of the school, a first approximation is to model it as an oblate spheroid.(Misund et al.,1995) Considering the indicated size of 6 m by 2 m, the effective radius of a sphere of equivalent volume would be about 2.08 m. The number

of fish contained in a school with these characteristics, assuming an average separation between neighboring fish of $s = L = 16.5$ cm, is about 8,000 individuals.

2.2.2. The Diachok analysis

To process the data, and obtain estimates of the species and abundance of the fish giving rise to the absorption effects in his experiment, Diachok used the resonance frequencies for fish schools derived from the published back scattering work of Feuillade et al. (1996), and some unpublished computations by Nero. He then proposed the following semi-empirical equation to describe the variation of the resonance frequency of a school:

$$f_0'/f_0 \approx x_S[1 + (12N^{2/3}\beta^{1/3}/\pi^2)]^{-1/2}[1 + 5.8(s/\lambda_0 - 0.06)] \,, \qquad (2.11)$$

where f_0' is the resonance frequency of a school of N fish at a separation s between nearest neighbors, f_0 is the theoretical resonance frequency of an individual fish in the school (i.e., without interacting with the other fish), and λ_0 is the associated acoustic wavelength.

The factor x_S in Eq. (2.11) is a correction for the nonsphericity of the oblate spheroidal shape of the school, which is assumed to increase the resonance frequency of the school. The magnitude of this factor was assumed to be that proposed by Weston (1977) [see Eq. (1.7)] for the nonsphericity of an individual air-filled swim bladder. With regard to this assumption, it should be noted, as was shown using the school scattering model in Figure 2.9, that the apparent resonance frequency of a school could increase or decrease depending on the orientation of the oblate spheroidal school with respect to the incident field.

Equation (2.11) was inferred by plotting the ratio f_0'/f_0 of the shifted resonance frequency f_0' to the individual resonance frequency f_0, as indicated by the results of Feuillade et al. (1996) and the unpublished work of Nero, as a function of the separation s between fish, scaled in units of the resonance wavelength λ_0 (i.e. s/λ_0). The computations shown in Figure 10 of Feuillade *et al.*, used by Diachok to derive Eq. (2.11), were performed with the assumption that the fish were physoclists, and that the swim bladders did not compress

with increasing depth. However, Diachok subsequently applied Eq. (2.11) to analyze transmission data from sardines, which are physostomes. As a check, the present authors have recomputed the cases considered in Figure 10 of Feuillade *et al.* for schools of 123 fish, but assuming the fish are physostomes, and therefore allowing the swim bladders to compress with depth. The subsequent results of plotting f_0'/f_0 against s/λ_0 fall along the curve for 123 fish shown in Figure 3(b) of Diachok's paper, in agreement with his assumption that Eq. (2.11) should be valid for describing the variation of f_0'/f_0 with s/λ_0, as a function of water depth, for physostomes. The results described in the present work indicate that the approach described in Diachok's paper, which uses Eq. (2.11) to infer school size from the observed shift in resonance frequency, and which is based upon models of back scattering from schools of fish, can lead to a marked underestimation of fish abundance.

As stated above, Diachok estimated the absorption coefficient α_b as a function of frequency by matching experimental measurements and computational models of transmission loss. Figure 2.11 shows some of these results. By knowing the theoretical value of the resonance frequency for an individual fish, and using the peak frequencies of the absorption lines found in his experiment (shown in Figure 2.11), Diachok was able to calculate the ratio f_0'/f_0 for the different measurements.

As an example of this approach, during the day [see Figure 2.11(c)], f_0'/f_0 was measured to be about 0.6. To match the observed data, Equation (2.11) allows different combinations of N and s to achieve this value of f_0'/f_0, assuming that the radius of the swim bladder and the depth are known. Initially, Diachok proposed two combinations of N and s, i.e, ($N = 10,000$, $s = L$) and ($N = 5,000$, $s = 0.8L$), which both satisfy the required value of $f_0'/f_0 = 0.6$ for a school of sardines in the daytime. Since these combinations indicate a marked difference (i.e., a factor of 2) in the number of fish in the school, Diachok used the diel variability and modal values of s reported in the literature (refer to Table 2.1) to improve the estimate. The relations $N_{night} = 0.6N_{day}$, $s_{night} = 0.8s_{day}$ were subsequently used to incorporate the diel variability. The peak frequencies of the absorption

lines found for α_b, for the four primary cases, and two secondary cases, shown in Figure 2.11, and also the interpretations proposed by Diachok in terms of number and spacing of sardines within the school, are summarized in Table 2.2.

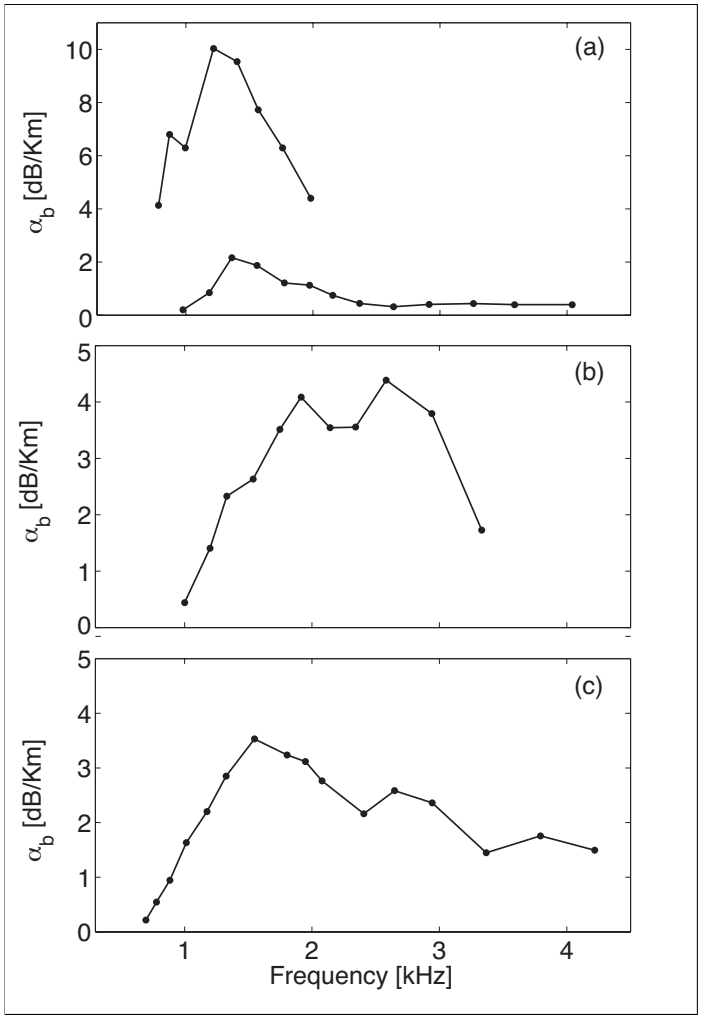

FIGURE 2.11. Absorption coefficients of layers of sardines as a function of frequency and depth. Data taken from Diachok (cf. figure 17 of Diachok (1999)). Data points denoted by •. (a) Night. (b) Sunrise. (c) Day.

2.2.3. Reinterpretation of the data

2.2.3.1. Inputs to school scattering model

Using the school scattering model described in Section 1.2.3, simulations were performed to determine the variation of the extinction cross section for schools of sardines of

individual length L = 16.5 cm, with an effective swim bladder radius, at the surface, of 0.79 cm. A random variation of the swim bladder radius within the school was introduced, allowing a standard deviation $\sigma = \pm$ 10% of the mean value of the radius.(Feuillade et al.,1996)

Since the swim bladder is elongated, and the resonance frequency of an elongated swim bladder (as with a bubble) is greater than that of a sphere of equal volume, it is necessary to incorporate a resonance frequency correction factor derived from Weston's equation (Weston,1977) [see Eq. (1.7)]. Following Diachok, it is assumed that the sardine swim bladder can be represented using a prolate spheroidal model, and a frequency correction factor of 1.28 is used for 16.5 cm long sardines.

The viscosity of fish flesh for sardines can be inferred from data concerning the quality factor Q of a fish given by Love (1977) for three types of physotomes at different depths. According to Love, the damping factor H (which is equal to Q at the resonance frequency) can be calculated using Equations (1.4) and (1.5). Using these equations, the average value found for the viscosity of fish flesh $\xi = 20.8\ Pa \cdot s$. In Diachok's analysis the data of Andreeva (1964) were used, from which were extracted: $Q_0 = 4.1$ at 6 m depth, $Q_0 = 5$ at 20 m depth, and $Q_0 = 7$ at 65 m depth. The corresponding viscosity was calculated to be $\xi = 20\ Pa \cdot s$. Since there is little difference between these estimates of the fish flesh viscosity, and since the Love swim bladder model is used here, a viscosity value of $\xi = 20.8\ Pa \cdot s$ was used in the calculations described in the present work.

Following Diachok, the extinction cross section was computed using an oblate spheroidal form for the schools of sardines, assuming, in every case, an aspect ratio 1/3, but with variable dimensions and numbers of fish contained. Each school was also assumed to be ensonified along a direction which is perpendicular to the axis of rotational symmetry of the oblate spheroid [i.e., as depicted in Figure 2.8(b)].

The 3-D locations of the sardines within the schools were constructed using a random number generator to determine the x, y, and z coordinates. The locations of the fish were constrained to lie within the boundary of the oblate spheroid specified for each case. To

obtain the required nearest-neighbor separation distance s between the fish, a condition was introduced to constrain the minimum distance between each fish and its nearest neighbors to lie within the range $s \pm 0.1s$. However, it was found, when performing a forward scattering analysis using the school scattering model, that the results are practically insensitive to the specific type of packing algorithm adopted, as long as the same overall fish density within the school is maintained. The reason for this is the almost complete absence, in the forward scattering case, of interference effects between the scattered fields from the individual fish, as discussed above in Section 2.1.2. This is illustrated in Figure 2.10. Curve 2 represents the frequency variation of the extinction coefficient of the sardine school when the fish locations in the school are generated using the packing algorithm just described. Curve 3 is the equivalent curve, for the same density of fish, when the sardines are located using a "body-centered cubic" type algorithm (i.e., visualizing the schools as constructed of cubic cells, each with a fish at each corner of the cube, and with one in the center, and also allowing random variations in the x, y, and z coordinates for each fish).(Feuillade et al.,1996) Curves 2 and 3 are almost exactly coincident, showing that the predicted frequency variations of the extinction coefficient for the two packing methods are practically identical.

2.2.3.2. Variation of school resonance peak frequency with fish spacing

To use the school model to estimate the number of sardines in a school, it is necessary to first develop curves predicting the variation of f_0'/f_0 as a function of the nearest-neighbor spacing s. This was also performed by Diachok (see Figure 3b of Diachok (1999)). However, in the present case, the curves are developed using a forward scattering paradigm. To achieve this, the extinction cross section was calculated for schools of 3,000, 5,000, 7,000 and 10,000 sardines, with average nearest-neighbor separations s= $4L$, $2L$, L, and $0.8L$.

As an example, Figure 2.12 shows the calculation of the average extinction cross section for a school containing 3,000 sardines, at 60 m depth, for four different values of the nearest-neighbor separation s, using 10 randomizations for each separation. It may be

clearly seen how the frequency of the peak value of the extinction cross section progressively moves to a lower frequency as the value of s is decreased.

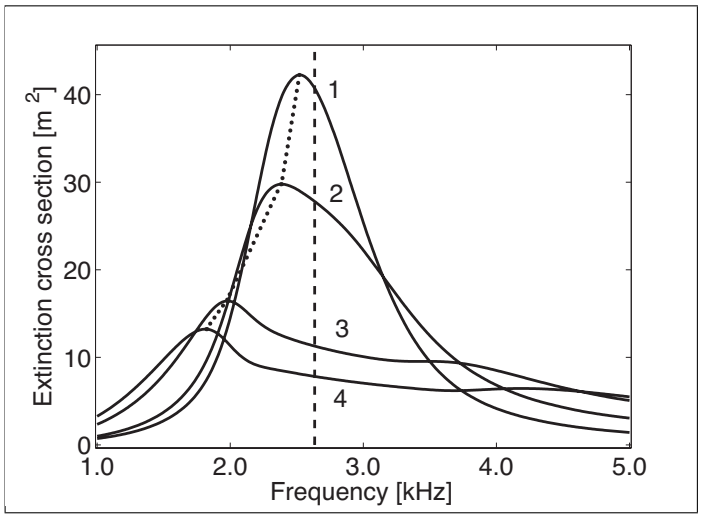

FIGURE 2.12. Average extinction cross section for a school of 3,000 fish at different separation between nearest neighbors. The vertical line indicates the theoretical resonance frequency for an individual fish. (1) $s = 4L$, (2) $s = 2L$, (3) $s = L$, (4) $s = 0.8L$. The dotted line indicates the downward shift of the peak frequency as the fish separation is decreased.

Figure 2.13 shows the variation of f_0'/f_0 as a function of s (scaled in units of L), for schools located at 25 m, 60 m and 65 m depth. The ratio f_0'/f_0 was calculated using the peak frequency f_0' of the extinction cross section in each case, and the theoretical resonance frequency f_0 of an individual sardine placed at the same depth as the school. For example, the curve demarcated by the "□" points in Figure 2.13(b) was produced by locating and plotting the four peak frequencies for the four curves in Figure 2.12.

2.2.3.3. The primary peaks

The two primary peaks shown in Figure 2.11 are considered first, which are due to absorption by fish schools, i.e., the peak shown in Figure 2.11(c) at 1.7 kHz, which is derived from data recorded in daylight, and also the lower absorption peak shown in Figure 2.11(a) at 1.5 kHz, which is derived from data recorded at night. The other two primary peaks in Figure 2.11, i.e., the peak seen at 2.7 kHz in Figure 2.11(b), and the upper peak seen at 1.3

kHz in Figure 2.11(a), which are both attributed to absorption by dispersed sardines, rather than schools of sardines (see Table 2.2), are not considered here.

TABLE 2.2. Measured resonance frequencies of sardines, and number of fish in a school

Measured f_0'	Time of day	Depth	Due to	Theoretical value
1.3 ± 0.1 kHz	Night	25 m	Dispersed sardines	$f_0 = 1.5 \pm 0.3$ kHz
2.7 ± 0.3 kHz	Day/Sunrise	65 m	Dispersed sardines	$f_0 = 2.8 \pm 0.6$ kHz
1.5 ± 0.1 kHz	Night	60 m	School of sardines	Consistent with $N = 3,000, s = 0.6L$
1.7 ± 0.1 kHz	Day	65 m	School of sardines	Consistent with $N = 5,000, s = 0.8L$
0.9 ± 0.1 kHz	Night	25 m	School of sardines	Consistent with $N = 10,000, s = 2L$
2.0 ± 0.2 kHz	Sunrise	65 m	School of sardines	Consistent with $N = 10,000, s = 1.5L$

Resonance frequencies of the absorption peaks shown in Figure 2.11, and the corresponding interpretation proposed by Diachok for the number of fish N in the school and the nearest-neighbor spacing s. The bottom two rows are for the two smaller secondary peaks detected. The upper two entries in the right-most column are for dispersed fish, and show the predicted resonance frequency for individual sardines at the indicated depth (compare with measured resonance frequency in corresponding left-most column).

In Diachok's analysis (see Table 2.2), it is proposed that the peak seen at 1.7 kHz is due to a school of 5,000 sardines, at 65 m depth, with a nearest neighbor-spacing of $s = 0.8L$. The value of f_0'/f_0 indicated by data is 0.6. According to the present analysis, assuming a separation $s = 0.8L$, it requires approximately 7,000 fish [see Figure 2.13(c)] to achieve the ratio $f_0'/f_0 = 0.6$, i.e., about 40% more than indicated by the previous analysis. Further computations using the school scattering model showed that it was possible to achieve $f_0'/f_0 = 0.6$ with a school of 5,000 sardines, but the nearest-neighbor spacing would have to be reduced to $s = 0.67L$, which is greater than the $s = 0.6L$ value measured by Cullen et al. (1965) during a controlled pool experiment, but less than the $s = 0.8L$ value used by Diachok, based on at-sea measurements.(Misund,1991;Graves,1968) If a value $s = 0.89L$ is used in the school scattering model (i.e., about in the center of the $s = 0.8L$ to $s = L$ range indicated by the experiments of Misund (1991) and Graves (1968)) then a much larger number of sardines is needed to achieve $f_0'/f_0 = 0.6$, i.e., about $N = 10,000$ (see right-most column of Table 2.3).

TABLE 2.3. Comparison of the two analyses

Measured f_0'	Depth	f_0'/f_0	s	Diachok	Present	Alternatives
1.5 ± 0.1 kHz	60 m	0.57	$0.6L$	$N = 3000$	$N = 5000$	$N = 7000, s = 0.8L$ $N = 3000, s = 0.5L$
1.7 ± 0.1 kHz	65 m	0.6	$0.8L$	$N = 5000$	$N = 7000$	$N = 10000, s = 0.89L$ $N = 5000, s = 0.67L$
0.9 ± 0.1 kHz	25 m	0.69	$2L$	$N = 10000$	$N = 300000$	$N = 10000, s = 1.5L, f_0'/f_0 = 0.61$
2.0 ± 0.2 kHz	65 m	0.72	$1.5L$	$N = 10000$	$N = 30000$	

A direct comparison is made between the data interpretations described by Diachok,(Diachok,1999) and the present analysis. The right-most column indicates several other combinations of N and s which could be used to fit the data.

Also in Diachok's analysis (Table 2.2), it is proposed that the peak seen at 1.5 kHz is due to a school of 3,000 sardines, at 60 m depth, with a nearest neighbor-spacing of $s = 0.6L$. The value of f_0'/f_0 indicated by the data is 0.57. According to the present analysis, assuming a separation $s = 0.6L$, it requires about 5,000 fish [see Figure 2.13(b)] to achieve the ratio $f_0'/f_0 = 0.57$, i.e., about 65% more than indicated by the previous analysis. To achieve $f_0'/f_0 = 0.6$ with the school scattering model using 5,000 sardines requires a nearest-neighbor spacing of $s = 0.5L$, which is smaller than the value obtained by Cullen et al. (1965) under controlled conditions. If a value $s = 0.8L$ is assumed, then a school of 7,000 sardines is needed to achieve $f_0'/f_0 = 0.6$ (see right-most column of Table 2.3).

This reanalysis of the primary peaks obtained during the Modal Lion experiment indicates that the present forward scattering analysis leads to significantly higher estimates of N than Equ ation (2.11), for the same values of f_0'/f_0 and s, and for schools of sardines both in daytime (65 m depth) and at night (60 m depth).

2.2.3.4. The secondary peaks

Table 2.2 also indicates two secondary peaks (and their corresponding interpretations in Diachok's analysis) seen in the measured absorption data (Figure 2.11). The peak at 2 kHz (i.e., the small peak seen to the left of the main peak in Figure 2.11(b)), derived from data taken at sunrise, is attributed to schools of 10,000 sardines, with nearest-neighbor

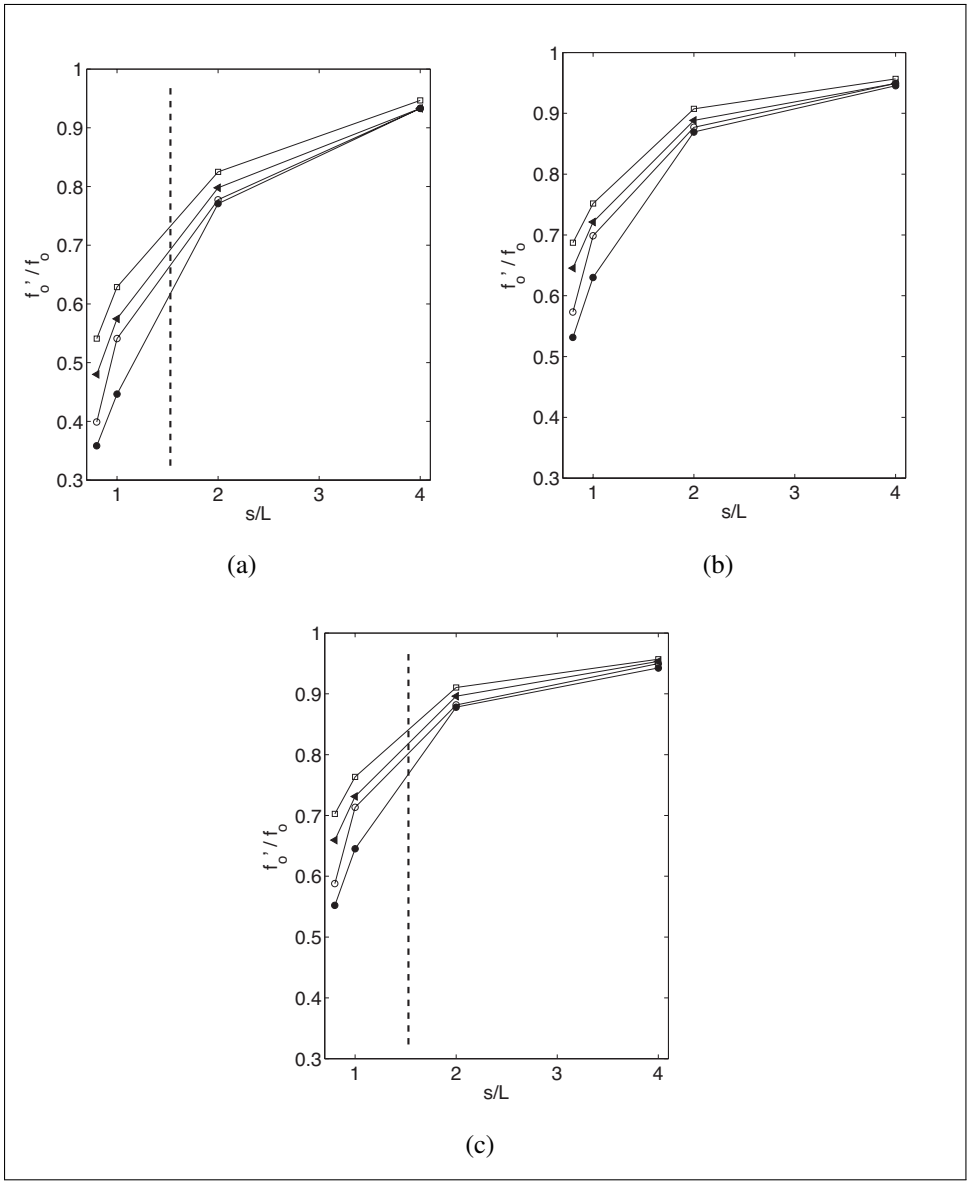

FIGURE 2.13. Calculations of f_0'/f_0 vs s/λ_0, based on extinction cross section simulations for $s = 4L, 2L, L, 08L$, as shown in Fig 2.12. (a) at 25 m depth, (b) 60 m depth, (c) 65 m depth. In all three cases, simulations were made for schools containing 3,000 (□), 5,000 (▲), 7,000 (○) and 10,000 (●) fish. The vertical dashed lines in (a) and (c) denote the abscissa $s/L = 1.5$. The points at which these lines intersect the four curves for different N are used to estimate values for f_0'/f_0 when $s/L = 1.5$, and are subsequently used to plot the dashed lines in Figure 2.14.

spacing $s = 1.5L$, at 65 m depth. The peak at 0.9 kHz (i.e., the small peak seen to the left

of the main peak in the upper curve in Figure 2.11(a)), which is derived from data recorded at night, is also attributed to schools of 10,000 sardines, with $s = 2L$, at 25m depth.

Initial computations, using the school scattering model to analyze the data from these two secondary peaks, indicated that the number of sardines in the schools was probably significantly larger than the 10,000 individuals proposed by Diachok. Rather than pursuing this investigation directly using the scattering model, which would have involved multiple computational inversions of huge matrices as indicated by the matrix equation $\mathbf{v} = \mathbf{M}^{-1}\mathbf{p}$ in Section 1.2.3 [see Eqs. (1.13) and following discussion], a second, indirect, approach was used.

During the course of his analysis, Diachok makes use of the first order approximation, described by Carey and Roy (1993) and Lu et al. (1990), for the fundamental mode of a spherical bubble cloud, i.e.,

$$f_0'/f_0 \approx N^{-1/3}\ \beta^{-1/6}\,, \tag{2.12}$$

where N is the number of bubbles in the cloud, and β is the gas volume fraction. To determine whether a relationship comparable to Equ ation (2.12) applies to the variation of the collective resonance frequency of the oblate spheroidal schools of swim bladder fish modeled in this work, the cases computed to determine the data points shown in Figs. 2.13(a) and 2.13(c) are replotted, using a different format to display the variation of f_0'/f_0 as a function of $N^{-1/3}$, as shown in Figures 2.14(a) and 2.14(b). Both of these figures contain three lines. The lower and upper lines represent the variation of f_0'/f_0 with $N^{-1/3}$ for constant values of $s = L$, and $s = 2L$, respectively. Each line is determined by calculating a least-squares fit to the four data points, for the specified value of s/L, extracted from the four curves for N = 3,000, 5,000, 7,000, and 10,000, shown in Figs. 2.13(a) and 2.13(c). The third (dashed) line, in each of Figs. 2.14(a) and 2.14(b), is a least-squares fit to data points also derived from the four curves in Figs. 2.13(a) and 2.13(c), but this time for $s = 1.5L$. The values of f_0'/f_0 in this case are determined by interpolating these curves at $s/L = 1.5$. In both Figs. 2.13(a) and 2.13(c), a vertical dashed line (s/L=1.5) is

drawn. The values of f_0'/f_0 used are those indicated where this vertical line intersects the four curves for different N.

In all of the lines plotted in Figs. 2.14(a) and 2.14(b), the least-squares fit of the points to a straight line (and the clear rectilinear trend of the points themselves) provides a convincing demonstration that the downward shift of the collective resonance of the fish schools, as the number of fish increases, is governed by the relation $f_0'/f_0 \propto N^{-1/3}$, just as previously proposed for the fundamental mode of a spherical bubble cloud.(Carey & Roy,1993;Lu et al.,1990) This relationship provides a very useful tool for extending the technique of estimating fish school size, by measuring the downward shift of the collective resonance frequency of the school, to much greater numbers of fish, and can now be applied to perform a reanalysis of the two secondary absorption lines detected in the Modal Lion data.

The secondary peak at 2 kHz in Figure 2.11(b), derived from data taken at sunrise, is attributed by Diachok to schools of 10,000 sardines, with nearest-neighbor spacing $s = 1.5L$, at 65 m depth. The measured value of $f_0'/f_0 = 0.72$. Assuming the same value of s, and the same 65 m depth of the school in the water column, the dashed curve in Figure 2.14(b) indicates that a value of $f_0'/f_0 = 0.72$ is obtained for a school of $N \approx$ 30,000 sardines.

The secondary peak at 0.9 kHz in Figure 2.11(a), derived from data taken at night, is attributed by Diachok to schools of 10,000 sardines, with nearest-neighbor spacing $s = 2L$, at 25 m depth. The measured value of f_0'/f_0 indicated by Diachok is 0.69. However, he calculates this value assuming that f_0=1.3 kHz, which is the resonance frequency observed from other absorption measurements due to sardines in a dispersed layer at 20 m. If these values of f_0'/f_0, s are assumed, and a depth 25 m used, then the dashed curve in Figure 2.14(a) indicates that a value of $f_0'/f_0 = 0.69$ is obtained for a school of $N \approx$ 300,000 sardines. If, on the other hand, the value of f_0 is calculated for an individual sardine at 25 m, using the present model, a value close to 1.5 kHz (within the range given by Diachok,

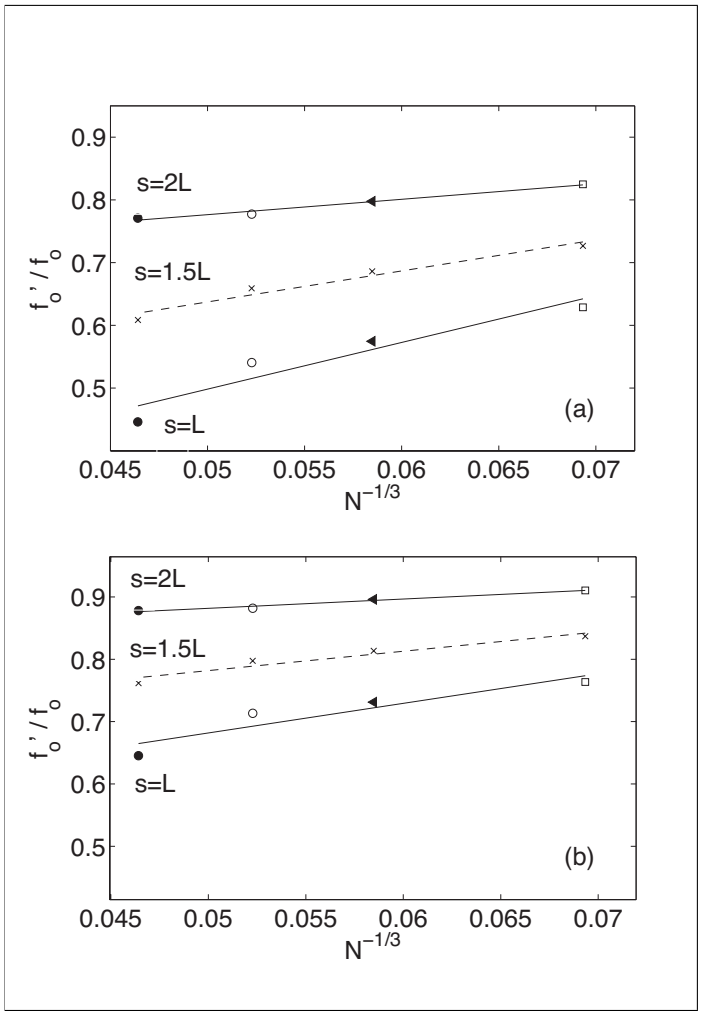

FIGURE 2.14. Variation of f_0'/f_0 vs $N^{-1/3}$, where N is the number of fish in the school. The data indicated by (□), (▲), (○), (●) are extracted from the curves shown in Figures 2.13(a) and 2.13(c). The points marked (×) were obtained by interpolating the curves shown in Figures 2.13(a) and 2.13(c) at a value $s/L = 1.5$. The straight lines are fitted to the points, in each case, using a least-squares method. (a) 25m depth, (b) 65m depth.

noted in Table 2.2) is obtained, and a value of $f_0'/f_0 = 0.61$. However, if $s = 2L$, inspection of the dashed line in Figure 2.14(a) indicates that $f_0'/f_0 = 0.61$ is not achievable for this nearest-neighbor spacing. Alternatively, if it is assumed that $s = 1.5L$, as for the previously considered 65 m depth schools represented by the 2 kHz peak in Figure 2.11(b), then Figure 2.14(a) indicates that a value of $f_0'/f_0 = 0.61$ is obtained for a school of $N \approx$ 10,000 sardines, which is the same as Diachok's estimates, but for a significantly more

closely spaced school than he estimated. If $1.5 \leq s < 2$, then the calculated value of $N \geq$ 10,000 sardines in the school, as seen in the previous 65 m school case.

3. RESONANCE SCATTERING BY FISH SCHOOLS: EVALUATION OF THE EFFECTIVE MEDIUM METHOD

The purpose of the present chapter is to evaluate the effective medium method as a tool for analyzing low frequency scattering from schools of swim bladder fish, through a theoretical comparison with the coupled differential equation formalism of Feuillade et al. (1996) and also by comparison with experimental data. Both theoretical approaches are compared with the Modal Lion sound absorption data of Diachok (1999), and experimental target strength data reported by Holliday (1972).

3.1. Implementation of the effective medium method

In this work, when EM is used to calculate scattering from fish schools, the effective wave number k_e is determined from Eq. (1.9), incorporating a scattering amplitude f_b for an individual fish, as defined by Eq. (1.6), and with damping factors for fish prescribed by the Love model, (Love,1978) as defined by Eq. (1.5).

Scattering computations for schools of fish, using EM, are presented here for ensembles which are either: (1) spherical in form; or, (2) oblate spheroidal in form. The spherical cases are implemented using Anderson's fluid sphere theory. (Anderson,1950) Hahn (2007) has already described the application of Anderson's theory to this problem, and rather than providing another detailed account here, the reader is referred to section 2C of Hahn's paper for further details. In particular, his Eq.(26) defines a scattering amplitude $f_A(k, \theta)$ for a fish school (there is no ϕ dependence, because of the spherical symmetry), obtained using the Anderson theory, describing the frequency and azimuthal variations of the scattered field for a spherical school, with the school represented as an effective medium.

The calculations presented here for oblate spheroidal cases are performed using the Extended Boundary Condition (EBC) method, sometimes called the "T-matrix" method. Again, rather than provide a detailed account of this theory, we refer the reader to the original article by Waterman (1969), or to a recent application of this method to describe acoustical scattering from prolate spheroidal air bubbles. (Feuillade,2012) As with the Anderson

theory, the EBC method leads to a definition of a scattering amplitude, i.e., $f_E(k, \theta, \phi)$ (ϕ now appears, because the spherical symmetry is, in general, lifted), to describe the frequency and angular variations of the scattered field.

3.2. Implementation of the coupled differential equation method

To implement CDE, schools are simulated by grouping together individual fish in a way that simply approximates the formations which fish typically adopt when swimming closely together.

First, the overall shape and size of the school is determined. Since one main aim of this work is to investigate EM by comparing it against CDE for equivalent cases (the second purpose is comparison of EM with experimental data), the shape and size of the school is the same as for the corresponding EM school. Therefore, the cases consist of spherical and oblate spheroidal schools of given dimensions.

Second, the fish are positioned within the school with a packing density parameterized by the mean nearest neighbor distance s between any two fish in the school. As the fish swim, the actual distance between nearest neighbors varies from s. The school is therefore constructed by placing the fish at randomized locations, such that the mean distance between neighboring fish is s, but a small variation in this distance is allowed, using a normally distributed randomizing algorithm with a standard deviation of $\pm\, 10\%$ of s.

Third, the fish locations, and directions in which they are swimming, frequently change. We account for these variations in location by averaging the scattering over a series of "snapshot" realizations. In each snapshot, a completely new random configuration of the fish is generated, using the procedure just outlined. For spherical schools, the azimuthal angle of ensonification is also varied randomly between 0 and 2π for each snapshot, to average over changes of direction of incidence.

Once the school is generated, the scattered pressure, in any direction, is computed using the theory outlined in Section 1.2.3 and, in particular, by evaluating the coherent sum represented by Eq. (1.14).

3.3. Theoretical investigations

3.3.1. A small spherical school

Hahn (2007) performed a detailed theoretical study of scattering from idealized, spherically shaped schools of swim bladder fish, using EM. To calibrate the EM model, Hahn computed the scattering for a small spherical school of 66 fish of 20 cm length, at a density of about 300 fish/m^3, with all the fish at 2 m depth. He compared EM against a numerical benchmark calculation involving a Foldy self-consistent expansion of the multiple scattered field between the fish, and a subsequent solution by Gaussian elimination of the resulting set of $N = 66$ coupled equations. The fish were assumed to be identical monopole scatterers, each with the same scattering amplitude. The data inputs used by Hahn are summarized in Table 3.1. He found that the frequency variation of the total scattering cross-section shows virtually no deviation between EM and the numerical benchmark over a frequency range of about 100-1500 Hz, which includes the dominant monopole resonance of the bladder.

Figure 3.1(a) is a recalculation of the frequency variation of the total scattering cross section for the 66 fish case considered by Hahn (*cf.* Fig. 4 of his paper). The two curves in Fig. 3.1(a) show: (1) EM, using Eq. (1.9) to represent propagation inside the school, where the scattering amplitude f_b for a single fish is defined by Eq. (1.6), and δ_B is given by Eq. (1.3), with Q replaced by H as specified in the Love swim bladder model [see Eqs. (1.4) and (1.5)]; and (2), CDE as outlined in Section 1.2.3, with f_b the same as for EM. The parameters used are those of Table 3.1. Figure 3.1(b) shows the corresponding variation of $|4\pi n \mathrm{f}_b^2/k|$ for this case. In these figures, the frequency variation is calculated up to 5 kHz. Since the total scattering cross section is being considered, the upper frequency limit on the use of EM (i.e., f_u) is not an issue.

The EM curve in Fig. 3.1(a) was calculated via Anderson's theory, (Anderson,1950) using an expression equivalent to Eq. (29) in Hahn's paper. The total scattering cross

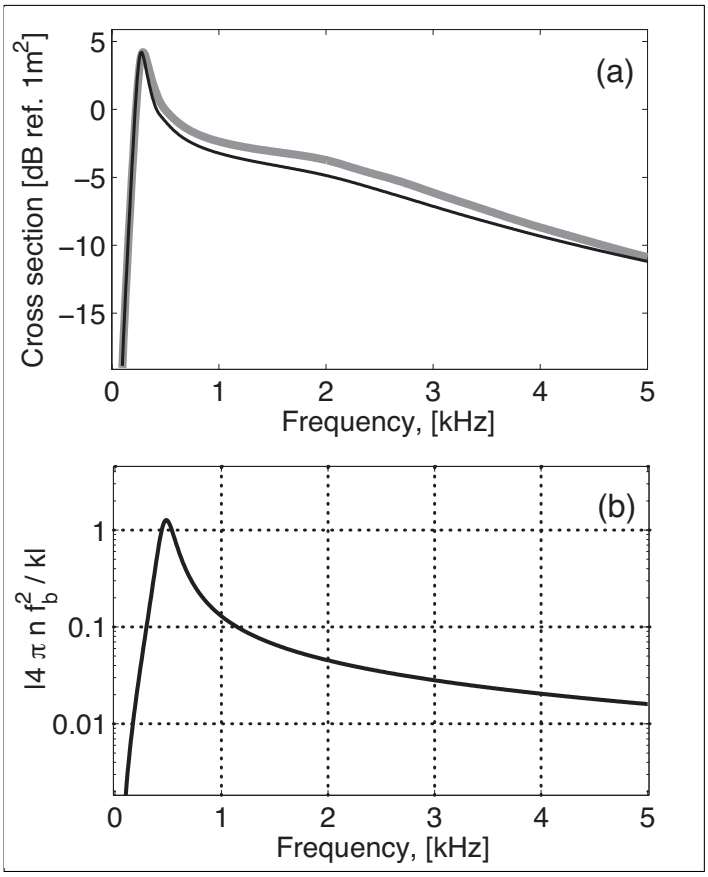

FIGURE 3.1. Total scattering cross section for a small spherical school of 66 fish at 2 m depth. (a) Black line: EM model calculations using an expression equivalent to Eq. (29) in the paper of Hahn (2007). Gray line: CDE model. Figure 4(a) of Hahn's paper shows a practically identical result for EM prediction until 2 kHz. (b) Variation of $|4\pi n f_b^2/k|$ for this case.

TABLE 3.1. Input parameters for Fig. 3.1

Parameter	Symbol	Value
Length of the fish	L	0.2 m
Surface radius of swimbladder	a_0	0.01 m [a]
Viscosity	μ	50 $Pa \cdot s$
Depth of the school	z	2 m
Theoretical resonance frequency	f_0	475 Hz
Number of fish in the school	N	66
Fish density	n	300 fish/m^3 [b]

[a] Linear dependence of a_0 on L ($a_0 = 0.058L(cm) - 0.14$) was based on data summarized by Diachok. (Hahn,2007)

[b] Equivalent to an average nearest neighbour separation of $0.75L$

section predicted by CDE, however, was computed by a numerical integration of the differential cross section $\Delta\sigma_s$ over 4π solid angle, i.e., (Medwin & Clay,1998)

$$\sigma_s(f) = \int_0^{2\pi} d\phi \int_0^{\pi} \Delta\sigma_s(\theta, \phi, f)\, \sin\theta \, d\theta \,, \tag{3.1}$$

where ϕ and θ are the azimuthal and elevation angles, respectively. The CDE curve in Fig. 3.1(a) represents an average over ten numerical evaluations of Eq. (3.1), each evaluation corresponding to a different school randomization, as described in Section 3.2.

Figures 3.1(a) and 3.1(b) lead to two initial observations. First, the resonance frequency for an individual fish at 2 m, which is essentially equal to the peak frequency of $|4\pi n \mathrm{f}_b^2/k|$ seen in Fig. 3.1(b), is about 475 Hz. Second, the peak scattering frequency of the school, predicted by both EM and CDE in Fig. 3.1(a), is downshifted from the individual fish resonance frequency to about 280 Hz. The EM curve is downshifted slightly more than the CDE curve.

More detailed examination of Fig. 3.1(a) shows that, between about 280 Hz and 5 kHz, CDE indicates a slightly higher value for the total scattering cross-section than EM. The difference, which at its greatest point is only about 1.5 dB, would probably be practically insignificant as regards its effects on experimental measurements of scattering from fish schools at sea. Since EM does not incorporate multiple scattering between the fish, while CDE does, this implies that multiple scattering effects augment the total school scattering from the school over the resonance region, and lead to the higher levels predicted here by CDE. The fact that the difference is relatively minor, in this case, may be attributable to the small number (66) of fish considered. Close inspection of Fig. 3.1(b) shows that the value of $|4\pi n \mathrm{f}_b^2/k| > 0.01$ over most of the frequency range, from about 200 Hz to 5 kHz. If the increase in total scattering in this frequency range is indeed due to multiple scattering, this suggests that the condition $|4\pi n \mathrm{f}_b^2/k| \ll 1$ indicated by Frisch (Frisch,1970) can be made more precise. It implies that the condition $|4\pi n \mathrm{f}_b^2/k| < 0.01$ should apply for multiple scattering to be considered negligible, as is implicitly assumed in EM. This statement is reexamined below, as further cases are considered.

3.3.2. Scattering from large schools at variable depth

3.3.2.1. Background

While the differences in the total scattering cross section predicted by EM and CDE for the 66 fish school are small, questions remain about the general applicability of EM for the analysis of experimental data from fish schools in the sea.

The first issue concerns the size of schools and the number of fish they contain. For the 66 fish case, the inclusion of multiple scattering processes makes only a small difference to the total scattering. However, multiple scattering effects could potentially be much more significant if the number of fish involved is greater. For many species, fish schools may contain thousands of individuals, (Diachok,2000) and the effect of multiple scattering on total scattering level, in such cases, remains largely unexamined.

The second issue is water depth. The depth of water in which schools are located depends both upon the species of fish, (Culley,1971;Barange et al.,1996;Holliday,1972) and also the time of day. It is well known (Freon et al.,1996;Azzali et al.,1985;Woodhead,1966) that some species typically migrate to the top of the water column during the night, when the danger of predation is reduced, and that they disperse to feed. These fish then regroup into schools, and move to greater depth again, at sunrise. As the depth increases, or decreases, the swim bladder compresses, or expands, with changes in water pressure. This typically leads to significant changes in the resonance frequency of the swim bladder, and the corresponding scattering amplitude $|\mathrm{f}_b|$, of individual fish in the school.

The third issue is the method of measurement. Hahn's 66 fish school case, (Hahn,2007) discussed above, mainly considers the variation of the total scattering cross section of the school. However, in practice, the total scattering cross section is not usually measured in an ocean experiment. Acoustic scattering experiments on fish are primarily of two types: (a) by detection and measurement of the back scattered echo using an active sonar; (b) by measuring the attenuation of sound as it passes through a region of the ocean containing fish. Applied to fish schools, the first method leads to a measurement of the target strength (TS) of a school, which is directly related to the back scattering cross section σ_{bs} (N.B., *not*

the total scattering cross section) by: (Medwin & Clay,1998)

$$\mathrm{TS}(f) = 10\log_{10}\sigma_{bs}(f) = 20\log_{10}\left|\mathrm{f}_s(k,\pi,0)\right|, \quad [\mathrm{dB}] \tag{3.2}$$

where $\mathrm{f}_s(k,\pi,0)$ is the school scattering amplitude evaluated in the back scattering direction (counter to the incident field), and $f = \omega/2\pi = ck/2\pi$ is the ensonification frequency.

In contrast, measurements of the attenuation of sound by fish schools are related to the "extinction" cross section σ_e, which represents the total power loss from the incident wave due to scattering and internal absorption by fish in the school. According to the "extinction" theorem (Ishimaru,1997) (sometimes also called the "forward scattering" or "optical" theorem), this loss is directly related to the behavior of the forward scattered wave, i.e.,

$$\sigma_e(k) = \frac{4\pi}{k}\mathrm{Im}\{\mathrm{f}_s(k,0,0)\}, \tag{3.3}$$

where "Im" denotes the "imaginary part of" and $\mathrm{f}_s(k,0,0)$ is the school scattering amplitude evaluated in the forward scattering direction (the direction of the incident field). For CDE, f_s is defined by Eq. (1.16), while for EM it may be calculated using the field expansion of Anderson. (Anderson,1950)

The object of this work is the applicability of EM to back, and forward, scattering. An analysis is therefore performed comparing the behavior of EM with CDE, and with experimental data, for both measurement types.

Computations were performed to determine the variations of both σ_{bs} and σ_e, as functions of frequency, for spherical schools located at 2 m , 25 m, and 65 m depth. The schools each consisted of 1000 sardines of individual length $L = 16.5$ cm, with an effective swim bladder radius of 0.79 cm at the surface.(Diachok,1999) The average nearest neighbor spacing s between fish in the schools was equal to one fish length (i.e., 16.5 cm), which corresponds to a school density of 223 fish/m^3. For each depth, σ_{bs} and σ_e were calculated, using both EM and CDE. In every case, the CDE curve represents an average over ten numerical school evaluations, each evaluation corresponding to a different randomization of fish locations.

3.3.2.2. Theoretical comparison of the models: Back scattering

Figure 3.2(a) shows the frequency variation of the back scattering cross section σ_{bs} for a school located at 2 m depth. The overall agreement between EM and CDE is very good. The resonance frequency for an individual sardine at this depth is $f_0 = 0.6$ kHz [see Fig. 3.2(c)]. In Fig. 3.2(a), both EM and CDE predict that the resonance peak is downshifted in frequency, as seen before in Fig. 3.1(a). Another characteristic feature of back scattering from fish schools is also seen, i.e., the appearance of frequency dependent interference effects. (Feuillade et al.,1996;Raveau & Feuillade,2015) In this case, an interference trough causes the resonance peak to divide into two components. As this is a back scattering result, the upper frequency limit f_u applies. It is indicated in Fig. 3.2(a) by the vertical dashed line, i.e., $f_u = 2.273$ kHz. Since f_u is significantly higher than f_0, EM should be applicable in the resonance region.

Figure 3.2(c) shows the corresponding variation of $|4\pi n \mathrm{f}_b^2/k|$. Careful comparison of Figs. 3.2(a) and 3.2(c) reveals that about 50% of the school resonance features, which now all lie below $f_0 = 0.6$ kHz, fall in the frequency range $f < 300$ Hz, where $|4\pi n \mathrm{f}_b^2/k| < 0.01$. However, from 300 Hz to about 3700 Hz, $|4\pi n \mathrm{f}_b^2/k| > 0.01$. Inspection of Fig. 3.2(a) over the frequency range $300 - 3700$ Hz shows that, apart from the resonance peak region itself, where interference effects complicate the overall behavior, CDE predicts slightly higher values of σ_{bs} than EM, suggesting that multiple scattering has a small, but non-vanishing, effect on back scattering over this frequency range.

At 25 m depth the individual fish resonance frequency increases to $f_0 = 1.5$ kHz [see Fig. 3.3(c)]. Figure 3.3(a) shows that, while this approaches $f_u = 2.273$ kHz more closely, most of the resonance activity still lies well below f_u, so that EM should still be applicable. The agreement between EM and CDE is not as good as for the 2 m case. While there is still broad correspondence in the overall variation of σ_{bs} in the resonance region, some differences appear in the predicted peak amplitudes of the various features. Much of this is probably due to interference effects, which complicate the behavior in the resonance region. Figure 3.3(c) indicates that $|4\pi n \mathrm{f}_b^2/k| > 0.01$ between about 1 kHz and 3 kHz. Referring

back to Fig. 3.3(a) shows that, over most of this range, CDE predicts higher values of σ_{bs}, especially near $f_0 = 1.5$ kHz. However, it is difficult to distinguish definitively the effects due to multiple scattering from those due to interference.

At 65 m depth [Fig. 3.4(a)] the individual resonance frequency increases to $f_0 = 2.8$ kHz, which is higher than f_u. In the resonance region, therefore, the wavelength should be small enough to resolve the individual fish scatterers, thereby invalidating a primary assumption of the EM, and causing it to fail. While the overall variation of σ_{bs} is again complicated by interference effects, close inspection of Fig. 3.4(a) shows that, above f_u, large differences between EM and CDE do appear, especially around $f_0 = 2.8$ kHz. The maximum value of σ_{bs} indicated by EM in this region is about 3×10^{-3} m^2, while CDE predicts a peak value of about 10.3×10^{-3} m^2, which is more than 240% greater than EM. Also, above f_0, σ_{bs} falls off more rapidly for EM than for CDE. Coincidentally, in this case, Fig. 3.4(c) shows that $|4\pi n f_b^2/k| > 0.01$ between about 2.2 kHz and 3.9 kHz, implying that the greater divergence between EM and CDE might, in fact, be due to multiple scattering, rather than because the resonance region lies above f_u. However, when the corresponding forward scattering case, at 65 m depth, is examined below, it confirms that the large divergence in σ_{bs} is almost certainly because the resonance region lies above f_u.

3.3.2.3. Theoretical comparison of the models: Forward scattering

Figures 3.2(b), 3.3(b), and 3.4(b), show the variations of the extinction cross section σ_e with frequency, for schools at depths 2 m, 25 m, and 65 m, respectively. Since σ_e is directly related to the forward scattering amplitude, as described by Eq. (3.3), the applicability of EM is not generally limited at higher frequencies by the f_u condition, which does not apply here, and is not shown in these figures. For the same reason, far fewer, and less prominent, interference peaks and troughs appear in the variation of σ_e. In general, all three cases show good agreement between both models, although EM typically predicts a lower amplitude than CDE in the resonance region.

With the absence of strong interference peaks, it is much easier to assess the effect of multiple scattering on the overall level of school scattering. It has been suggested above

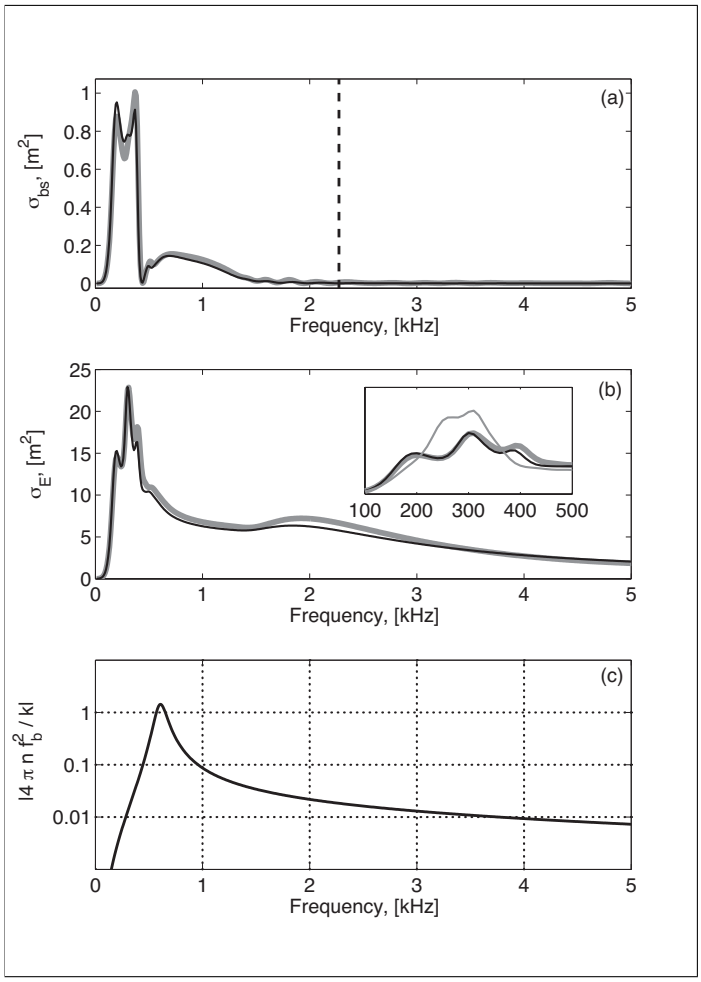

FIGURE 3.2. Scattering from a spherical school of 1000 fish at 2 m depth. The average separation between nearest neighbors s = L, where L is the fish length. (a) Back scattering cross section: black line – EM model; gray line – CDE model. The vertical dashed line denotes the frequency at which the wavelength is four times greater than s (i.e., $\lambda/s = 4$). (b) Extinction cross section: black line – EM model; gray line – CDE model. The inset box details the structure around the peak for the spherical school (black and gray lines), and a prolate spheroidal school (thin gray line). (c) Variation of $|4\pi n\mathrm{f}_b^2/k|$ for this case.

that the Frisch criterion (Frisch,1970) $|4\pi n\mathrm{f}_b^2/k| \ll 1$ should be replaced by the condition $|4\pi n\mathrm{f}_b^2/k| < 0.01$ to indicate where multiple scattering is negligible. When comparisons of Figs. 3.2(b), 3.3(b), and 3.4(b) are made with the variations of $|4\pi n\mathrm{f}_b^2/k|$ for these cases, i.e., Figs. 3.2(c), 3.3(c), and 3.4(c), respectively, it can be seen that the frequency range over

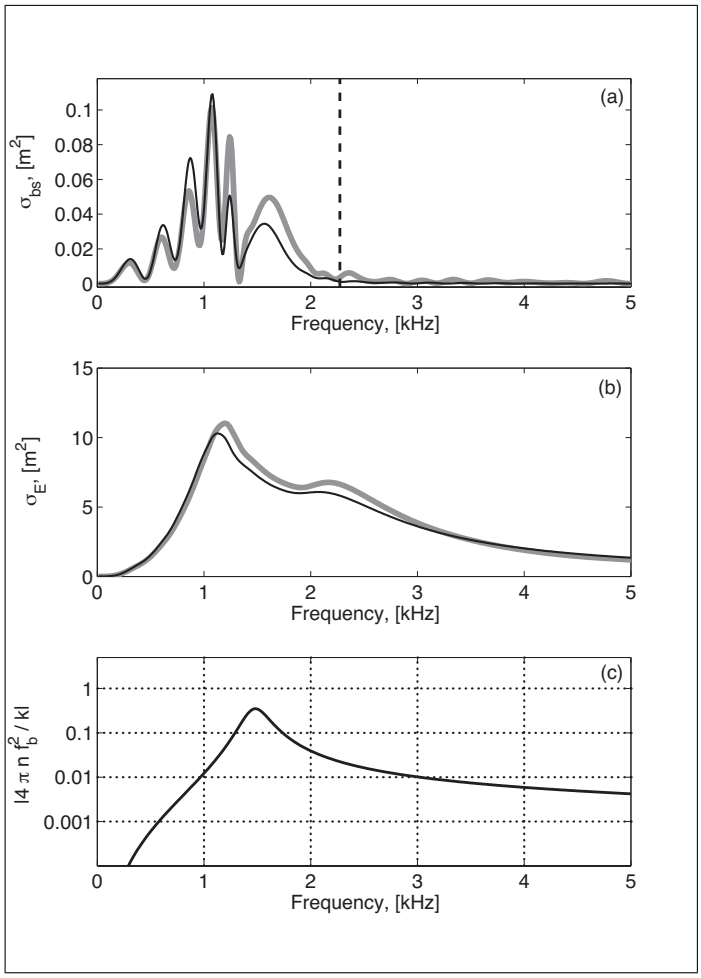

FIGURE 3.3. Scattering from a spherical school of 1000 fish at 25 m depth. The average separation between nearest neighbors $s = L$, where L is the fish length. (a) Back scattering cross section: black line – EM model; gray line – CDE model. The vertical dashed line denotes the frequency at which the wavelength is four times greater than s (i.e., $\lambda/s = 4$). (b) Extinction cross section: black line – EM model; gray line – CDE model. (c) Variation of $|4\pi n \mathrm{f}_b^2/k|$ for this case.

which the EM model predicts a lower value of σ_e than CDE almost exactly corresponds, in each case, with the frequency range for which $|4\pi n \mathrm{f}_b^2/k| > 0.01$.

Figures 3.3(b) and 3.4(b) show a two peak structure for the σ_e frequency variation, and that a "hole" appears in the resonance region. This phenomenon is due to interference effects among the fish, which change the resonance behavior of fish nearer to the receiver, as explained in Sections III.B and III.C of the paper of Raveau and Feuillade (2015). A

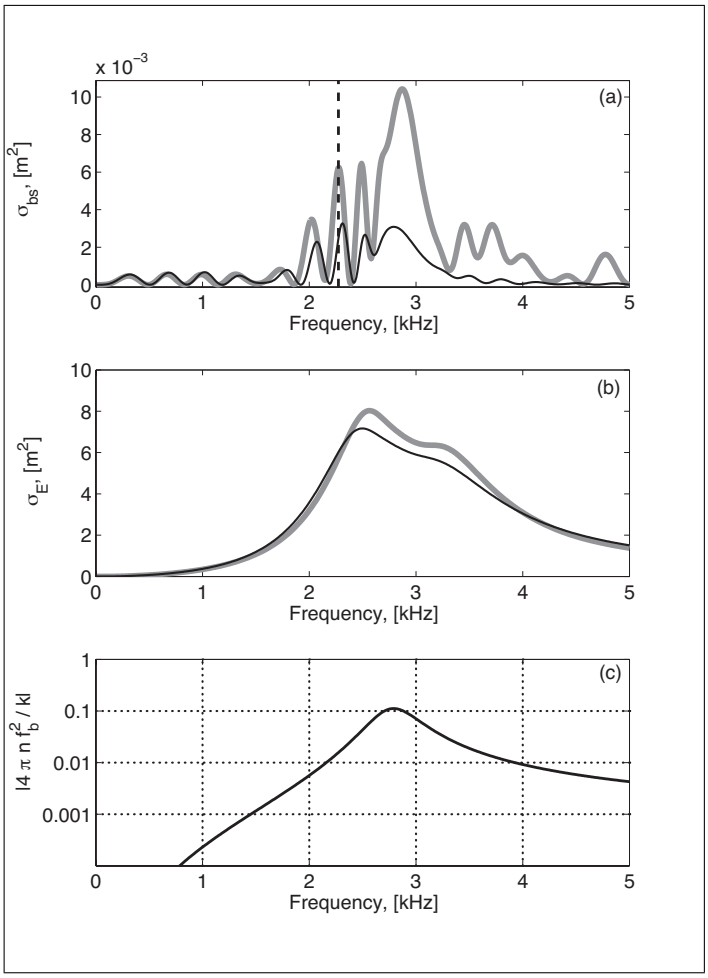

FIGURE 3.4. Scattering from a spherical school of 1000 fish at 65 m depth. The average separation between nearest neighbors $s = L$, where L is the fish length. (a) Back scattering cross section: black line – EM model; gray line – CDE model. The vertical dashed line denotes the frequency at which the wavelength is four times greater than s (i.e., $\lambda/s = 4$). (b) Extinction cross section: black line – EM model; gray line – CDE model. (c) Variation of $|4\pi n f_b^2/k|$ for this case.

detailed theoretical discussion of the physical differences between back and forward scattering from fish schools is also given in this reference.

The extinction cross section also exhibits this overall two peak structure for the 2 m school [Fig. 3.2(b)] but, in this case, the lower frequency peak itself also appears to split into three separate peaks, as detailed in the inset box in Fig. 3.2(b). This occurs because, while the forward scattered field is highly coherent, there are still small differences in the

propagation paths for fish located further from the source-receiver axis, leading to interference effects which cause the apparent division of the lower frequency peak. This artefact depends strongly on the spatial configuration of the school. To illustrate it, the extinction cross section was recalculated for a prolate spheroidal (rather than spherical) school, but containing the same number of fish, and with the same average nearest neighbor separation, as before. The prolate spheroid containing the fish was generated by rotating an ellipse of aspect ratio $\alpha = 3$ by 180° around the major axis, which is orientated to lie along the source-receiver direction. When this is done, more fish are distributed close to the source-receiver axis, thus reducing path differences and, consequently, interference effects. The thin gray curve in the detail window inside Fig. 3.2(b) shows σ_e for this prolate spheroidal case. It can be clearly seen that, when these interference effects are reduced, the splitting of the resonance peak is much less pronounced.

After noting the differences between EM and CDE in Fig. 3.4(b), a more specific interpretation of the differences between EM and CDE in the corresponding back scattering case of Fig. 3.4(a) can be made. Careful measurement of the divergence between EM and CDE in Fig. 3.4(b) shows that multiple scattering increases the total scattering by, at most, about 17.5%, at about 3.35 kHz. In contrast, for the back scattering case of Fig. 3.4(a), the differences between EM and CDE over the same frequency range, while variable, are generally much greater than this. In particular, at $f_0 = 2.8$ kHz, CDE predicts a scattering level about 3 times that of EM. Since essentially the same multiple scattering interactions give rise to the CDE curves in both Figs. 3.4(a) and 3.4(b), it appears most likely that the wide divergence between EM and CDE in Fig. 3.4(a) is primarily due to the resonance region laying above f_u, rather than because $|4\pi n \mathrm{f}_b^2/k| > 0.01$ over this frequency range.

3.3.2.4. Theoretical comparison of the models: Azimuthal variations

Figures 3.5(a), 3.5(b), and 3.5(c), show the azimuthal variation of $|\mathrm{f}_s|^2$ (plotted logarithmically on the radial grid of these figures) for the fish school cases shown in Figs. 3.2, 3.3, and 3.4, respectively. In each case, the variation is plotted at the single fish resonance frequency for the corresponding depth (i.e., $f_0 = 0.6$ kHz at 2 m, 1.5 kHz at 25 m, and

2.8 kHz at 65 m). The external sound field is incident at 0 deg. For Figs. 3.5(a) and 3.5(b), $f_0 < f_u$, and these both show that EM and CDE predict practically identical values of $|\mathrm{f}_s|^2$ for all scattering angles. In Figure 3.5(c), for which $f_0 > f_u$, the azimuthal variations differ, and the radial scale is expanded to emphasize this. Around 180 deg, $|\mathrm{f}_s|^2$ shows a large forward scattering lobe. This is not fully plotted in Fig. 3.5(c), since both EM and CDE predict practically identical values within the angular range of the lobe ($\approx$ 165 - 195 deg). However, outside this range, distinct differences between EM and CDE appear. Both models indicate side lobes on either side of the forward scattering lobe, but their side lobe patterns diverge as the angle turns towards the back scattering direction 0 deg, with EM typically predicting a lower scattering level. The side lobes gradually diminish, and, from about 330 deg to 30 deg, EM predicts a slowly varying value of $|\mathrm{f}_s|^2$ which is $\sim$ 30-40% of that indicated by CDE, in line with the results of Fig. 3.4(a).

3.4. Comparison with experimental data

3.4.1. Modal Lion Experiment

Diachok (1999) described an experiment, performed in the Gulf of Lion in September 1995, designed to study acoustic absorption due to fish, and fish schools, in shallow water. Estimates of the absorption coefficient α_b were obtained by matching experimental measurements and computational models of transmission loss. A new method for interpreting these data, based on forward scattering, was recently described by Raveau and Feuillade (2015), who generated estimates of the number of fish in fish schools by matching the peak frequency of the absorption data with computed values of σ_e, obtained using CDE. To run CDE, it was necessary to determine a number of input parameters, i.e., the length of the individual fish, the size of the swim bladder, the viscosity of fish flesh, the shape and dimensions of the schools, the nearest neighbor separation between fish, and the depth of the school in the water column. A detailed discussion of these parameters, based on Diachok's work, is presented in Raveau and Feuillade (2015). Table 3.2 summarizes the parameters as applied to one of Diachok's cases, which is analyzed here.

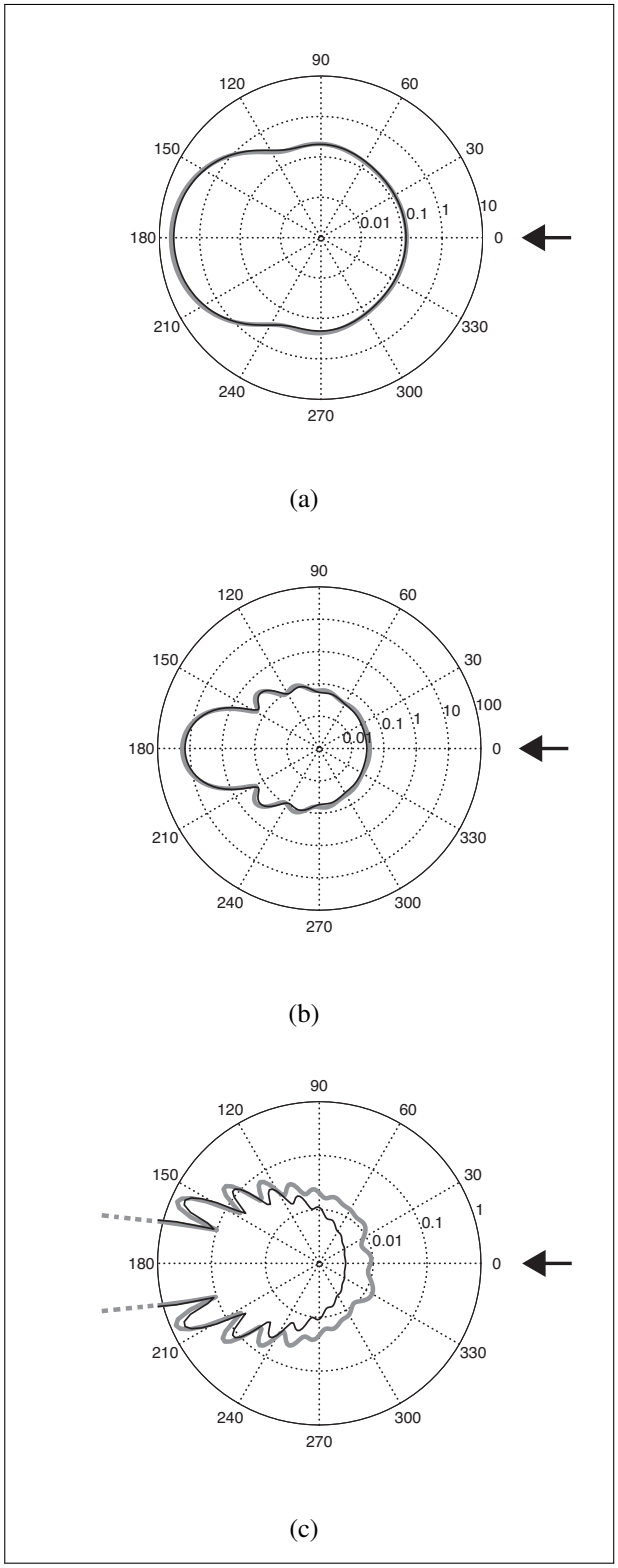

FIGURE 3.5. Azimuthal distribution of $|\mathrm{f}_s|^2$ for a spherical school of 1000 fish at: (a) 2 m depth; (b) 25 m depth; (c) 65 m depth. The arrows indicate the direction of the incident field. $|\mathrm{f}_s|^2$ is plotted logarithmically, and the values are denoted along the 15 deg radial grid line. Note the expanded scale in (c).

TABLE 3.2. Input parameters for Fig. 3.6

Parameter	Symbol	Value
Length of the fish	L	0.165 m [a]
Surface radius of swimbladder	a_0	0.079 m [b]
Viscosity	μ	20.8 $Pa \cdot s$
Depth of the school	z	65m
Number of fish in the school	N	7000
Average nearest neighbor separation	s	0.8L
Shape of the school	Oblate spheroidal, aspect ratio α = 1:3	

[a] Estimated according to the growth rate of the fish
[b] Measured at the surface

In this present work, the frequency variation of the forward scattering amplitude is computed using both CDE and EM, and estimates of σ_e obtained from them using Eq.(3.3). Comparison of these computations with Diachok's absorption data is made via the relationship between the extinction cross section and the absorption coefficient, as described by: (Medwin & Clay,1998)

$$\alpha_b = 4.34\, n\, \sigma_e\ ,\ [dB/m] \tag{3.4}$$

where α_b is the absorption coefficient in water containing n fish schools per m^3. This expression assumes that there are no scattering interactions between schools of fish in the water column, and that all of the schools are approximately the same size.

The data points in Fig. 3.6(a) are from Fig. 17 of Diachok (1999), and are attributed to absorption by sardine schools within a layer 65 m deep, and about 15 m thick, during daytime. In the reanalysis of these data by Raveau and Feuillade (2015), it is calculated that these sardine schools each contain about 7000 fish, with an average nearest neighbor spacing $s = 0.8L$. The black and gray curves in Fig. 3.6(a) show the absorption predicted by EM and CDE, respectively, by means of Eq. (3.4), using the same value of n for both methods, and incorporating the parameters of Table 3.2. CDE predicts slightly greater scattering than EM from about $1.5 - 4$ kHz, and reference to Fig. 3.6(b) shows that, over this frequency range, $|4\pi n \mathrm{f}_b^2/k| \gtrsim 0.003$, which represents a lower limit than indicated in Figs. 3.2, 3.3, and 3.4, and may be due to the oblate spheroidal, rather than spherical, school shape in this case.

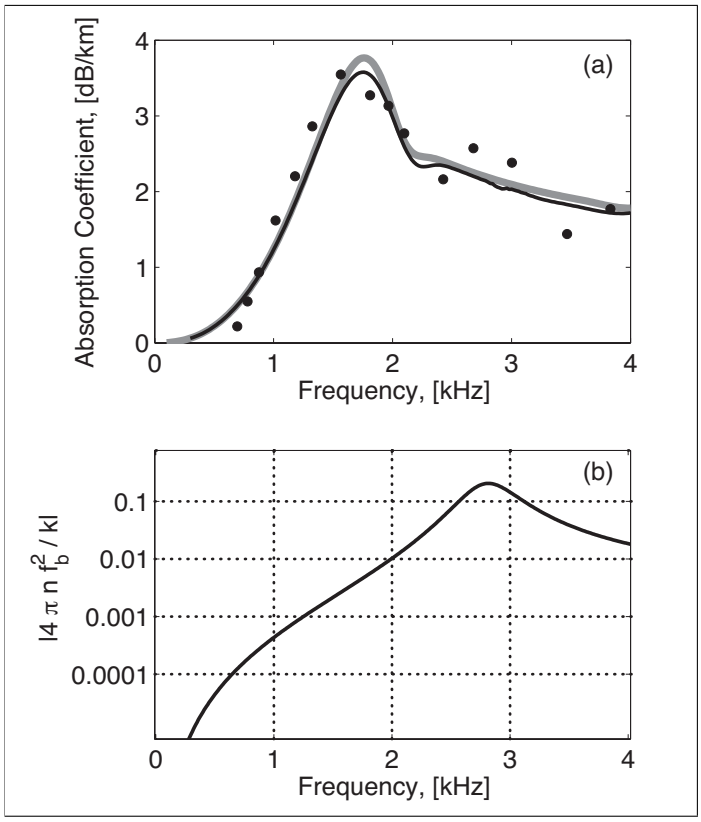

FIGURE 3.6. Sound absorption due to a school of sardines. (a) The data points are from Diachok (1999). The curves are derived from computations of the extinction cross section for an oblate spheroidal school of 7000 sardines at 65 m depth, using an average separation s=0.8L. Black line – EM. Gray line – CDE. (b) Variation of $|4\pi n \mathrm{f}_b^2/k|$ for this case.

Figure 3.6(a) shows that both CDE *and* EM agree very well with the data over the whole frequency range. As expected for this forward scattering case, there is no indication that EM is affected in any way, at higher frequencies, by an f_u condition. Also, the exclusion of multiple scattering (i.e., as in EM) causes practically no difference to the predicted theoretical fit to the absorption data. To obtain the scattering levels shown, for *both* EM and CDE in Fig. 3.6(a), the value of n required in Eq. (3.4) is $\approx 3.84 \times 10^{-5}$ schools/m^3. Since each school contains approximately 7000 fish, this would correspond to about 0.27 sardines/m^3 if the fish were evenly dispersed within the 15 m thick layer where the schools are located.

3.4.2. Target strength of a school of anchovies

In 1971, Holliday collected scattering data for several fish species in the Los Angeles Bight. (Holliday,1972) Schools were located using the ships hull-mounted sonar. The ship was positioned upwind of a school and allowed to drift through it. The acoustic source was a small explosive charge (2.5 g flash powder) detonated at 10 cm depth. Echoes were received on two omnidirectional hydrophones, with flat responses from below 10 Hz to above 20 kHz, suspended in the middle of the upper mixed layer, at depths between 10 and 40 m. Holliday attempted to sample fish from each school after a group of shots were made, using a purse seine, gill net, or hook and line. Of the five targets located during the experiment, three (targets A, B, and D) were pure schools of anchovy of approximate length 12 cm and mean calculated swim bladder volume 0.5 ml, and were estimated to be near 20, 30, and 15 m depth, respectively. From visual observation, the anchovy schools appeared to be spherical in shape, with a diameter of roughly 3 m.

In a previous article of Feuillade et al. (1996), the CDE model was compared against the anchovy data of targets A, B and D. Information about the fish length, swim bladder volume, and school depth, was obtained from Holliday's article, while the swim bladder viscosity was estimated using data suggested by Love (1978) for small physostomes. The spacing between fish was adjusted to fit the spectral distribution of the experimentally recorded target strength. Using these parameters, the normalized target strength for a single fish within a small school of 123 fish was calculated, and the overall level of the normalized curve was then adjusted to fit the experimental data. A similar analysis is performed here. However, in this case, the experimental target strength level is matched by increasing the number of fish within a spherical school. Since the targets A, B and D show similar features, only one of them (target D) is analyzed here.

Figure 3.7(a) shows the results of the model comparisons with Holliday's data for target D. The target strength variation with frequency was calculated via Eq. (3.2), using both EM and CDE, and incorporating the parameters listed in Table 3.3. Comparison with Fig. 3.7(b) shows that $|4\pi n \mathrm{f}_b^2/k| < 0.003-0.01$ throughout the frequency range of the data,

TABLE 3.3. Input parameters for Fig. 3.7

Parameter	Symbol	Value
Length of the fish	L	0.12 m
Surface radius of swimbladder	a_0	0.053 m
Viscosity	μ	30 $Pa \cdot s$
Depth of the school	z	15 m
Theoretical resonance frequency	f_0	1.1 kHz
Number of fish in the school	N	10000
Average nearest neighbor separation	s	$4L$

except possibly within the immediate vicinity of the individual fish resonance frequency, i.e., 1.1 kHz. Therefore, from the previous analysis described here, it appears very unlikely that multiple scattering contributes to the marked divergence between EM and CDE seen in the figure. The target strength values predicted by EM begin to drop off, and diverge sharply from CDE, for frequencies just above the limit corresponding to $\lambda/s = 4$ [the vertical dashed line in Fig. 3.7(a)], and it appears most probable that exceeding this limit is the reason for the failure of EM to correctly predict the target strength distribution in this back scattering case.

Since back scattering computations with CDE are strongly affected by the precise fish locations, the predicted CDE target strength variation in Fig. 3.7(a) does not fit every spectral feature exactly. However, the ensemble interactions incorporated in CDE change the primary fish resonances, and produce additional variations, resulting in spectra which closely resemble the original data.

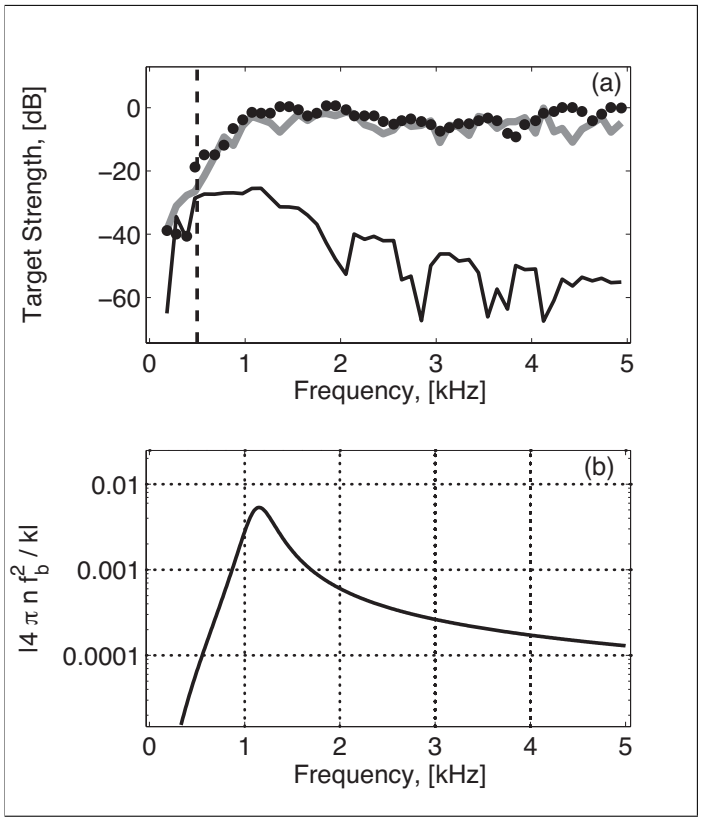

FIGURE 3.7. Back scattering from a school of anchovies. (a) The data points are from Holliday (1972). The curves are derived from computations of the back scattering cross section for a spherical school of 10000 sardines at 15 m depth, using an average separation $s = 4L$. The vertical dashed line denotes the frequency at which the wavelength is four times greater than s (i.e., $\lambda/s = 4$). Black line – EM. Gray line – CDE. (b) Variation of $|4\pi n f_b^2/k|$ for this case.

4. IMPULSE SCATTERING FROM CLOUDS OF ACOUSTICALLY COUPLED GAS BUBBLES IN FLUIDS

The present chapter introduces a new method to find the impulse response of a bubble cloud in a compressible medium, based on perturbation theory.(McComb,2004) This method provides for an approximate solution to the problem, by starting from the exact solution of a related problem. The solution is formulated by adding a "small" term (or perturbation) to the mathematical description of the exactly solvable problem.

4.1. Time domain solution for a bubble cloud

4.1.1. Simple perturbation theory

Consider an equation defined by an operator L such as:

$$L\phi(x) = f(x), \tag{4.1}$$

where $\phi(x)$ is any function that satisfies Eq. (4.1). Typically, in multiple degrees-of-freedom problems, the resulting equation (4.1) cannot be solved. However, let us consider the soluble equation:

$$L_0\phi_0(x) = f(x). \tag{4.2}$$

Suppose that the operator L can be written as:

$$L = L_0 + \epsilon L_I, \tag{4.3}$$

where ϵ is a small quantity and the subscript I refers to "interaction."(McComb,2004) Let us note that Eq. (4.1) is not the same as Eq. (4.2), and thus $\phi \neq \phi_0$. Now we assume that the exact solution $\phi(x)$ can be expressed as follows:

$$\phi(x) = \phi_0(x) + \epsilon\phi_1(x) + \epsilon^2\phi_2(x) + ..., \tag{4.4}$$

where ϕ_0, ϕ_1, ϕ_2 denote the coefficients of the ϵ-expansion. If ϵ is small, Eq. (4.4) can be truncated at a low order. Substituting from (4.4) and (4.3) in (4.1):

$$\begin{aligned} f(x) =& L_0\phi_0(x) + L_0\epsilon\phi_1(x) + L_0\epsilon^2\phi_2(x), \\ &+ \epsilon L_I\phi_0(x) + \epsilon^2 L_I\phi_1(x) + O(\epsilon^3), \end{aligned} \tag{4.5}$$

and then equate coefficients of each power of ϵ in (4.5):

$$\epsilon^0 : L_0\phi_0(x) = f(x), \tag{4.6}$$

$$\epsilon^1 : L_0\phi_1(x) = -L_1\phi_0(x), \tag{4.7}$$

$$\epsilon^2 : L_0\phi_2(x) = -L_1\phi_1(x). \tag{4.8}$$

Now we have a set of equations for ϕ_0, ϕ_1, ϕ_2, which form the solution ϕ in Eq. (4.4). The coefficients are then calculated iteratively, beginning with ϕ_0. Once we solve (4.6), ϕ_0 is used as an input of (4.7), and so on. In the previous derivation, ϵ is assumed to be small enough to truncate expansion (4.4) at a low order. Let us now define the interaction operator by:

$$L_I = L - L_0, \tag{4.9}$$

which is equivalent to $L = L_0 + \epsilon L_I$, where $\epsilon = 1$. In this case, there is no basis for truncating the expansion, hence ϵ shall be considered as a variable control parameter, where $0 \leq \epsilon \leq 1$. Therefore, $\epsilon = 0$ corresponds to the soluble case, while $\epsilon = 1$ corresponds to the exact solution.

4.1.2. Time domain CDE equations

In 1996, Feuillade et al. developed a scattering model which includes all the multiple interaction among the bubbles. If we consider an external field driving an ensemble of N

interacting bubbles, the total field incident on any bubble is the sum of the external field and the scattered fields from all of the others. The response of a whole group may be represented by a set of coupled differential equations as follows:

$$m_n\ddot{\nu}_n + b_n\dot{\nu}_n + \kappa_n\nu_n = -P_n e^{i(\omega t+\phi_n)} - \sum_{j\neq n}^{N} \frac{\rho e^{-ikr_{jn}}}{4\pi r_{jn}}\ddot{\nu}_j, \tag{4.10}$$

where ν is the differential volume (i.e., the difference between the instantaneous and equilibrium bubble volumes). The coefficient $m(=\rho/4\pi a)$ is termed the inertial "mass" of the bubble, and $\kappa(=3\gamma P_A/4\pi a^3)$ is the "adiabatic stiffness". P_n and ϕ_n are the amplitude and phase respectively of the external field experienced by the n-th bubble, and r_{jn} is the radial distance from the center of the n-th bubble to the center of the j-th bubble. Harmonic "steady-state" solutions of these coupled equations are found by substituting $\nu_n = \bar{\nu}e^{i\omega t}$ in Eq. (4.10). This leads to a matrix equation which can be solved by matrix inversion.

However, this analysis has been carried out in the frequency domain, where the time delays are represented as additional phase terms. In order to calculate the impulse response of the bubble cloud, a time domain version of the CDE method is proposed, equivalent to the equations of Ooi et al.:

$$m_i\ddot{\nu}_i + b_i\dot{\nu}_i + \kappa_i\nu_i = -\delta(t-t_i) - \sum_{i\neq j}^{N} \frac{\rho}{4\pi r_{ij}}\ddot{\nu}_j(t-t_{ji}), \tag{4.11}$$

where $\delta(t-t_i)$ represents an impulse arriving at $t=t_i$ to the i-th bubble, and the coupling term $\sum_{i\neq j}^{N} \frac{\rho}{4\pi r_{ij}}\ddot{\nu}_j(t-t_{ji})$ is the coherent summation of the pressure fields radiated by the remaining N-1 bubbles within the cloud. Let us note that the coupling term $\ddot{\nu}_j(t-t_{ji})$ includes the time delay t_{ji} between each pair of bubbles. The coupled system described in Eq. (4.11) can be written in state space, such that:

$$\dot{\mathbf{x}}_{2N\times 1} - \mathbf{A}_{\mathbf{0}2N\times 2N}\mathbf{x}_{2N\times 1} = \mathbf{B}_{2N\times N}\mathbf{u}_{N\times 1} + \mathrm{diag}\left(\mathbf{A}_{\mathbf{I}2N\times 2N}\dot{\mathbf{x}}_{\mathbf{R}2N\times 2N}\right), \tag{4.12}$$

where

$$\mathbf{x} = \begin{bmatrix} \nu_1 \\ \vdots \\ \nu_N \\ \dot{\nu}_1 \\ \vdots \\ \dot{\nu}_N \end{bmatrix}_{2N\times 1}, \mathbf{A_0} = \begin{bmatrix} \mathbf{0}_{N\times N} & \mathbf{I}_{N\times N} \\ -\mathbf{M}^{-1}\mathbf{K} & -\mathbf{M}^{-1}\mathbf{C} \end{bmatrix}_{2N\times 2N}, \mathbf{B} = \begin{bmatrix} \mathbf{0}_{N\times N} \\ -\mathbf{M}^{-1} \end{bmatrix}_{2N\times N}$$

$$\mathbf{E} = \begin{bmatrix} 0 & \frac{\rho}{4\pi r_{12}} & \cdots & \frac{\rho}{4\pi r_{1N}} \\ 0 & \ddots & \cdots & 0 \\ \vdots & \vdots & \ddots & \vdots \\ \frac{\rho}{4\pi r_{1N}} & 0 & \cdots & 0 \end{bmatrix}_{N\times N}, \mathbf{C} = \begin{bmatrix} b_1 & 0 & \cdots & 0 \\ 0 & b_2 & \cdots & 0 \\ \vdots & \vdots & \ddots & \vdots \\ 0 & 0 & \cdots & b_m \end{bmatrix}_{N\times N},$$

$$\mathbf{A_I} = \begin{bmatrix} \mathbf{0}_{N\times N} & \mathbf{0}_{N\times N} \\ \mathbf{0}_{N\times N} & \mathbf{M}^{-1}\mathbf{E} \end{bmatrix}_{2N\times 2N}, \dot{\mathbf{x}_\mathbf{R}} = \begin{bmatrix} \mathbf{0}_{N\times N} & \mathbf{0}_{N\times N} \\ \mathbf{0}_{N\times N} & \ddot{\nu}_R \end{bmatrix}_{2N\times 2N},$$

$$\mathbf{M} = \begin{bmatrix} m_1 & 0 & \cdots & 0 \\ 0 & \ddots & \cdots & 0 \\ \vdots & \vdots & \ddots & \vdots \\ 0 & 0 & \cdots & m_N \end{bmatrix}_{N\times N}, \mathbf{K} = \begin{bmatrix} \kappa_1 & 0 & \cdots & 0 \\ 0 & \kappa_2 & \cdots & 0 \\ \vdots & \vdots & \ddots & \vdots \\ 0 & 0 & \cdots & \kappa_m \end{bmatrix}_{N\times N},$$

$$\mathbf{u} = \begin{bmatrix} \delta(t-t_1) \\ \delta(t-t_2) \\ \vdots \\ \delta(t-t_N) \end{bmatrix}_{N\times 1} \quad \text{and } \ddot{\nu}_R = \begin{bmatrix} 0 & \ddot{\nu}_1(t-t_{12}) & \cdots & \ddot{\nu}_1(t-t_{1N}) \\ 0 & \ddots & \cdots & 0 \\ \vdots & \vdots & \ddots & \vdots \\ \ddot{\nu_N}(t-t_{1N}) & 0 & \cdots & 0 \end{bmatrix}_{N\times N}$$

If we leave the term $\mathrm{diag}\,(\mathbf{A_{I}}_{2N\times 2N}\dot{\mathbf{x}}_{\mathbf{R}2N\times 2N})$ out of Eq. (4.12), the remaining equation takes the form of a linear system with input $\mathbf{u}(t)$, which can be solved by conventional methods.(Ogata,2004;Chen,1999) Considering the term $\mathrm{diag}\,(\mathbf{A_{I}}_{2N\times 2N}\dot{\mathbf{x}}_{\mathbf{R}2N\times 2N})$ as an external perturbation, the methodology described in Section 4.1.1 can be used to obtain the solution of Eq. (4.12):

$$L(\mathbf{x}) = \mathbf{Bu}, \tag{4.13}$$

where

$$\begin{aligned} L &= L_0 + \epsilon L_I, \\ L_0 &: \frac{d}{dt} - \mathbf{A_0}, \\ L_I &: -\mathbf{A_I}\frac{d}{dt}. \end{aligned} \tag{4.14}$$

If $\epsilon = 1$, the operator L leads to the exact solution of Eq. (4.12). Following the methodology described in Section 4.1.1 (Eqs. 4.4 to 4.8), the problem is re-expressed as:

$$\epsilon^0 : L_0\phi_0 = f \longrightarrow \dot{\phi_0} - \mathbf{A_0}\phi_0 = \mathbf{Bu}, \tag{4.15}$$

$$\epsilon^1 : L_0\phi_1 = -L_1\phi_0 \longrightarrow \dot{\phi_1} - \mathbf{A_0}\phi_1 = -\mathbf{A_I}\dot{\phi_0}, \tag{4.16}$$

$$\epsilon^2 : L_0\phi_2 = -L_1\phi_1 \longrightarrow \dot{\phi_2} - \mathbf{A_0}\phi_2 = -\mathbf{A_I}\dot{\phi_1}. \tag{4.17}$$

4.1.3. Solving the uncoupled problem

Since the input $\mathbf{u}$ of the uncoupled problem $\dot{\phi_0} - \mathbf{A_0}\phi_\mathbf{0} = \mathbf{Bu}$ consists of a series of impulses, an analytic solution can be found for $\phi_\mathbf{0}$. Since the arrival time depends upon the distance between the source and each bubble, a solution of the type $\mathbf{RI} = e^{\mathbf{A}t}\mathbf{B}\left[1 \quad 1 \quad 1 \ldots 1\right]^T$ cannot be applied in this case. It is possible to derive a concise analytic solution using a matrix exponential, however the computational cost would be considerable for bigger clouds. Therefore, a modal coordinates solution is proposed:

$$\sigma_j(t) = \int_0^t e^{\lambda_j(t-\tau)}\widetilde{\mathbf{B}}(j,:)\mathbf{u}(\tau)d\tau, \tag{4.18}$$

$$\phi_\mathbf{0} = \mathbf{\Psi}\sigma \quad \sigma \text{ :new coordinates ,} \tag{4.19}$$

where λ_i are the eigenvalues of $\mathbf{A_0}$, $\mathbf{\Psi}$ is the matrix whose columns are the eigenvectors of $\mathbf{A_0}$. $\widetilde{\mathbf{B}}(j,:)$ corresponds to the j-th column of the product $\mathbf{\Psi}^{-1}\mathbf{B}$. Let us note that the product $\widetilde{\mathbf{B}}(j,:)\mathbf{u}$ is a scalar quantity. Assuming zero initial conditions for all the variables, Eq. (4.18) may be re-expressed as:

$$\sigma_j(t) = \int_0^t e^{\lambda_j(t-\tau)}[\widetilde{\mathbf{B}}(j,1)\delta(\tau - t_1) + \ldots + \widetilde{\mathbf{B}}(j,N)\delta(\tau - t_N)]d\tau.$$

Using Dirac delta properties:

$$\sigma_j(t) = e^{\lambda_j(t-t_1)}\widetilde{\mathbf{B}}(j,1) + \ldots + e^{\lambda_j(t-t_N)}\widetilde{\mathbf{B}}(j,N). \tag{4.20}$$

4.1.4. Encapsulated bubbles

In a classic work published in 1989 by Commander and Prosperetti, a rigorous model for the propagation of pressure waves in bubbly liquids was formulated. Combining Eqs. (27) and (32) from Commander and Prosperetti (1989) yields to a linearized expression for the resonance frequency of the radial motion of a non-encapsulated and isolated bubble:

$$\omega_0^2 = \frac{P_0}{\rho_l a^2}\left(3\gamma - \frac{2\sigma}{aP_0}\right), \tag{4.21}$$

where a indicates the bubble equilibrium radius, P_0 is the undisturbed pressure in the bubble, ρ_l is the liquid density, σ is the surface tension at the liquid-gas interface and γ represents the ratio of specific heats in air.

Church derived a model for a collection of encapsulated bubbled, by considering an elastic shell in the liquid-air interface. Since the resonance frequency and the damping are affected by the shell, it was necessary to develop new expressions for those parameters:(Church,1995)

$$\omega_0^2 = \frac{P_0}{\alpha\rho_s a_1^2}\left\{3\gamma - \frac{2}{P_0}\left(\frac{\sigma_1}{a_1} + \frac{\sigma_2}{a_2}\frac{a_1^3}{a_2^3}\right) + \frac{4V_s G_s}{a_2^3 P_0}\left[1 + Z\left(1 + \frac{3a_1^3}{a_2^3}\right)\right]\right\}, \tag{4.22}$$

$$Z = \left[\frac{2\sigma_1}{a_1} + \frac{2\sigma_2}{a_2}\right]\frac{a_2^3}{V_s}\frac{1}{4G_s},$$

$$\alpha = \left[1 + \left(\frac{\rho_l - \rho_s}{\rho_s}\right)\frac{a_1}{a_2}\right],$$

where ρ_s, G_s represent the density and shear modules of the shell material; a_1, a_2 are the internal and external bubble radius, V_s is defined as $a_2^3 - a_1^3$ and σ_1, σ_2 denote the surface tension of the gas-shell and shell-liquid interfaces, respectively.

The terms for the viscous damping in the liquid, the thermal damping, and acoustic re-radiation damping also contain modifications due to the presence of the shell:

$$\beta_{\mathrm{vis},L} = \frac{2\mu_l}{\rho_s a_1^2}\frac{a_1^3}{a_2^3\alpha}, \qquad \beta_{\mathrm{th}} = \frac{2\mu_{\mathrm{th}}}{\rho_s a_1^2\alpha}, \qquad \beta_{\mathrm{ac}} = \frac{\omega}{c}\left(\frac{\omega a_2}{c}\right)\left[1 + \left(\frac{\omega a_2}{c}\right)^2\right]^{-1}. \tag{4.23}$$

An expression for $\mu_{\rm th}$ may be found in Eq. (14) from Prosperetti (1977). Substitution of $\mu_{\rm th}$ into $\beta_{\rm th}$ yields:

$$\beta_{\rm th} = \frac{P_0}{2\rho_s \omega a_1^2 \alpha} \mathsf{Im}(\Phi), \tag{4.24}$$

where

$$\Phi = \frac{3\gamma}{1 - 3(\gamma - 1) i\chi \left[(i/\chi)^{1/2} \coth(i/\chi)^{1/2} - 1 \right]}, \tag{4.25}$$

and $\chi = D/\omega a_1^2$, where D is the gas thermal diffusivity . The expressions of Φ and χ correspond to Eqs. (27) and (28) of Commander and Prosperetti (1989), respectively.

The new damping term also incorporates an additional term for the viscous damping due to the shell material.

$$\beta_{{\rm vis},s} = \frac{2\mu_s}{\rho_s a_1^2} \frac{V_s}{a_2^3 \alpha}, \tag{4.26}$$

4.2. Data analysis

A series of experiments were performed at the Lake Travis Test Station, Applied Research Laboratories (ARL, The University of Texas at Austin), to measure the attenuation of sound through an artificial bubble cloud, consisting of 14 fixed air-filled latex balloons of 4.68 cm radius at the surface.(Dolder,2014;Enenstein,2014) The balloons were attached by a nylon netting grid to a steel cage of dimensions 1.22 m in height and base area 1.30 m by 1.30 m, as shown in Fig. 4.1. Three balloon configurations were used, but in the present work just one of them will be analyzed.

The source was a Navy J-13, which is an approximately omnidirectional electromagnetic loudspeaker designed to operate between 30 and 3000 Hz at depths up to 20 meters. Linear chirps from 30 Hz to 2 kHz produced by the J-13 were recorded by nine HTI-90-U hydrophones, located at 2 meter intervals of depth from 2 meters to 18 meters, at a horizontal distance of 11.7 meters from the center of the bubble cloud, as shown in Fig. 4.2.

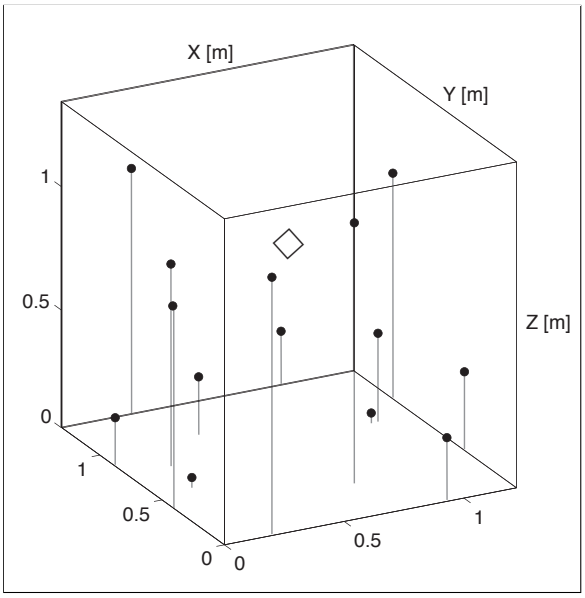

FIGURE 4.1. The location of each of the 14 balloons is shown along with a local coordinate system associated with the steel frame that held the balloons. The balloon location appear in Table G.3 of Dolder (2014). The source is depicted with the diamond-shape symbol.

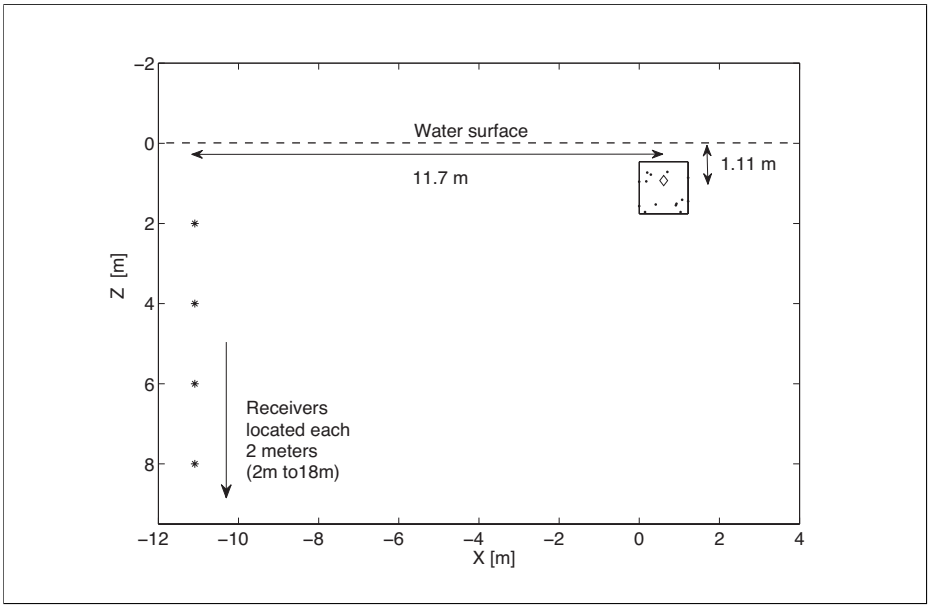

FIGURE 4.2. Experimental apparatus. The water depth at the source position was 19.6 m and the depth at the receiver position was 19.1 m. The bubble frame and the source are shown on the right. The source is depicted by the diamond symbol. The air-filled balloons are depicted by the solid black dots. On the left, the hydrophones are depicted using asterisks. The source was located at a depth of 1.11 m from the surface.

The source signal and all the hydrophone signals were digitized by a Data Translation DT9837B data acquisition module. Transfer functions between each hydrophone signal and the source signal were calculated using Data Translation's VIBPoint Framework software. These transfer functions represent the acoustic pressure recorded at each hydrophone normalized by the source signal voltage. Transfer functions were measured with and without the bubble cloud. A measurement technique that had been previously used to study small bubbles was used here to isolate the acoustic effect of the bubble cloud scattering.(Leighton et al.,2002) According to this technique, the received signal at the measurement hydrophone $y(t)$, can be considered as the superposition of two components, i.e.,

$$y(t) = y_d(t) + y_s(t), \tag{4.27}$$

where $y_d(t)$ is the signal due to the direct field (in the absence of bubbles), and $y_s(t)$ is the signal arising from the acoustic field generated by scattering from the bubble cloud. It is possible then to estimate the field scattered from the bubbles by subtracting the two measurable quantities $y_d(t)$ and $y_s(t)$. The difference between those quantities shows the impact of adding bubbles to the system:

Transfer functions are generally defined in the frequency domain, and represented as a complex function of the frequency. The corresponding impulse response (i.e. the time domain representation of the transfer function) can be obtained by performing an inverse Fourier transform (IFFT). Since the Fourier transform is a linear operator, the superposition defined in Eq. (4.27) is valid in both the frequency and time domains. After the subtraction, nine different curves were found, corresponding to the nine hydrophone locations. Each curve represents the transfer function for the bubble group, measured at a given depth.

According to the classic wave theory, the phase relation between the driving oscillation and the oscillation of the bubble depends upon the frequency: they are in phase with each other below resonance, they are in quadrature at resonance, and in anti-phase above resonance. (French,1971) Figure 4.3 shows the phase as a function of frequency, for

the measured transfer function (solid line). The dash-dotted line represents the theoretical phase response of the bubble group, calculated with a frequency dependent model developed by Feuillade et al. (1996). Both the modeled and measured phase response show the reversal of phase for frequencies above the resonance.

It has been reported in the literature that shallow water measurements evidence a strongly nonlinear phase, especially at low frequency. This behavior suggests that the sub-bottom structure plays an important role in sound reflection. By contrast, a linear cross-spectral phase would imply that the source-receiver propagation is dominated by a single path.(Guillon et al.,2011) Measurements performed in Lake Travis also exhibit the nonlinear phase behavior (solid line in Figure 4.3), which confound the comparison with theoretical predictions. Since scattering models are usually developed in the free field and subsequently included as an input in full propagation models, it is not intended to incorporate reflections from layered boundaries in the present work. A phase adjustment of the measured data was performed, which is depicted in Figure 4.3.

4.3. Results

4.3.1. Model Implementation

A time-domain model was implemented to calculate the impulse response of a cloud of bubbles, based on the perturbation theory solution explained in Section 4.1.2. The model was tested against the transfer functions measured in Lake Travis for the group of fixed balloons. This technique was also compared with a numerical benchmark, which includes all the multiple interactions and time delays.

It is first necessary to determine a number of input parameters, to provide a starting point to run the bubble scattering model. The model requires information about the bubble size, damping, and individual resonance frequency. It is also required to know the relative positions among the source, bubbles and receiver, which strongly affect the individual phase response, and therefore, the total interference pattern. In the present experiment, all the relative positions are known, as well as the balloon radii.

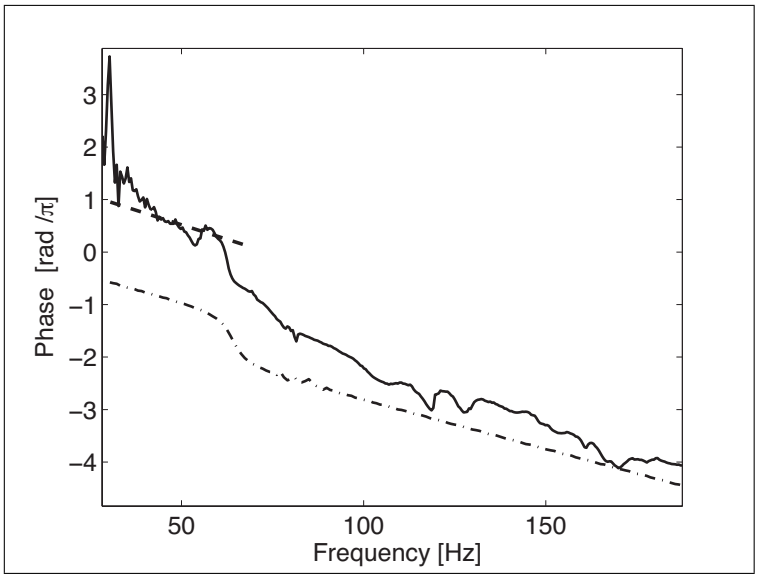

FIGURE 4.3. Phase response of the bubble cloud for the receiver located at 6 m depth. Solid line: phase of the measured transfer function, after the subtraction. Dash-dot line: theoretical phase response, calculated using a frequency dependent scattering model (Feuillade et al.,1996). The dash segment of line represents the slope of the measured phase in the linear zone below resonance. For the phase adjustment, the measured curve is transposed until the dash line coincides with the dash-dot line. In other words, the phase was adjusted to match the theoretical phase below the resonance frequency.

The physical parameters input to the modified resonance frequency model and damping given by Eqs. (4.22) to (4.26) are summarized in Table 4.1. The shear modulus and viscosity were not measured for the specific shell material used in the experiment. Following Lee, McNeese, Tseng, Wochner, and Wilson (2012), these parameters were estimated using viscoelastic master curves that were obtained for natural rubber. In this work, an AA 165-5 formulation for natural rubber was used. The coefficients for generating these master curves are given on p. 147 of Capps (1989).

Figure (4.4) shows the damping components calculated for the 10 Hz to 2000 Hz frequency range. The total damping was calculated as $\beta_{\text{total}} = \beta_{\text{ac}} + \beta_{\text{th}} + \beta_{\text{vis},L} + \beta_{\text{vis},s}$. Since the IR model implemented is a time-domain method, a frequency dependent damping parameter cannot be included. Therefore, a constant value was used in the model implementation, corresponding to the total damping at the resonance frequency $\beta_{\text{total}} \approx 10$. Future

TABLE 4.1. Physical parameters for resonance frequency model and damping

Parameter	Symbol	Value	Units
Shell material density	ρ_s	998	kg/m^3
Shear modulus of shell	G_s	0.75[b]	MPa
Liquid density	ρ_l	990	kg/m^3
Liquid viscosity	μ_l	0.001	MPa
Internal radius	a_1	4.68	cm
Shell wall thickness	r_s	0.254	mm
Ratio of specific heats (air)	γ	1.4	
Thermal conductivity for air	D	2×10^{-5}	m^2/s
Surface tension in gas-shell interface	σ_1	25 [a]	N/m
Surface tension in shell-liquid interface	σ_2	5	N/m
Hydrostatic pressure at mean bubble depth	P_0	1.12×10^5	Pa

[a] Mean value over the range 10-2000 Hz.

[b] Following Lee et al. (2012), σ_1 and σ_2 were selected such that their sum was equal to 30. The value of each tension is less important that the sum of both, due to the very small difference between the internal and external radii.

work should include a time dependent damping parameter, which responds in a different way to transient and stationary states.

The individual bubble resonance frequency is also affected by the elastic shell. Using Church's model (Eq. (4.22)) with the physical parameters indicated in Table 4.1, a resonance frequency of 77 Hz was predicted for the bubble size used in the present experiment. However, a discrepancy between measurements and the Church model prediction has recently been reported. According to Lee et al. (2012), for balloon radii ranging from 1.6 cm to 3.5 cm, the measured resonance frequencies of the natural latex balloons deviated from Church's model by 11% or less. Subsequent adjustments indicate a better match for a resonance frequency of 83 Hz, which is similar to the deviation reported by Lee et al., under similar circumstances.

Once the Eqs. (4.11) are solved, the total scattered pressure field for the whole group is given by the coherent summation:(Lamb,1945)

$$p_s(r) = \frac{\rho_l}{4\pi r} \sum_{i=1}^{N} \ddot{\nu}_i(t - t_{ri}), \tag{4.28}$$

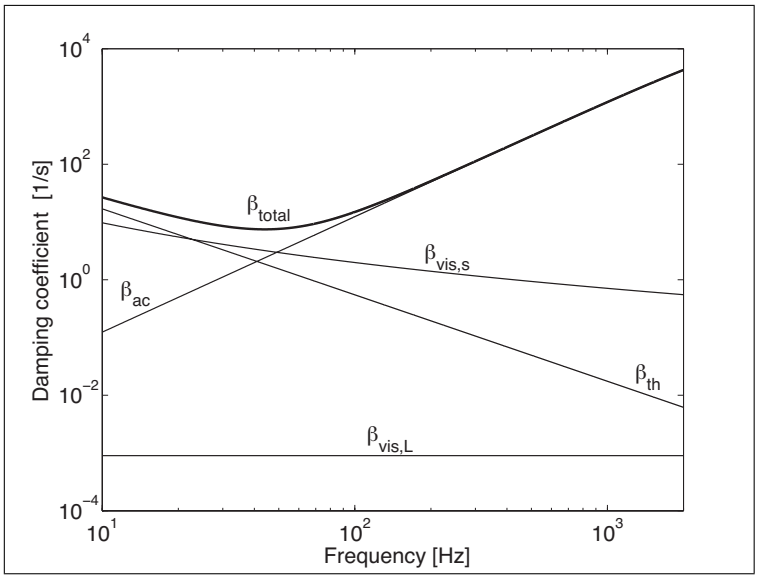

FIGURE 4.4. Dimensional linear damping constants versus frequency for a bubble radius of 4.68 cm. The components $\beta_{\rm ac}$, $\beta_{\rm th}$, $\beta_{{\rm vis},L}$, $\beta_{{\rm vis},s}$ were calculated using the expressions given by Eqs. (4.22) to (4.26) and the physical parameters indicated in Table 4.1. An AA 165-5 formulation for natural rubber was used. The coefficients for generating these master curves are given on p. 147 of Capps (1989).

where ρ_l is the liquid density, and t_{ri} is the time delay between the receiver and the i-th bubble. The scattered pressure field $p_s(r)$ represents the impulse response of the bubble group in the free field, i.e. in the absence of boundary reflections.

4.3.2. Perturbation Theory solution.

The inputs previously determined were used to formulate the operators L_0 and L_I, defined in (4.14). As it was previously formulated, the solution of the coupled system (4.11) is defined as the expansion in ϵ: $\phi(t) = \phi_0(t) + \epsilon\phi_1(t) + \epsilon^2\phi_2(t) + ...$ The first term of the expansion corresponds to the solution of equation (4.15), which can be analytically solved using expression (4.20). The functions ϕ_n were iteratively calculated as the solution of $\dot{\phi_{\mathbf{n}}} - \mathbf{A_0}\phi_{\mathbf{n}} = -\mathbf{A_I}\dot{\phi}_{n-1}$, using a fourth order Runge-Kutta algorithm. Since ϵ is considered as a variable control parameter, the exact solution ϕ will occur when $\epsilon = 1$. It is possible to choose a smaller value of ϵ and truncate the expansion at a lower order, but it may degrade the solution. A value of $\epsilon = 1$ was used in this work.

According to McComb (2004), even when ϵ is small, the perturbation expansion is not convergent. However, in practice one may still obtain a good approximation to $\phi(t)$ by taking a finite number of terms and neglecting the remainder (asymptotic convergence). In order to truncate the expansion, a criterion must be introduced. Let us say that convergence is reached when the relative error between ϕ_n and ϕ_{n+1} is less than a tolerance value. The convergence of the ϵ-expansion will be determined by the interaction operator L_I. In our case, L_I depends upon the matrix A_I, which consists of all the acoustic interactions between bubbles. Since all ϕ_n functions are related to ϕ_0, the operator L_I will also depend upon the physical parameters included in A_0.

As the operators L_I and L_0 are defined for this case, the amplitude for ϕ_n grows exponentially with n. For higher orders of n the solutions will require extended precision, which would imply significantly higher computational cost. Therefore, an alternative methodology was implemented, based on the decay of the impulse response. It can be noticed from Figure (4.5), that higher orders of ϕ_n affect later times. In other words, a longer simulation window will require more functions ϕ_n to converge to the solution ϕ. Since the amplitude of ϕ decays with time, the later time points will not depend strongly on the first ones. Therefore, it is possible to stop the computations at a certain time $t = \tau$, and restart it again as an initial value problem for the next time window. In this way, all the ϕ_n functions will be calculated up to $t = \tau$, and added together to obtain the solution ϕ. For the next time window, a new ϕ_0 is obtained as the solution of the initial value problem $\dot{\phi_\mathbf{0}} - \mathbf{A_0}\phi_\mathbf{0} = 0$, where the initial condition $\phi_0(\tau)$ corresponds to $\phi(t = \tau)$, i.e. the last value of the solution ϕ for the first window. For the second time window, all the ϕ_n functions must be calculated using the new ϕ_0. The simulation can be rebooted as many times as needed. In this way, a long time window can be split into shorter windows of length τ, reducing the order of the ϕ_n functions needed, and therefore, the computing time.

However, the solution cannot be restarted time to time, since the input term in $\dot{\phi_\mathbf{n}} - \mathbf{A_0}\phi_\mathbf{n} = -\mathbf{A_I}\dot{\phi}_{n-1}$ consists of past values of ϕ_{n-1}. Consequently, each reboot will lose some information about the first time steps, when no past values are available. Accordingly, the time interval τ should be long enough so that the missing values are negligible

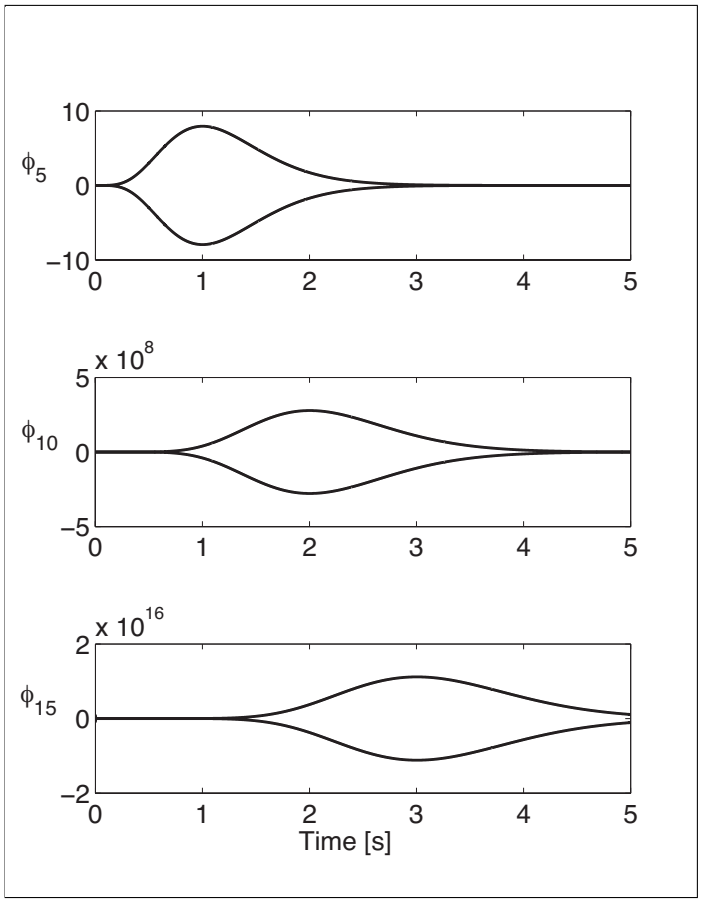

FIGURE 4.5. (a) ϕ_5 , (b) ϕ_{10} , (c) ϕ_{15}. Only the envelope of the functions are shown in the figure. Note the variation of the maximum amplitude in each case.

compared to the interval. The value of τ can be chosen as the mean lifetime of ϕ_0, i.e. $\tau = \frac{1}{\lambda}$, where λ denotes the average eigenvalue of A_0. Since the interaction between bubbles adds damping to the system, the decay of ϕ_0 will be the minimum decay of the total system.

4.3.3. Perturbation - Benchmark comparison.

A numerical benchmark was also implemented to solve Eqs. (4.11), using a fourth order Runge-Kutta algorithm. Looking at Eq. (4.12), the input consists of two terms: the impulse signal coming from the source ($\mathbf{Bu}$) and the multiple scattering among the bubbles ($\mathbf{A_I \dot{x}_R}$). The input $\mathbf{u}$ consists of a series of delayed impulses $\delta(t - t_n)$, where the arrival time t_n will depend upon the distance between the source and the n-th bubble. Since both

the impulse and the acoustic interactions are delayed, for each time step the input will depend on past values of $\mathbf{x}$, which were already calculated. For the first time steps, there will be some cases when the interaction delays lead to negative values. This implies that the scattered field from one bubble has not yet reached the other bubbles. In which cases, there is no interaction between the two bubbles and the corresponding term is zero.

An additional difficulty is the impulse implementation. The Dirac delta function can be numerically represented as the limit of a Gaussian function, such as (Hassani,2013)

$$\delta(x - x') = \lim_{\xi \to 0} \frac{1}{\sqrt{\xi \pi}} e^{-\frac{(x-x')^2}{\xi}}. \tag{4.29}$$

In the limit $\xi \to 0$, the amplitude of this function goes to infinity, while its width goes to zero. For any $\xi \neq 0$,

$$\int_{-\infty}^{\infty} \frac{1}{\sqrt{\xi \pi}} e^{-\frac{(x-x')^2}{\xi}} dx = 1. \tag{4.30}$$

This relation holds for any ξ. For the input implementation, the value of ξ was calibrated by matching the general amplitude and shape of the numerical benchmark and the perturbation-based solution. Figure 4.6(a) shows the impulse response for the differential volume of one bubble, when $\xi = 0.0077$. A reasonable agreement between the numerical benchmark and the perturbation-based solution is observed from Figure 4.6(a). The similarity of two signals X and Y can also be determined using a mathematical tool called magnitude squared coherence (MSC).(Carter et al.,1973) The coherence spectrum is defined by the squared cross spectrum divided by the product of the two autospectra (Jones,2012)

$$C_{XY}(\omega) = \frac{|G_{XY}(\omega)|^2}{G_{XX}(\omega) \cdot G_{YY}(\omega)}, \tag{4.31}$$

where ω indicates the frequency domain, G_{XY} is the cross spectral density, and G_{XX}, G_{YY} are the autospectra of signals X and Y, respectively. Figure 4.6(b) shows the MSC estimator when X denotes the perturbation-based solution and Y is the numerical benchmark. The MSC was calculated using Welch's overlapped averaged periodogram method,(Welch,1967)

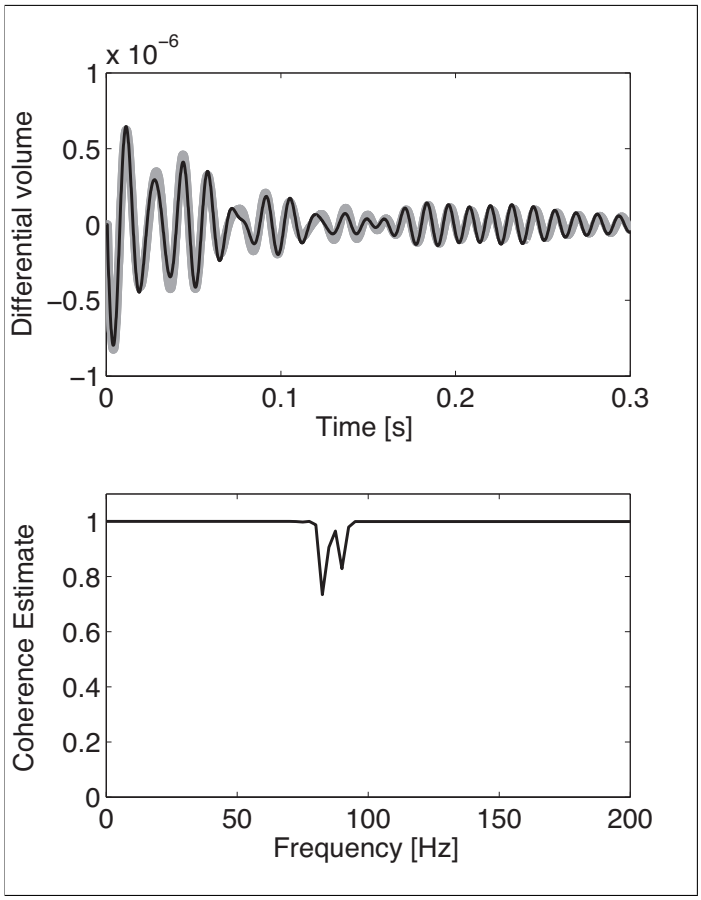

FIGURE 4.6. (a) Theoretical comparison between numerical benchmark (black line) and the perturbation-based solution (gray line). (b) Coherence estimator between both curves.

which is implemented in the MATLAB Signal Processing Toolbox (*mscohere*). The coherence is nearly always very close to unity, except for a region around the individual bubble resonance, where it has a minimum value of 0.75, which indicates a relatively high degree of similarity between the two signals.

The stability of coupled delay differential equations has received substantial attention from researchers since the early 1970s. This problem can be addressed by using a Lyapunov-Krasovskii functional, a time domain methodology to investigate the stability properties of linear time-delay systems.(Papachristodoulou et al.,2005) While a comprehensive stability analysis is not performed in this work, an observation may be made. For our study, the perturbation-based solution behaves in more stable way than the numerical

TABLE 4.2. Input parameters for Figure 4.9

Parameter	Symbol	Value
Surface bubble radius	a_0	0.0468 m
Damping constant	β	10 $1/s$
Average bubble depth	z	1.1 m
Theoretical resonance frequency	f_0	83 Hz
Number of bubble in the cage	N	14

benchmark. The latter did not work for time steps longer than 0.1 ms., while the former ran for time steps as long as 2 ms. An extension of this work should include a comprehensive analysis of the model stability, as a function of the time resolution, the physical parameters and the time delays.

4.3.4. Perturbation - Data comparison

The perturbation-based solution was also tested again the data described in Section 4.2. The experimental impulse response, obtained by performing an inverse Fourier transform on the measured transfer function, was compared with the pressure impulse response calculated using Eq. (4.28). The differential volume $\nu(t)$ for each bubble was calculated as the solution of the coupled system (4.11) for $\epsilon = 1$, i.e. $\nu(t) = \phi(t) = \phi_0(t)+\phi_1(t)+\phi_2(t)+...$, where $\nu(t)$ is a $2N \times 1$ vector, and N is the number of bubbles. The total simulated time was 0.4 s, corresponding to two blocks of 0.2 s. For each block, it was necessary to calculate 200 functions to reach convergence. The physical bubble parameters used in the simulation were previously described in Section 4.3.1, and are summarized in Table 4.2.

The acoustic field described by Eqs. (4.11) assumes a free field, i.e. the acoustic field in the receiver position is only due to the direct propagation from the bubbles and the incident field, and not from boundary reflections. Scattering models are usually developed for free field conditions, and subsequently incorporated as an input in propagation models. A comprehensive sound propagation analysis would include sea surface and layered bottom reflections, refraction effects and internal waves, among others. Even when it is not intended to implement a full propagation model, it is necessary to include certain reflections to represent the variation in the peak amplitude registered by the different hydrophones.

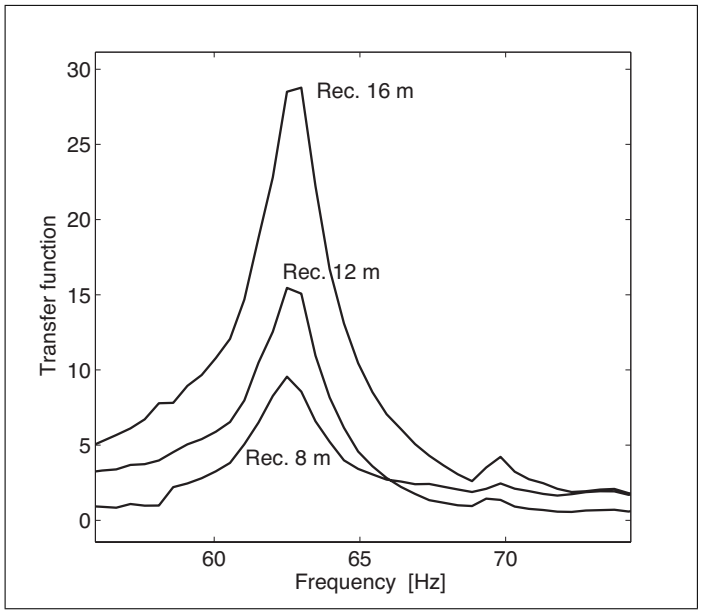

FIGURE 4.7. Variation of transfer function with frequency, for receivers located at 8 m, 12 m, and 16 m. depth.

Figure 4.7 shows the frequency variation of the transfer function, for the hydrophones located at 8 m, 12 m and 16 m depth. This figure illustrates how the amplitude of the transfer function changes at different points in the water column. An interesting feature to note from Figure 4.7 is the downshift in the peak frequency by multiple scattering effects. According to Eq. (4.22), the individual resonance frequency should be around 80 Hz, while this figure shows the peak at 63 Hz. The peak frequency of the collective resonance of the bubble cloud typically shifts down to a lower frequency than that of an individual bubble, due to radiative coupling between the bubbles. The magnitude of this shift effect increases as the number of bubbles is increased, and the separation among them is reduced. This behavior has been well documented in literature for various systems of interacting resonators. (Feuillade et al.,1996;Twersky,1962;Weston,1966)

In order to represent the peak amplitude variation shown in Figure 4.7, first and second order reflections from sea surface and ocean bottom were incorporated in the impulse response solution. The reflected signal is estimated by delaying the free-field response in time, according to the total propagation path for each case. For example, the path for the

first-order sea surface reflection, will be equal to the average distance between the bubbles and the sea surface point G, plus the distance between this point and the receiver. G is the point at which the incident wave strikes the reflecting surface, considering specular reflection. This is just a first approximation to include propagation effects in the hydrohone position, since reflections in sea surface are usually diffusive, and bottom reflections depend upon the seabed composition. Once the free-field impulse response is calculated, the total impulse response is estimated as:

$$\begin{aligned} \mathrm{IR}_{\mathrm{total}}(r,t) =& \mathrm{IR}_{\mathrm{free}}(r,t) + \mathrm{R_B}\mathrm{IR}_{\mathrm{free}}(r,t-t_{\mathrm{B}}) + \mathrm{R_S}\mathrm{IR}_{\mathrm{free}}(r,t-t_{\mathrm{S}}), \\ &+\mathrm{R_B}\mathrm{R_S}\mathrm{IR}_{\mathrm{free}}(r,t-t_{\mathrm{BS}}) + \mathrm{R_S}\mathrm{R_B}\mathrm{IR}_{\mathrm{free}}(r,t-t_{\mathrm{SB}}), \end{aligned} \tag{4.32}$$

where $\mathrm{IR}_{\mathrm{free}}$ is the impulse response in free-field, and $\mathrm{R_B}$, $\mathrm{R_S}$ denote the reflection coefficient for the ocean bottom and sea surface (top boundary), respectively. Similarly, the subscripts B and S in the time delays, stand for "bottom" and "surface" reflections. In expression (4.32), each reflection is represented by a retarded function multiplied by a constant factor. For example, $\mathrm{R_B}\mathrm{IR}_{\mathrm{free}}(r,t-t_{\mathrm{B}})$ designates the first order bottom reflection, where $t_{\mathrm{B}} = d_{\mathrm{B}}/c$ and d_{B} is the propagation distance for the first bottom reflection. Similarly, the term $\mathrm{R_S}\mathrm{R_B}\mathrm{IR}_{\mathrm{free}}(r,t-t_{\mathrm{SB}})$ denotes a second order reflection, where $t_{\mathrm{SB}} = d_{\mathrm{SB}}/c$ and d_{SB} is the propagation distance for an incident wave hitting the sea surface and then the ocean bottom, before reaching the receiver location.

The reflection on the ocean bottom depends upon the geoacoustic properties for the seafloor and the grazing angel, i.e. the angle between the beam and the surface. The bottom structure of Lake Travis consists of layers of unconsolidated mud, chalk/limestone and a very hard layered limestone.(Stotts et al.,2006) Using tabulated values of density and sound speed,(Steele et al.,2009) the reflection coefficient was calculated using Rayleigh's expression for each receiver.(Steele et al.,2009) The estimated average value of R_{B} is 0.62 for chalk, and 0.76 for limestone. Since Rayleigh's expression is valid for a single interface, it is not possible to determine an effective reflection coefficient. Also, the sea floor is covered

by layers of sediments, which affects the amplitude and phase of the reflected beam. However, it is expected that the average value of R_{B} is near 0.62 - 0.76. On the other hand, the reflection from the sea surface is even harder to determine, since it is also frequency dependent and sensitive to the surface roughness.(Steele et al.,2009) What we do know is that the water/air interface, approached from the water side, is called a "pressure-release" surface for underwater sound, and the reflected pressure is phase-reversed.(Medwin & Clay,1998)

The coefficients $\mathrm{R_B}$ and $\mathrm{R_S}$ were found by matching the peak amplitudes for the experimental and modeled transfer function. The latter was estimated by performing the Fourier transform of the calculated impulse response, including the reflections (Eq. 4.32). Although $\mathrm{R_B}$ and $\mathrm{R_S}$ depend upon the grazing angle, a single value was chosen for all the nine receivers. Future work may include angular and frequency dependent coefficients. Figure 4.8 shows the best match for the peak amplitudes, when $\mathrm{R_B} = 0.7$ and $\mathrm{R_S} = -0.1$. According to the literature, the reflection coefficient for a flat pressure-release surface should be close to $\mathrm{R_S} = -1.0$. However, the barge from which the experiment was conducted was floating on the surface on the water, therefore part of the reflection is coming from the bottom of the barge, which consist of metal containers filled with foam to provide flotation. The value of $\mathrm{R_S} = -0.1$ found by matching the peak amplitudes indicated that the average reflection coefficient under the barge is still negative, but with absolute value less than unity.

Figure 4.9 shows the pressure impulse response of the bubble system, for the receivers located at 2 m, 6 m and 12 m depth. The results for the remaining receivers are similar to the cases shown here, and therefore will be omitted. Each experimental curve was obtained by performing an inverse Fourier transform on the corresponding measured transfer function, after the phase adjustment described in Section 4.2. For all the three cases, the measured data shows a fundamental frequency that is very similar to the modeled fundamental frequency, as well as other transient features that match between measurements and model. Figure 4.9 also shows a good agreement for the general amplitude, as it is expected from Figure 4.8. In addition, the measured data shows some other higher frequency components, superimposed with the fundamental frequency, that are not present in the model and may be caused by boundary reflections.

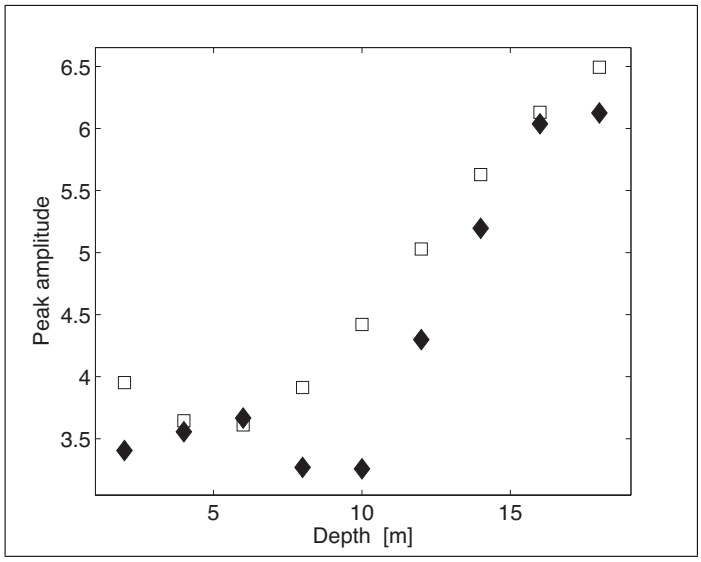

FIGURE 4.8. Transfer function peak amplitudes for all the nine receivers in the water column. $\mathrm{R_B} = 0.7$ and $\mathrm{R_T} = -0.1$. Note that $\mathrm{R_T}$ is phase-reversed. Model:(□), Data:(⧫).

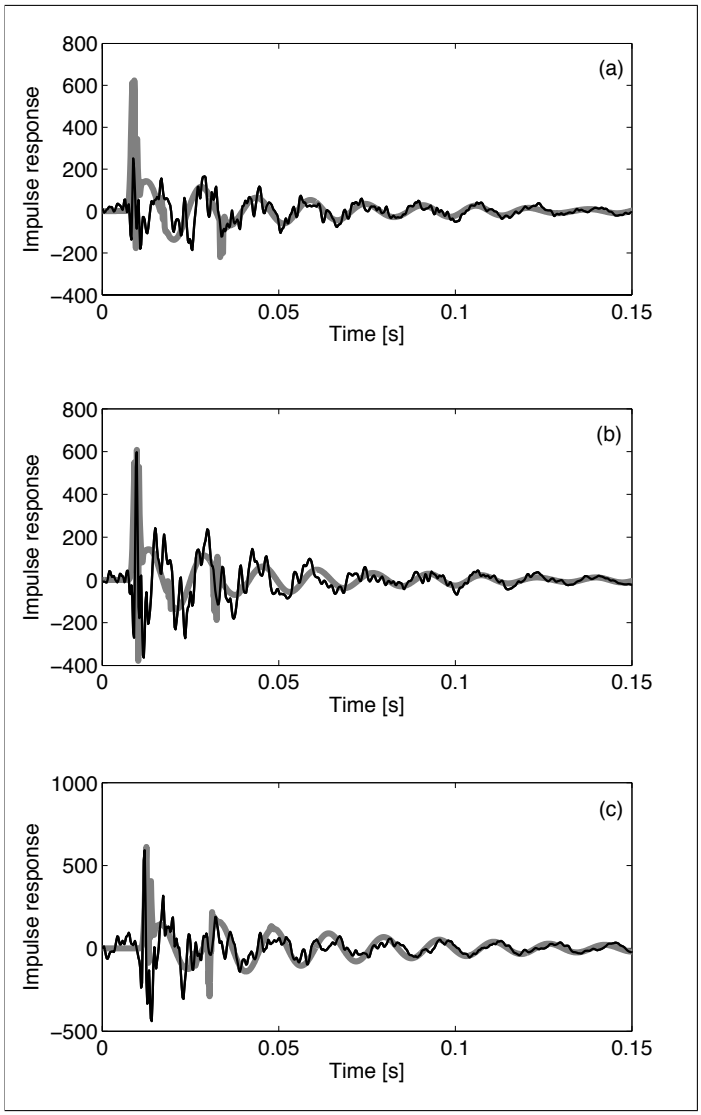

FIGURE 4.9. Pressure impulse response due to the bubbles, for the receivers located at (a)2 m, (b)6 m and (c)12 m depth. Black line: IFFT of transfer function data. Gray line: perturbation-based solution.

5. CONCLUSIONS

A model used previously to study collective back scattering from schools of swim bladder fish, which incorporates both multiple scattering effects between neighboring fish and coherent interactions of their individual scattered fields, has been used to analyze the forward scattering properties of these objects (the CDE approach). A detailed theoretical analysis has been performed which shows that there is an essential physical difference between back and forward scattering from fish schools. Strong frequency dependent interference effects, which affect the back scattered field amplitude, are practically absent in the forward scattering case. An investigation was made, using the modeled frequency dependence of the extinction coefficient, of the degree of downward shift of the peak frequency of the collective resonance of fish schools, as a function of the number of fish in the schools. Measurements of this frequency shift provide a means for estimating the number of fish in the schools. It was found that, for oblate spheroidal fish schools, the frequency shift is governed by the relation $f_0'/f_0 \propto N^{-1/3}$, just as previously found for the fundamental mode of a spherical bubble cloud. (***Chapter 2***)

A reanalysis has been made of transmission data obtained during the Modal Lion experiment in September 1995, and reported by Diachok (1999). The overall results of the analysis of this data using the present forward scattering approach, compared to those obtained using the previous method based upon back scatter modeling, show that the forward scattering analysis leads to significantly larger estimates of fish abundance than the previous analysis. The number of fish indicated increases by 60-200% (and possibly even more). The estimates of the number of fish in the schools depends strongly on the nearest-neighbor spacing s of the fish. Table 2.3 also shows several other combinations of the number of fish N in the school, and the nearest-neighbor spacing s, which can be used to fit the Diachok data. It is possible to use the forward scattering method to predict values of N which do conform to those previously predicted using back scatter modeling. However, to do this, the spacing s has to be reduced to values which are probably not indicated by other observational data. (***Chapter 2***)

The effective medium (EM) method was used to investigate resonance scattering from schools of swim bladder fish, and compared with the CDE approach. A theoretical comparison for idealized spherical schools (Figs. 3.2, 3.3 and 3.4) showed good agreement in forward scattering, where interference effects have a minimal effect. Good agreement was also seen in back scattering at low frequencies, when the wavelength is significantly larger than the fish separation, specifically, $\lambda \geq 4s$. If $\lambda < 4s$, the models diverge in back scattering, and the effective medium method fails. This can be critically important, if schools migrate to deeper water, thereby causing the collective resonance frequency to increase. At 2 m and 25 m depth (Figs. 3.2, 3.3), the resonance region lies below the wavelength limit. In both cases, the resonance behavior is adequately resolved. However, at 65 m, the agreement is not good (Fig. 3.4). Multiple scattering interactions are significant when $|4\pi n \mathrm{f}_b^2/k| > 0.01$. A comparison with low frequency forward scattering data shows very good agreement for both models, and indicates a method for estimating fish abundance. For back scattering data, the effective medium method is seen to diverge strongly when $\lambda < 4s$. (***Chapter 3***)

The resonance scattering properties of schools of swim bladder fish are very similar to those of clouds of bubbles in water. This work also presents a new method to calculate the impulse response of a near surface bubble cloud in a compressible medium and in the presence of a reflective bottom, based on perturbation theory (McComb,2004) applied to the coupled differential equation formalism. The solution ϕ for the differential volume of each bubble is formulated as an expansion in a control parameter ϵ, where the first term of the expansion (ϕ_0) corresponds to the solution of an exactly solvable problem. The remaining terms are iteratively calculated, and incorporate multiple scattering effects between bubbles. This method provides for an approximate solution for $0 < \epsilon < 1$, where $\epsilon = 0$ represents the soluble case, and $\epsilon = 1$ leads to the exact solution. In the latter case, there is no reason to truncate the expansion, and a convergence criterion is needed. In general, the convergence of the expansion will be determined by the physical bubbles parameters and the interaction between them. (***Chapter 4***)

The perturbation-based model was tested against experimental measurements of an artificial bubble cloud located near the surface, in a shallow fresh water lake environment. The artificial bubble cloud consisted of 14 fixed latex balloons of 4.68 cm radius at the surface. Transfer functions (hydrophone voltage normalized by driven voltage) were measured from 30 Hz to 2 kHz by nine hydrophones, located at 2 meter intervals of depth from 2 meters to 18 meters, at a horizontal distance of 11.7 meters from the center of the bubble cloud. A measurement technique was used to isolate the acoustic effect of the bubble cloud scattering, by subtracting the signal due to the direct field (in the absence of bubbles) from the signal arising from the bubble cloud. After the subtraction, nine different curves were found, corresponding to the nine receivers. The model shows good agreement with the experimental transfer function data, both in amplitude and frequency. First and second order boundary reflections were successfully incorporated to represent the variation in the peak amplitude registered by the different hydrophones. A numerical benchmark was also implemented, using a fourth order Runge-Kutta algorithm. The input consisted of the impulse signal coming from the source plus the multiple scattering from the bubbles. Two issues arise with the benchmark solution. The first one is the impulse implementation, which depends upon the impulsive function chosen. In the perturbation-based solution, the impulsive input is applied just to the soluble case (i.e., the first term of the expansion ϕ_0), which can be solved analytically. Therefore, in this case, there is no need to create an impulse function to solve the equation. The second issue is related to stability. For the tested case, the numerical benchmark was less stable than the perturbation-based solution. Future work may explore the model stability as a function of the time resolution, system parameters, and time delays. (***Chapter 4***)

References

Anderson, V. C. (1950). Sound scattering from a fluid sphere. *J. Acoust. Soc. Am*, *22*, 426-431.

Andreeva, I. B. (1964). Scattering of sound by air bladders of fish in deep sound-scattering ocean layers. *Sov. Phys. Acoust.*, *10*, 17-20.

Andrews, M., Gong, Z., & Ratilal, P. (2011). Effects of multiple scattering, attenuation and dispersion in waveguide sensing of fish. *J. Acoust. Soc. Am.*, *130*, 1253-1271.

Azzali, M., Buracchi, G., Conti, S., Gambetti, S., & Luna, M. (1985). Relationship between the forms of pelagic fish distribution and nycthermal periods. a tentative model of behavior. *Oebalia*, *11*, 471-488.

Baik, K. (2013). Comment on resonant acoustic scattering from a swimbladder-bearing fish. *J. Acoust. Soc. Am.*, *133*, 5-8.

Barange, M., Hampton, I., & Soule, M. (1996). Empirical determination of in situ target strengths of three loosely aggregated pelagic fish species. *ICES J. Mar. Sci.*, *53*, 225-232.

Breder, C. M. (1965). Vortices and fish schools. *Zoologica*, *50*, 97-114.

Capps, R. N. (1989). *Elastomeric materials for acoustical applications* (Technical Report No. AD-A216872). Naval Research Laboratory.

Carey, W. M., & Roy, R. A. (1993). Sound scattering from microbubble distributions near the sea surface. In *Ocean reverberation* (pp. 25–43). Springer.

Carstensen, E., & Foldy, L. (1947). Propagation of sound through a liquid containing bubbles. *J.Acoust. Soc. Am.*, *19*(3), 481–501.

Carter, G. C., Knapp, C. H., & Nuttall, A. H. (1973). Estimation of the magnitude-squared coherence function via overlapped fast fourier transform processing. *IEEE Trans. Audio Electroacoust.*, *21*(4), 337–344.

Chen, C.-T. (1999). Linear system theory and desing. In (Third ed., chap. 3,4). Oxford University Press.

Ching, P., & Weston, D. (1971). Wide band studies of shallow water acoustic attenuation due to fish. *J. Sound Vib.*, *18*, 499-510.

Church, C. (1995). The effects of an elastic solid surface layer on the radial pulsations of gas bubbles. *J. Acoust. Soc. Am*, *97*, 1510-1521.

Clay, C. S., & Medwin, H. (1977). *Acoustical oceanography: principles and applications* (Vol. 15). John Wiley & Sons.

Commander, K., & Prosperetti, A. (1989). Linear pressure waves in bubbly liquids: Comparison between theory and experiments. *J. Acoust. Soc. Am*, *85*, 732-746.

Cullen, J., Shaw, E., & Baldwin, H. (1965). Methods for measuring the three-dimensional structure of fish schools. *Anim. Behav.*, *13*, 534-543.

Culley, M. (1971). The pilchard :biology and exploitation. Pergamon Press, New York.

d'Agostino, L., & Brennan, C. (1988). Acoustical absorption and scattering cross sections of spherical bubble clouds. *J. Acoust. Soc. Am*, *84*, 2126-2134.

Devin, C. (1959). Survey of thermal, radiation, and viscous damping of pulsating air bubbles in water. *J. Acoust. Soc. Am.*, *31*, 1654-1667.

Diachok, O. (1999). Effects of absorptivity due to fish on transmission loss in shallow water. *J. Acoust. Soc. Am*, *105*, 2107-2128.

Diachok, O. (2000). Absorption spectroscopy: A new approach to estimation of biomass. *Fish. Res.*, *47*, 231-244.

Doinikov, A. (2001). Acoustic radiation interparticle forces in a compressible fluid. *J. Fluid Mech.*, *444*, 1-21.

Doinikov, A., Manasseh, R., & Ooi, A. (2005). Time delays in coupled multibubble systems. *J. Acoust. Soc. Am*, *117*, 47-50.

Doinikov, A., & Zavtrak, S. (1995). On the mutual interaction of two gas bubbles in a sound field. *Phys. Fluids.*, *7*(8), 1923-1930.

Doinikov, A., & Zavtrak, S. (1997). Radiation forces between two bubbles in a compressible liquid. *J. Acoust. Soc. Am*, *102*(3), 1424-1431.

Dolder, C. (2014). *Direct measurement of effective medium properties of model fish schools*. Unpublished doctoral dissertation, The University of Texas at Austin.

Enenstein, G. (2014). *Two studies on the acoustics of multiphase materials: Seagrass tissue and encapsulated bubbles*. Unpublished master's thesis, The University of Texas at Austin.

Farquhar, G. B. (1976). Biological sound scattering in the oceans: a review. *J.Acoust. Soc. Am.*, *59*(S1), S73–S73.

Feuillade, C. (1995). Scattering from collective modes of air bubbles in water and the physical mechanism of superresonances. *J. Acoust. Soc. Am.*, *98*, 1178-1190.

Feuillade, C. (1996). The attenuation and dispersion of sound in water containing multiply interacting air bubbles. *J.Acoust. Soc. Am.*, *99*(6), 3412–3430.

Feuillade, C. (2001). Acoustically coupled gas bubbles in fluids: Time domain phenomena. *J. Acoust. Soc. Am*, *109*, 2606-2615.

Feuillade, C. (2012). Superspheroidal modeling of resonance scattering from elongated air bubbles and fish swim bladders. *J. Acoust. Soc. Am*, *131*, 146-155.

Feuillade, C., & Clay, C. (1999). Anderson (1950) revisited. *J. Acoust. Soc. Am.*, *106*, 553-564.

Feuillade, C., & Nero, R. (1998). A viscous-elastic swim bladder model for describing enhanced-frequency resonance scattering from fish. *J. Acoust. Soc. Am*, *103*, 3245-3255.

Feuillade, C., Nero, R., & Love, R. (1996). A low-frequency acoustic scattering model for small schools of fish. *J. Acoust. Soc. Am*, *99*, 196-208.

Foldy, L. L. (1945). The multiple scattering of waves. i. general theory of isotropic scattering by randomly distributed scatterers. *Phys. Rev.*, *67*(3-4), 107.

French, A. P. (1971). Vibration and waves. In (p. 80-90). CRC press.

Freon, P., Gerlotto, F., & Soria, M. (1996). Diel variability of school structure with special reference to transition periods. *ICES J. Mar. Sci.*, *53*, 459-464.

Frisch, U. (1970). *Wave propagation in random media.* (Tech. Rep.). Centre National de la Recherche Scientifique, Paris.

Gong, Z., Andrews, M., Jagannathan, S., Patel, R., Jech, J., Makris, N., et al. (2010). Low-frequency target strength and abundance of shoaling atlantic herring (clupea harengus) in the gulf of maine during the ocean acoustic waveguide remote sensing 2006 experiment. *J. Acoust. Soc. Am.*, *127*, 104-123.

Gordoa, A., & Duarte, C. (1991). Size-dependent spatial distribution of hake in namibian waters. *Can. J. Fish. Aquat. Sci.*, *48*, 2095-2099.

Graves, M. (1968). Air-bubble curtain in sub-aqueous blasting at muddy run. *Civil Engineering*, *38*(6), 59.

Guillon, L., Holland, C. W., & Barber, C. (2011). Cross-spectral analysis of midfrequency acoustic waves reflected by the seafloor. *IEEE J. Oceanic Eng.*, *36*, 248-258.

Hahn, T. R. (2007). Low frequency sound scattering from spherical assemblages of bubbles using effective medium theory. *J.Acoust. Soc. Am.*, *122*(6), 3252–3267.

Hassani, S. (2013). *Mathematical physics: a modern introduction to its foundations*. Springer Science & Business Media.

Henyey, F. S. (1999). Corrections to foldys effective medium theory for propagation in bubble clouds and other collections of very small scatterers. *J.Acoust. Soc. Am.*, *105*(4), 2149–2154.

Holliday, D. V. (1972). Resonance structure in echoes from schooled pelagic fish. *J. Acoust. Soc. Am.*, *51*, 1322-1332.

Hsiao, P.-Y., Devaud, M., & Bacri, J.-C. (2001). Acoustic coupling between two air bubbles in water. *Eur. Phys. J. E*, *4*(1), 5-10.

Hu, H., Dowell, E., & Virgin, L. (1998). Stability estimation of high dimensional vibrating systems under state delay feedback control. *J. Sound Vib.*, *214*(3), 497-511.

Ishimaru, A. (1997). Wave propagation and scattering in random media. In (p. 14-15). JIEEE Press, New York.

Jones, J. P. (2012). *Acoustical imaging* (Vol. 21). Springer Science & Business Media.

Kargl, S. G. (2002). Effective medium approach to linear acoustics in bubbly liquids. *J.Acoust. Soc. Am.*, *111*(1), 168–173.

Kim, Y., & Nelson, P. (2003). Spatial resolution limits for the reconstruction of acoustic source strength by inverse methods. *J. Sound Vib.*, *265*(3), 583–608.

Lamb, H. (1945). Hydrodynamics. In (6nd ed., chap. 56). Dover, New York.

Lee, K. M., McNeese, A. R., Tseng, L. M., Wochner, M. S., & Wilson, P. S. (2012). Measurements of resonance frequencies and damping of large encapsulated bubbles in a closed, water-filled tank. In *Proceedings of meetings on acoustics* (Vol. 18).

Leighton, T. (1994). The acoustic bubble. In (p. 137-148). Academic, San Diego.

Leighton, T., White, P., Morfey, C., Clarke, J., Heald, G., Dumbrell, H., et al. (2002). The effect of reverberation on the damping of bubbles. *J.Acoust. Soc. Am.*, *112*(4), 1366–1376.

Love, R. (1977). *A new model of resonant acoustic scattering by swimbladder-bearing fish*. Unpublished doctoral dissertation, Norda Report 4, Naval Oceanographic Laboratory.

Love, R. (1978). Resonant acoustic scattering by swim bladder-bearing fish. *J. Acoust. Soc. Am.*, *64*, 571-580.

Love, R. (2013). Response to comment on resonant acoustic scattering by swimbladder-bearing fish[j. acoust. soc. am. 64, 571–580 (1978)]. *J.Acoust. Soc. Am.*, *134*(5), 3399–3402.

Lu, N., Prosperetti, A., & Yoon, S. (1990). Underwater noise emissions from bubble clouds. *Journal of Oceanic Engineering*, *15*, 275-281.

Marshall, N. B. (1951). Bathypelagic fishes as sound scatterers in the ocean. *J. Mar. Res.*, *10*, 1-17.

Maynard, J. D., Williams, E. G., & Lee, Y. (1985). Nearfield acoustic holography: I. theory of generalized holography and the development of NAH. *J.Acoust. Soc. Am.*, *78*(4), 1395–1413.

McCartney, B. S. (1967). Underwater sound in oceanography. In V. M. Albers (Ed.), (Vol. 2, p. 185-201). Plenum, New York.

McComb, W. (2004). Renormalization methods: A guide for beginners. In (p. 28-33). Oxford, University Press.

Medwin, H., & Clay, C. (1998). Fundamentals of acoustical oceanography. In (p. 237-238). Academic, Boston.

Mettin, R., Akhatov, I., Parlitz, U., Ohl, C., & Lauterborn, W. (1997). Bjerknes forces between small cavitation bubbles in a strong acoustic field. *Physical review E*, *56*, 2924-2931.

Mettin, R., Luther, S., Kamphausen, S., & Lauterborn, W. (2000). Dynamics of delay-coupled spherical bubbles. In *Aip conference proceedings.* IOP Institute of Physics Publishing LTD.

Minnaert, M. (1933). On musical air-bubbles and the sounds of running water. *Philosophical Magazine*, *16*, 235-248.

Misund, O. (1991). *Dynamics of moving masses: variability in packing density, shape, and size among herring, sprat, and saithe schools*. Unpublished doctoral dissertation, Bergen, Norway.

Misund, O., Aglen, A., & Frønæs, E. (1995). Mapping the shape, size, and density of fish schools by echo integration and a high-resolution sonar. *ICES J. Mar. Sci.*, *52*, 11-20.

Nero, R., Thompson, C., & Love, R. (1997). Abyssopelagic grenadiers: The probable cause of low frequency sound scattering at great depths off the oregon and california coasts. *Deep-Sea Res*, *44*, 627-645.

Ogata, K. (2004). System dynamics. In (Fourth ed., chap. 5.1 and 8.5).

Ooi, A., Nikolovska, A., & Manasseh, R. (2008). Analysis of time delay effects on a linear bubble chain systema. *J. Acoust. Soc. Am*, *124*, 815-826.

Papachristodoulou, A., Peet, M., & Lall, S. (2005). Constructing lyapunov-krasovskii functionals for linear time delay systems. In *American control conference, 2005. proceedings of the 2005* (pp. 2845–2850).

Pitcher, T., Magurran, A., & Edwards, J. (1985). Schooling mackerel and herring choose neighbours of similar size. *Marine Biology*, *86*, 319-322.

Pitcher, T., & Parrish, J. (1993). Functions of shoaling behavior in teleosts. In T. J. Pitcher (Ed.), (2nd ed., p. 363-439). Chapman and Hall, New York.

Prosperetti, A. (1977). Thermal effects and damping mechanisms in the forced radial oscillations of gas bubbles in liquids. *J. Acoust. Soc. Am*, *61*, 17-27.

Raveau, M., & Feuillade, C. (2015). Sound extinction by fish schools: Forward scattering theory and data analysis. *J.Acoust. Soc. Am.*, *137*(2), 539–555.

Scalabrin, C. (1997). *Identification acoustique des especes pelagiques a partir d'attributs discriminants des bancs de poissons monospecifiques*. Unpublished doctoral dissertation, Brest, France.

Scalabrin, C., Diner, N., Weill, A., Hillion, A., & Mouchot, M. (1996). Narrowband acoustic identification of monospecific fish shoals. *ICES J. Mar. Sci.*, *53*, 181-188.

Scrimger, J., Turner, R., & Heyd, G. (1972). Backscattering of underwater sound in saanich inlet, british columbia, including observations of scattering from a fish school. *J. Acoust. Soc. Am.*, *51*, 1098-1105.

Steele, J. H., Thorpe, S. A., & Turekian, K. K. (2009). *Elements of physical oceanography: a derivative of the encyclopedia of ocean sciences*. Academic Press.

Stotts, S., Knobles, D., Keller, J., Piper, J., & Thompson, L. (2006). Geoacoustic inversion of short range source data using a plane wave reflection coefficient approach. *J.Acoust. Soc. Am.*, *120*(6), 3607–3626.

Twersky, V. (1962). Multiple scattering of waves and optical phenomena. *JOSA*, *52*(2), 145–169.

Waterman, P. (1969). New formulation of acoustic scattering. *J.Acoust. Soc. Am.*, *45*(6), 1417–1429.

Weber, T., Lutcavage, M., & Schroth-Miller, M. (2013). Near resonance acoustic scattering from organized schools of juvenile atlantic bluefin tuna (thunnus thynnus). *J. Acoust. Soc. Am.*, *133*, 3802-3812.

Welch, P. D. (1967). The use of fast fourier transform for the estimation of power spectra: A method based on time averaging over short, modified periodograms. *IEEE Trans. Audio Electroacoust.*, *15*(2), 70–73.

Weston, D. (1966). Acoustic interaction effects in arrays of small spheres. *J.Acoust. Soc. Am.*, *39*(2), 316–322.

Weston, D. (1977). Underwater acoustics. In V. M. Albers (Ed.), (Vol. 2, chap. 5). Plenum, New York. (Please note that Eq. (13) on page 59 contains a typographical error. It is correctly stated in the present work.)

Weston, D., & Ching, P. (1970). Sound extinction by fish in one-way shallow water propagation. In G. B. Farquhar (Ed.), *Proceedings of an international symposium on biological sound scattering in the ocean* (p. 212-219). Maury Center for Ocean Science, Washington, D.C.

Woodhead, P. (1966). The behaviour of fish in relation to light in the sea. *Oceanogr. Mar. Biol. Ann. Rev.*, *4*, 337–403.

Ye, Z., & Ding, L. (1995). Acoustic dispersion and attenuation relations in bubbly mixture. *J.Acoust. Soc. Am.*, *98*(3), 1629–1636.